EXTERNAL AND INTERNAL MAGNETOHYDROSTATIC MODELS OF QUIESCENT SOLAR PROMINENCES

Nicholas P. Cartledge

A Thesis Submitted for the Degree of PhD
at the
University of St Andrews

1996

External and Internal Magnetohydrostatic Models of Quiescent Solar Prominences

Nicholas P. Cartledge

Thesis submitted for the degree of Doctor of Philosophy
of the University of St. Andrews.

Declaration

1. I, Nicholas Philip Cartledge, hereby certify that this thesis has been composed by myself, that it is a record of my own work, and that it has not been accepted in partial or complete fulfilment of any other degree or professional qualification.

   Signed .... Date ...21/12/95..

2. I was admitted to the Faculty of Science of the University of St. Andrews under Ordinance General No. 12 in October 1991 and as a candidate for the degree of Ph.D. in October 1992.

   Signed .... Date ....21/12/95..

3. I hereby certify that the candidate has fulfilled the conditions of the Resolution and Regulations appropriate to the Degree of Ph.D.

   Signature of Supervisor ....Date ..21.12.95

4. In submitting this thesis to the University of St. Andrews I understand that I am giving permission for it to be made available for use in accordance with the regulations of the University Library for the time being in force, subject to any copyright vested in the work not being affected thereby. I also understand that the title and abstract will be published, and that a copy of the work may be made and supplied to any bona fide library or research worker.

Acknowledegments

I would like to thank the members of the Solar Theory Group in St Andrews for their support and help over the last three years. I am also grateful to the Particle Physics and Astronomy Research Council for providing financial support.

My acknowledgements also go to my other friends and colleagues for many enlightening conversations during "extended" coffee breaks and for contributing to some memorable sporting occasions including 5-a-side footie, all-weather golf matches and various public house pastimes! I would also like to thank my flat-mates for a truly unforgettable three years and for providing a hearty plate of supper on many a freezing Winter's night!

Without the help and guidance of my supervisors, Eric Priest and Alan Hood, this thesis would not have been possible, and special thanks go to Slava Titov, for many hours of stimulating conversation.

Finally, I would like to thank my family and my girlfriend, Heather, for providing invaluable support and encouragement, and it is to them I dedicate this thesis.

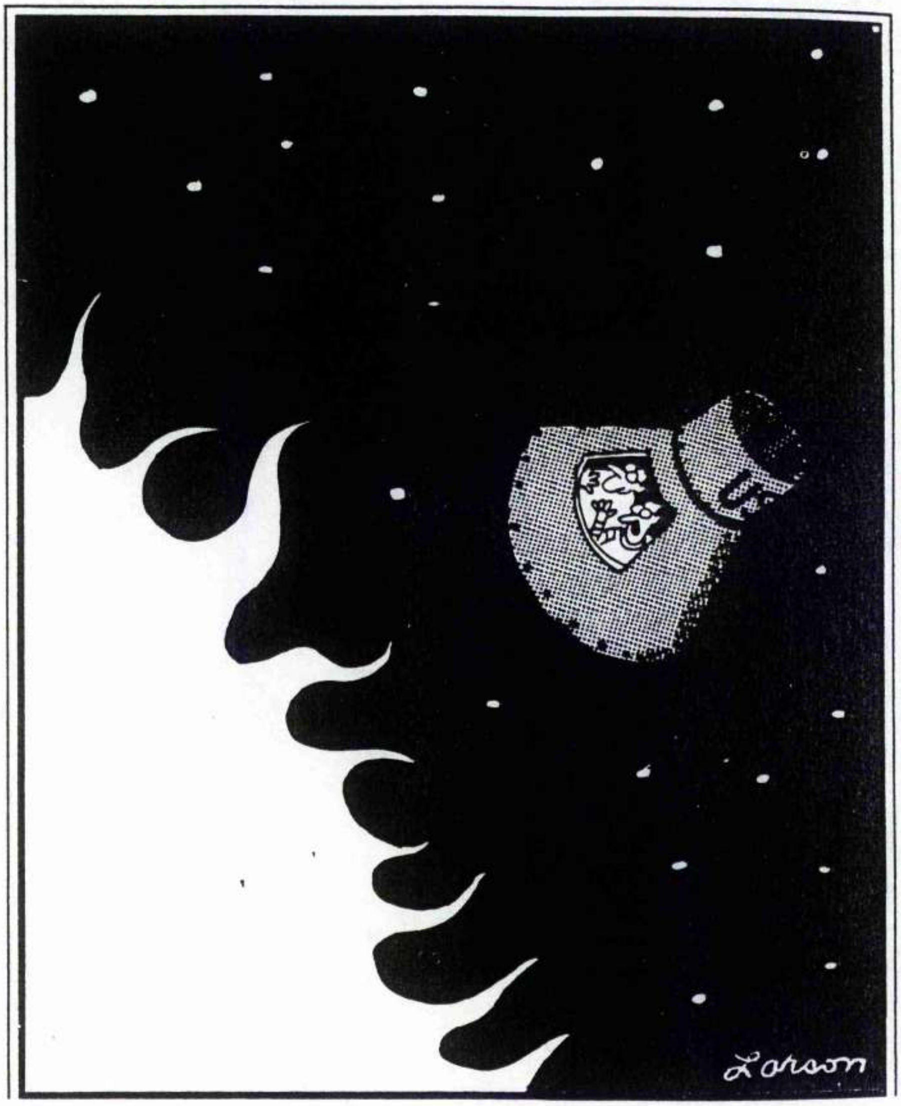

"Blast! The controls are jammed! . . . We're headed straight for Mr. Sun!"

Abstract

Quiescent solar prominences are amongst the most interesting and yet least understood of the phenomena observed on the Sun and provide both the theorist and the observer with equally demanding challenges.

The theoretical study of prominences is an important branch of solar physics as it contributes significantly to the overall understanding of the Sun and its atmosphere. One only needs to be presented with the illuminating fact that there is more mass contained in these bodies than in the remainder of the entire corona to be convinced of their importance. Although many of the physical mechanisms associated with prominence theory are important in their own right, they are also of much wider relevance for various other astrophysical phenomena. For example, radiative and magnetic instabilities are explored in detail in the context of solar prominences; yet clearly these are important processes that relate to many other branches of astrophysics. Prominences are intimately associated with solar flares which occur when a prominence loses equilibrium. Also, prominence eruptions are very important as they are closely connected with coronal mass ejections. These account for a large fraction of the total mass lost from the Sun and so are extremely important events, particularly when one considers the consequences as this plasma interacts with the Earth's environment.

It is the period of global equilibrium of quiescent prominences, though, that is the focus of this thesis. Various models are proposed to help understand both the topology and supporting mechanisms of the external, coronal magnetic field, and also the internal prominence structure and the way in which the two regimes fit together.

In Chapter 3 we extend a model for the equilibrium of a prominence sheet in a twisted magnetic flux-tube, given by Ridgway, Priest and Amari (1991), to incorporate a current sheet of finite height. This removes the discontinuity at the edge of the tube and provides a shear-free outer boundary which enables the tube to be matched onto a background potential field. In addition, internal prominence solutions are found by expanding the sheet to a finite width and matching suitable magnetic profiles across this region.

Next we consider a global model for the magnetic field structure surrounding a polar-crown prominence. We examine potential configurations generated from typical distributions of photospheric flux, and select solutions for which there is a location of dipped

magnetic field where prominence material may collect and form. Once such a configuration is available, it is necessary to construct the ensuing prominence solution. We achieve this in Chapter 4 by considering a simplified form for the photospheric field. We show that the equilibrium contains a weighted, curved prominence sheet supported in the location of dipped magnetic field. The equilibrium requires an enhanced magnetic pressure below the sheet to support the component of weight in the normal direction.

The internal equilibrium of curved or inclined prominence material has not been considered previously and so we formulate, in Chapter 6, a simple one-dimensional isothermal solution for a cut across the prominence. This is developed to allow for variations along the sheet and in this way an internal solution for the curved prominence of Chapter 4 is given, which matches onto the external potential polar-crown field.

Finally, in Chapter 7, we rewrite this solution in terms of its constituent internal and external components and show how the composite solution switches between the two in a region of overlap, or transition region. From this, the internal plasma properties are deduced and realistic profiles for the pressure, density and temperature are obtained.

Contents

Chapter 1

Introduction to Prominences

1.1 Chapter Summary

In this chapter we describe the main properties of solar prominences, which have been a topic of great interest for hundreds of years now. We begin with a short historical review summarising the main observational developments and results obtained since the thirteenth century. A description of the different types of prominence is given but we concentrate on the properties of quiescent prominences; the well-developed, slowly evolving category that have raised some pertinent questions for solar theory.

1.2 Historical Background

Historically, solar prominences have generated tremendous interest and have been observed now for a period of time dating back to the thirteenth century. In fact, the first recorded evidence of prominences is by Muratori in 1239 when he observed the corona during an eclipse and reported "a burning hole" in it. During a total solar eclipse, a large prominence located at the limb of the Sun is seen brightly in emission in the lower corona and so, in all probability, Muratori's observation was of a prominence. Figure 1.1 is a photograph showing the innermost corona during such an eclipse in which several prominences can be seen on the East limb. They actually appear red because of their strong emission in the $H\alpha$ line at $\lambda6563$ Å.

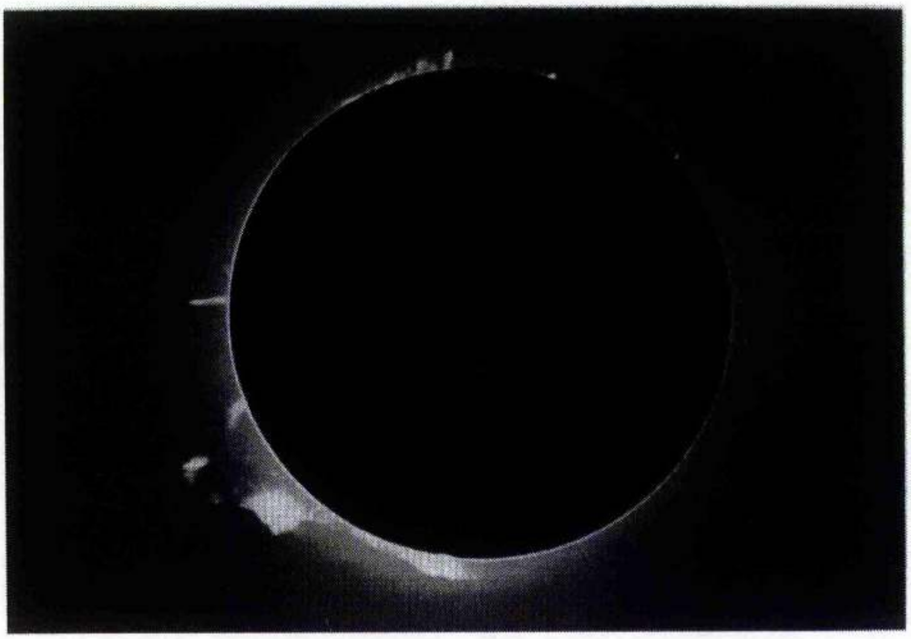

Figure 1.1: Prominences seen in emission at the limb (courtesy J. C. Noëns, Observatoire du Pic-du-Midi).

The first semi-scientific description of prominences came after an eclipse in 1733 during which Vassenius (1733) observed three or four prominences from Gothenburg, Sweden. He called them "red flames" and actually believed them to be clouds in the lunar atmosphere! Many other observers were in agreement with Vassenius' description, although Ulloa (1779) observed a low-lying prominence during the 1778 eclipse and attributed it to a hole in the moon. These early observations were subsequently forgotten and when the phenomenon was rediscovered during the eclipse of 1842, the observers were so bewildered by what they saw that their vague and ambiguous reports influenced later scientists to believe that prominences were actually mountains on the Sun!

1868 saw the advent of spectrographic methods which were employed during an eclipse in India and Malacca and it was determined that prominence spectra consist of bright lines; from then on prominences were realised to be glowing masses of gas. One of the observed lines, at 5876 Å, was not known to be emitted by any terrestrial atom and it was ascribed to a specific solar element called Helium, after Helios, the Greek Sun God. Because many of the prominence emission lines are so bright, the spectrograph could be used even in broad daylight without the aid of an eclipse, and so prominence spectra were observed far more frequently using this technique. In 1869, Huggins (1869) realised that by opening the spectrograph slit he could obtain a series of monochromatic images of prominences, corresponding to the emission lines observed with a normal slit. By using this method, the complex forms of prominences could be better studied.

In the 1890's the spectroheliograph was invented and prominences could then be studied against the disc as absorption features which were later referred to as "filaments". This presented a significant advance in the observations as it enabled the study of prominences as they passed from the disc to the limb, thus providing a more complete view of their overall shapes and forms. Figure 1.2 shows such a sequence of images and demonstrates the changing face of a prominence as it passes over the limb of the Sun. Notice how the prominence is initially seen in absorption since the dense material overlies the disc of the Sun and later in emission against the rarefied background atmosphere.

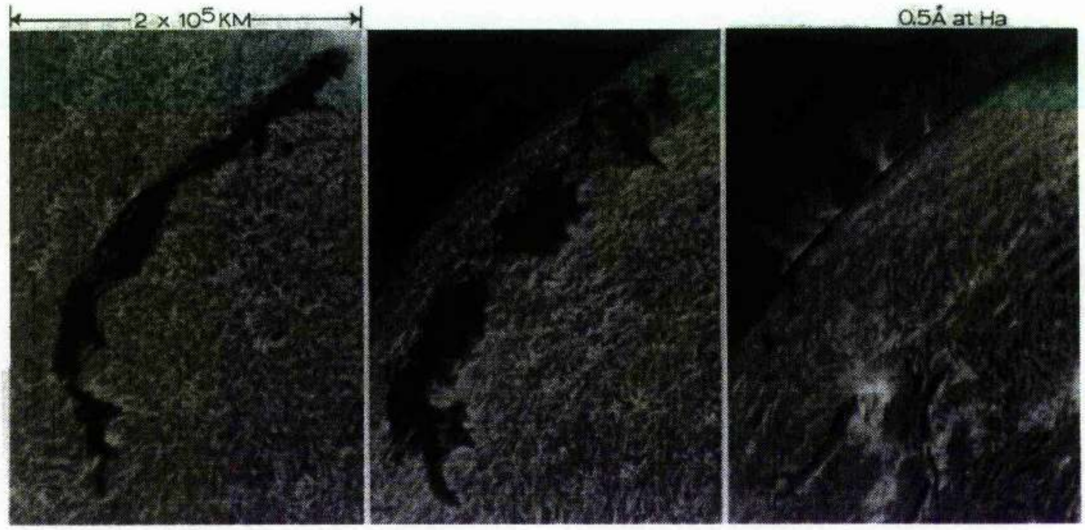

Figure 1.2: A time sequence of images in $H\alpha$ showing a prominence as it moves from the disc to the limb (courtesy S. Martin, Lockheed Solar Observatory).

This century has seen many further advances in prominence observations as improved instrumentation techniques have provided us with in-depth details of plasma properties such as temperature, density and velocity and also measurements of prominence magnetic fields. A description of the basic prominence properties is given in the following section.

We complete this historical introduction with a fascinating sketch from the book, "Le Soleil", by Secchi (1875) in which he depicts sunspots against the disc and several prominences seen in emission at the limb (Figure 1.3). In this book, Secchi actually refers to prominences as being "a universally well-known phenomenon", yet more than a century later the theory of solar prominences still poses some of the most difficult and puzzling questions related to solar activity!

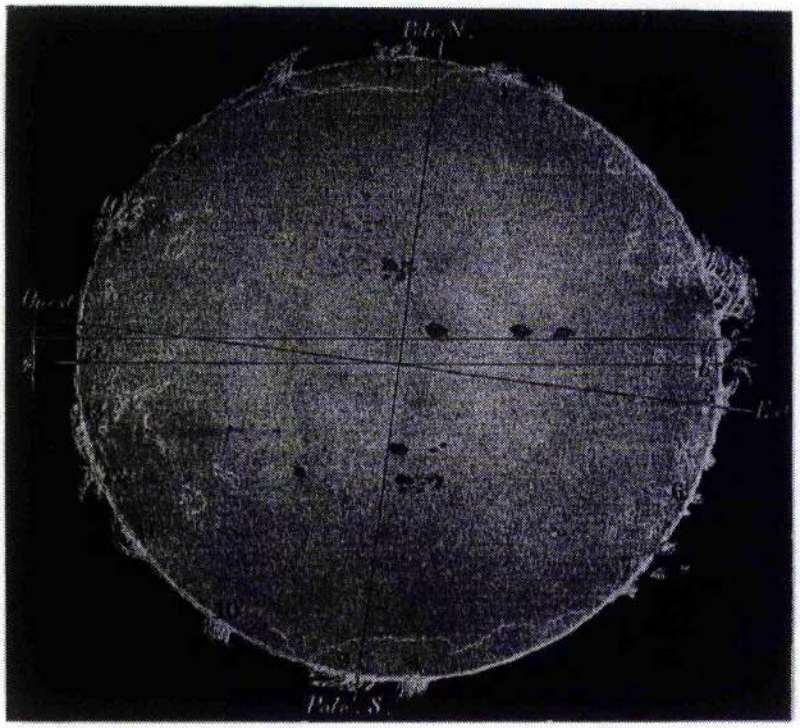

Figure 1.3: Secchi's sketch showing prominences at the limb of the Sun (Secchi, 1875).

1.3 Basic Description

Prominences are cool, dense bodies of plasma located in the lower regions of the solar corona. Typically, they possess temperatures which are 100 times lower than the surrounding atmosphere and their densities are 100 times higher. They are best observed in the $H\alpha$ line where they appear dark against the disc (due to absorption of the underlying photospheric emission) and bright at the limb (as they are strong in emission in comparison to the tenuous corona). One of the most important of all prominence observations is due to Babcock and Babcock (1955) and relates to the magnetic field: all prominences are seen to overlie a magnetic polarity inversion line, where the line-of-sight magnetic field reverses its sign. This has proved to be a highly significant result as it paved the way for the first theoretical prominence models and provides a real clue as to how these dense bodies can be supported against the Sun's huge gravitational pull.

1.3.1 Morphology

Several different types of prominence are observed on the Sun ranging from those which are dynamic, highly energetic and short lived to those which are slowly evolving, incredibly stable and long lived. Various suggestions have therefore been proposed as to how they might be categorised but the scheme given by Zirin (1988) seems to be as good as any. Table 1.1 shows his classification from which we see that prominences may basically be divided into two groups. The first group, active prominences, are the highly-dynamic features which display rapid plasma motions and are closely associated with flares, eruptions and the release of large amounts of energy over short time-scales.

Active (transient) Prominences	*Quiescent (long-lived) Prominences*
(a) Limb Flares (b) Loops and Coronal Rain (c) Surges (d) Sprays	(a) Active-Region Prominences (b) Quiet-Region Prominences (c) Ascending Prominences

Table 1.1: Basic Classification of Solar Prominences.

When a flare occurs, material may be driven upwards into the corona and this generally results in one of the many types of active prominence: surges occur when the ejected material is well collimated, probably by a strong magnetic field; sprays are active-region prominences which are erupting; and post-flare loops occur as the hot material cools and "rains" down to the surface, outlining the magnetic loop structures.

Although very dramatic, this category of prominence has received little theoretical attention, mainly due to the complexity of the governing time-dependent equations. The second class of prominence has been studied in far more detail since they are approximately static features (except type (c) which relates to their eventual eruption) and so can be modelled as magnetohydrostatic structures. It is to this class of prominence we pay our attention and now describe.

1.4 Quiescent Prominences

1.4.1 Plasma Properties

Quiescent prominences are seen against the disc as thin, dark ribbons of dense, optically thick material. Suspended in the lower corona, the dimensions of a quiet-region prominence are observed to be:

length:	60-600 Mm	(average 200 Mm) ,
height:	10-100 Mm	(average 50 Mm) ,
width:	4-15 Mm	(average 6 Mm) ,

and so they are essentially seen as thin sheets of current and plasma. From now on we will refer to "quiescent prominences" simply as "prominences" for brevity. Figure 1.4 (top) shows a full disc $H\alpha$ image in which several prominences are seen. Notice the prominence at the North-West limb which has been enlarged in Figure 1.4 (bottom). Prominence temperatures are commonly in the range $5,000 - 8,000\ K$ and their densities range between $10^{16}\ m^{-3}$ and $10^{17}\ m^{-3}$. Active-region prominences are typically a factor of three or four smaller than their mature quiet-region counterparts; their temperatures are much the same but their densities are rather higher. They lie at lower altitudes and they extend to heights of 20 Mm at most.

1.4.2 Magnetic Field

Prominences are always observed to overlie a magnetic polarity inversion line (Babcock and Babcock, 1955) and so the magnetic field is an essential ingredient and of fundamental importance to their formation, existence, evolution and eruption (see below). In fact, in his book on solar prominences, Tandberg-Hanssen (1974) wrote: "The single, physically most important parameter to study in prominences may be the magnetic field. Shapes, motions, and in fact the very existence of prominences, depend on the nature of the magnetic field threading the prominence plasma ...". Figure 1.5 depicts an active-region prominence against the disc showing its $H\alpha$ structure and its close relation to the photospheric magnetic field. In the magnetogram, black areas represent positive polarity and white areas are negative polarity. Thus, prominences are thought to be contained in large-scale magnetic flux tubes (Figures 1.4, 1.10) and this field plays an essential role in supporting the dense material over long time-scales; incredibly, quiet-region prominences can exist in the tenuous coronal environment for periods of up to several months! During this time the prominence

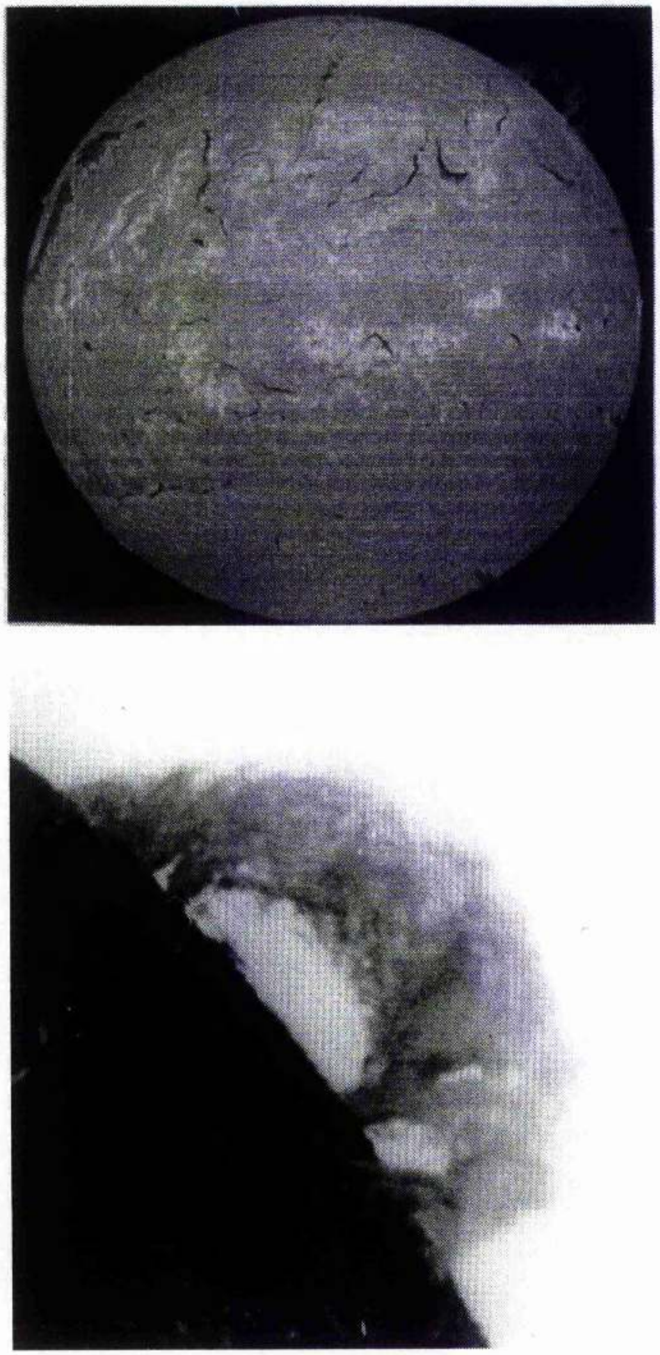

Figure 1.4: (Top) Full disc image of the Sun in $H\alpha$ showing several prominences in absorption against the disc. (Bottom) An enlargement of the prominence at the N-W limb which is seen in emission (courtesy Meudon Observatory).

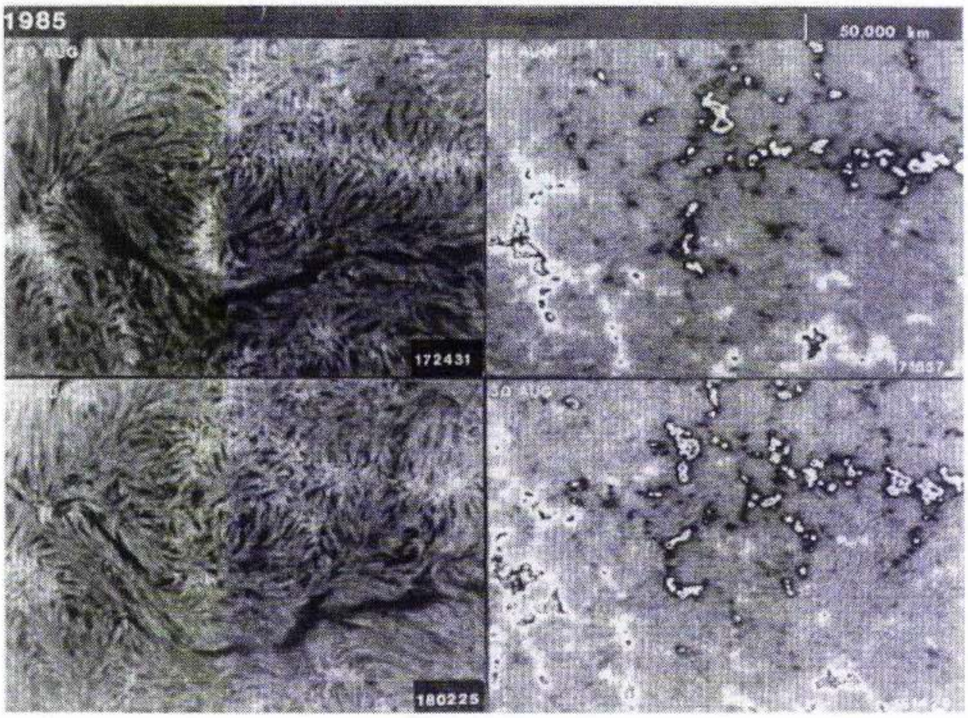

Figure 1.5: The relation between a prominence, filament channel and the photospheric magnetic field (courtesy S. Martin, Big Bear Solar Observatory).

Figure 1.6: Eclipse photograph showing limb prominences with overlying coronal cavities and helmet streamers (courtesy High Altitude Observatory).

evolves very slowly and remains in quasi-static equilibrium as long as the magnetic field structure is not disrupted.

The magnetic field also appears to play other roles. Overlying many prominences is a large-scale helmet streamer which can be seen during a total solar eclipse (Figure 1.6) and surrounding the prominence is a closed region of reduced density, often with a near-circular geometry. This is a coronal cavity (see Engvold (1989) for details) and may be considered to be the outline of a surrounding helical magnetic field. Prominences sometimes have a well defined upper edge (Figure 1.7) or lower boundary (Figure 1.8 (bottom)) both of which highlight the presence of the magnetic field.

Figure 1.7: $H\alpha$ image showing a quiet-region prominence with a well defined upper edge (courtesy Big Bear Solar Observatory).

The direction of the magnetic field in a prominence is quite interesting. The field is *highly sheared*, typically at an angle of 20° to the long axis of the prominence (Tandberg-Hanssen and Anzer, 1970; Leroy et al., 1983; Kim, 1990) and so may not necessarily be potential (or current free). Athay et al. (1983) finds that the field is inclined at an angle of 3° to the horizontal. In active-region prominences, the magnetic field is quite strong, usually ranging between 20 and 70 Gauss, yet in high-latitude (quiet-region) prominences it is somewhat weaker, typically 6 Gauss (Kim, 1990). Rust (1967) and Leroy et al. (1983)

found that the magnetic field strength in prominences often increases with height.

Because active-region prominences are relatively low-lying, the prominence field has a strong influence on the chromosphere and a well defined "filament channel" is seen underneath the prominence. Structurally, this is composed of fibrils aligned with the prominence and polarity inversion line and is a result of chromospheric material lying along the sheared, horizontal field. A good example of a filament channel is shown in Figure 1.5. In quiet-region prominences the filament channel is not nearly as well defined, because the chromospheric magnetic field is weaker and more vertically oriented, and so the underlying material tends to exhibit a *mottled* structure. At the limb, the effect of this field on the chromospheric structure can be seen (Figures 1.7, 1.8, 1.9).

1.4.3 Other Features

Prominences are not simply uniform, vertical sheets of plasma but possess many other significant attributes. Well-developed prominences reach down to the surface in a series of regularly spaced feet, resembling great tree trunks (Figures 1.4, 1.8), which are joined by huge arches, 30 Mm across. These feet were thought to be located at the boundaries of supergranule cells (Ploceniak and Rompolt, 1973) but this is a subject of controversy; some observers now believe that they are located over the cell centres where the convective flows are upwards. Material continuously drains out of the main body of the prominence at these points with velocities of around 1 $km\ s^{-1}$. The resulting loss of mass is immense and would drain the prominence in a day or so if it were not being replenished somehow. Upward flows are observed in prominences with velocities of about 0.5 $km\ s^{-1}$ (Schmieder, 1989) and fast, horizontal motions ($\sim 5\ km\ s^{-1}$) are sometimes observed in active-region prominences (Malherbe et al., 1983). Within a prominence there is much fine structure in the form of thin, vertical threads (Figures 1.8, 1.9) of length $\sim$ 5000 km and diameter 300 km or less (Démoulin et al., 1987) and so the material in a prominence is not homogeneously distributed but rather clumped within these small-scale structures.

1.4.4 Development

Prominences form either in active regions or between two adjacent active (or remnant active) regions (Martin, 1990; Tang, 1987) but the birth always takes place at the location of a polarity inversion line. Active-region prominences typically form over the course of a few

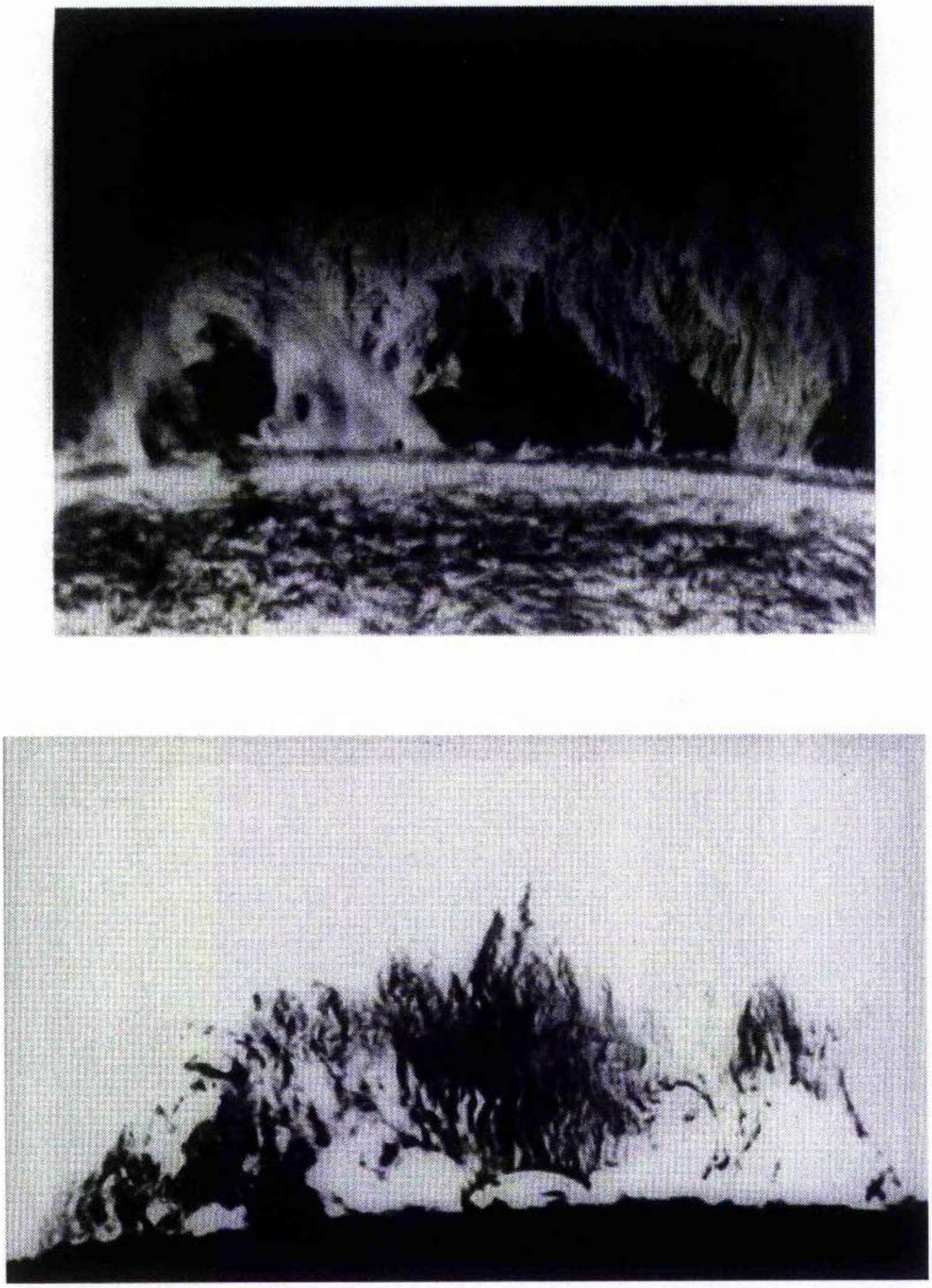

Figure 1.8: Prominences at the limb showing vertical fine structure and feet (courtesy H. Zirin, Big Bear Solar Observatory and Sacramento Peak Observatory).

Figure 1.9: Quiescent prominence showing fine structure (courtesy O. Engvold, Swedish Observatory, La Palma).

hours whilst quiet-region prominences take a bit longer, sometimes forming over a period of a few days. Observations show that a prominence will only form when a filament channel is already present in the chromosphere (Martin, 1990). This indicates that it is only after the correct magnetic geometry has been created (horizontal and highly sheared) that prominence material may collect and form.

Once formed, quiet-region prominences may exist for up to several solar rotations, evolving very slowly and gradually increasing in length and mass. The sustained equilibrium is due to the magnetic field which twists and threads through the dense material, somehow providing a form of magnetic hammock in which the plasma may rest. It is the force this field exerts upon the plasma, the *Lorentz force*, that needs to be directed upwards, thus providing a balance against gravity.

Eventually, though, an instability will occur and the prominence then erupts in an event known as a "disparition brusque". This is often a very dramatic event and, despite the presence of gravity, always occurs *upwards!* This seems counter-intuitive at first but it is the supporting magnetic field which has become unstable and the magnetic energy which is consequently released provides a driving force to accelerate the prominence material upwards with a velocity of several hundred kilometres per second. An eruption will generally occur when the height of the prominence exceeds $50Mm$. Examples of erupting prominences are shown in Figure 1.10 where the twist in the magnetic field can be clearly seen. Prominences do not always die by this mechanism; sometimes they disappear *thermally* (thermal disparition brusque), although it is not obvious from a theoretical viewpoint how the extra heating is supplied. As long as a filament channel is present the prominence will usually reform again a day or two after the eruption, often assuming a very similar form as before, although generally there will not be as much material present. Dynamical prominence eruptions are often associated with coronal mass ejections (or CME's). In this event, a huge body of overlying material is driven outwards and accelerated to tremendous velocities, often higher than 1000 $km\ s^{-1}$ (Hundhausen et al., 1984). The initiation of a CME takes place before the onset of the prominence eruption and the whole process occurs over a period of a few hours. Coronal mass ejections are hugely important phenomena as they represent a substantial proportion of the mass lost from the Sun.

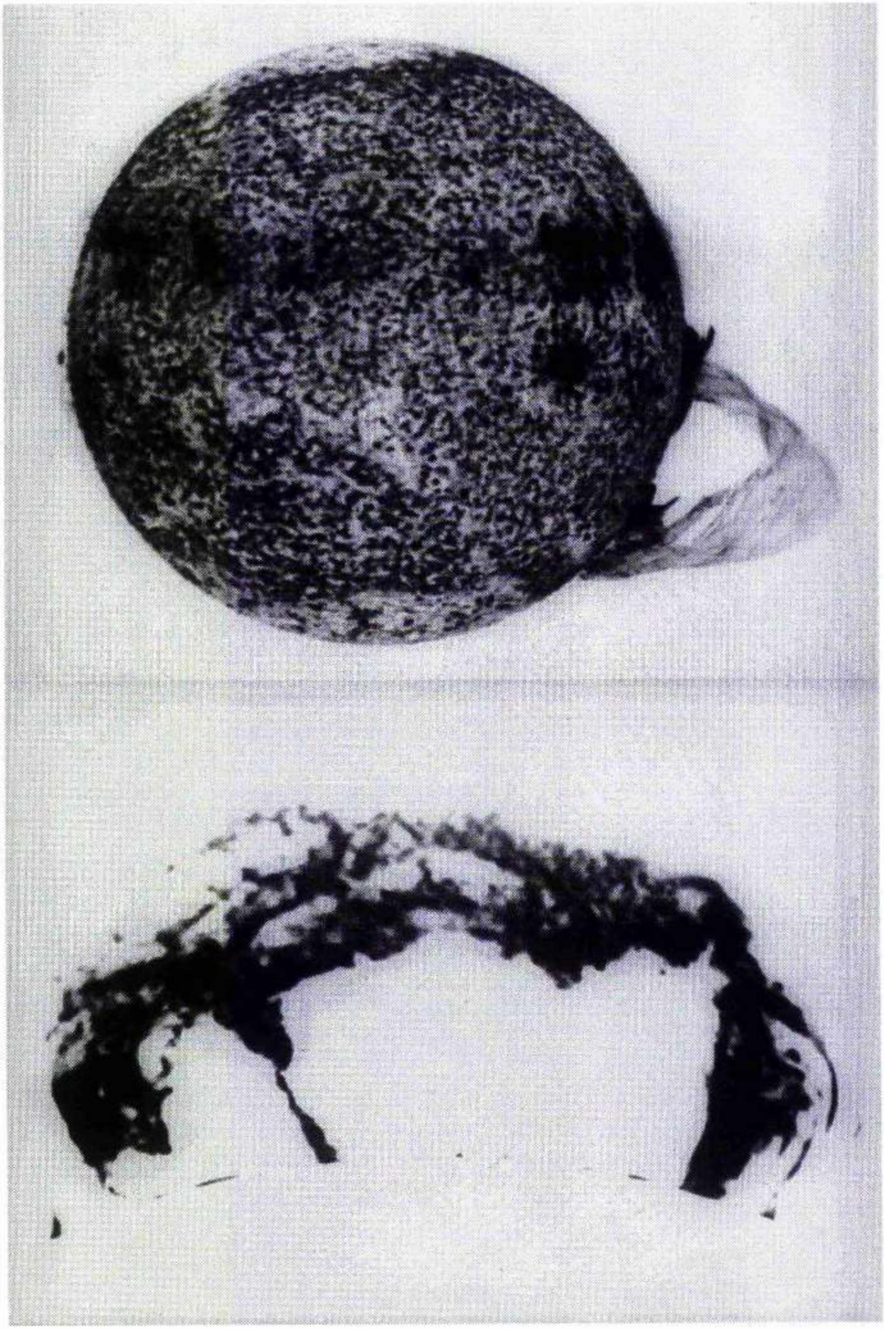

Figure 1.10: Examples of erupting prominences. The twist due to the magnetic field is clearly evident in these photographs (courtesy Naval Research Laboratory and Sacramento Peak Observatory).

Chapter 2

Governing Equations and Mathematical Modelling

2.1 Chapter Summary

This chapter provides a basis for the mathematical models presented throughout this thesis. Section 2.2 introduces the basic equations of magnetohydrodynamics (MHD) which can be broadly used to describe the interaction between a plasma (or electrically conducting fluid) and a magnetic field over large scales. In Section 2.3 the relevant equations for our magnetohydrostatic (MHS) studies are selected from the complete set of equations and some important implications are discussed. Any additional theory which is utilised within the subsequent chapters is considered here. Finally, in Section 2.4 a summary of important existing prominence models is given, thus completing the foundations upon which our work is based.

2.2 The Equations of Magnetohydrodynamics

The interaction of ionised solar plasma with the magnetic field that it has remarkably generated provides a fascinating topic for study. The term *plasma* refers to an electrically neutral material which is largely ionised; by considering length scales which are far greater than typical particle scales, the plasma may be treated as an electrically conducting fluid or a *continuum*. The equations governing the behaviour of such a fluid, the magnetohydrodynamic (MHD) equations, may be derived from two sets of equations: a simplified form of Maxwell's equations of electromagnetism which describe the relations between the electric and magnetic fields and the electric charge and current densities; and the hydrodynamic equations which interrelate pressure, density, temperature and flow velocity. For an in-depth description of these equations and their derivation see Priest (1982).

Maxwell's equations may be written

$$\nabla \times \mathbf{B} = \mu \mathbf{j} + \frac{1}{c^2}\frac{\partial \mathbf{E}}{\partial t} , \tag{2.1}$$

$$\nabla \cdot \mathbf{B} = 0 , \tag{2.2}$$

$$\nabla \times \mathbf{E} = -\frac{\partial \mathbf{B}}{\partial t} , \tag{2.3}$$

$$\nabla \cdot \mathbf{E} = \frac{\rho_c}{\epsilon} , \tag{2.4}$$

where $\mathbf{B}$ is the magnetic induction (usually referred to as the magnetic field), $\mathbf{E}$ is the electric field, $\mathbf{j}$ the current density and ρ_c the charge density. μ is the magnetic permeability and ϵ the permittivity which, for solar plasmas, may generally be ascribed their vacuum values, μ_0 $(= 4\pi \times 10^{-7}\ Hm^{-1})$ and ϵ_0 $(\approx 8.85 \times 10^{-12} Fm^{-1})$ such that the speed of light in a vacuum is given by $c = (\mu_0 \epsilon_0)^{-\frac{1}{2}}$.

The plasma must be essentially electrically neutral otherwise strong electrostatic forces would result and attract particles of the opposite charge, so neutralising the plasma. Therefore

$$\rho_c \ll n\ e ,$$

where n is the particle density and e is the electron charge.

The first of these equations (2.1), known as Ampère's law, states that magnetic fields are generated from the presence of electric currents or time varying electric fields. Equation (2.2) requires that there are no magnetic poles (net sources or sinks of magnetic field). Equation (2.3), Faraday's dynamo equation, and (2.4) imply that electric fields are generated either by magnetic fields which are varying in time or by the presence of electric charges.

We are now in a position to derive the MHD equations. By assuming (a) the velocity v_0 to be non-relativistic, i.e. $v_0 \ll c$, and (b) that the terms in equation (2.3) are of the same order of magnitude, we may eliminate the second term on the right-hand side of equation (2.1) using an order of magnitude argument. Therefore, this equation may be rewritten as

$$\nabla \times \mathbf{B} = \mu \mathbf{j} \ . \tag{2.5}$$

Plasma which is moving with a velocity $\mathbf{v}$ in a magnetic field $\mathbf{B}$ is subject to a total electric field

$$\mathbf{E} + \mathbf{v} \times \mathbf{B} \ .$$

Ohm's law states that the current density is proportional to this electric field and may be written

$$\mathbf{j} = \sigma(\mathbf{E} + \mathbf{v} \times \mathbf{B}) \ , \tag{2.6}$$

where σ is the electrical conductivity.

We now eliminate both $\mathbf{E}$ and $\mathbf{j}$ from (2.3), (2.5) and (2.6) and by using (2.2) we find that

$$\frac{\partial \mathbf{B}}{\partial t} = \nabla \times (\mathbf{v} \times \mathbf{B}) + \eta \nabla^2 \mathbf{B} \ , \tag{2.7}$$

where $\eta = (\mu\sigma)^{-1}$ is the magnetic diffusivity, taken to be uniform here. This is the induction equation and determines the magnetic field, subject to equation (2.2), when the plasma velocity is prescribed.

The first term on the right-hand side of (2.7) represents changes in the magnetic field due to the coupling of the field and plasma velocity, whereas the second term results from the effects of magnetic diffusion. By considering the ratio of the magnitudes of these terms we obtain, for a typical plasma velocity v_0 and length-scale l_0, a dimensionless parameter

$$R_m = \frac{l_0 v_0}{\eta} \ ,$$

known as the magnetic Reynolds number. If $R_m \gg 1$ the diffusion term may be neglected in (2.7) in an approximation known as the *perfectly conducting limit.* From this, Alfvén's frozen-flux theorem may be derived which states that in a perfectly conducting plasma (of which the solar corona is, in general, a good example), the magnetic field lines move with the plasma as if they were frozen to it. For many solar applications this theorem holds, although an important exception occurs in magnetic reconnection theory for which diffusion effects are certainly important. This occurs when the magnetic field varies strongly over small length scales, for example in the neighbourhood of an X-type neutral point or a current sheet.

The motion of the plasma is described by the equations of continuity and motion. Conservation of mass yields the continuity equation

$$\frac{D\rho}{Dt} + \rho \nabla \cdot \mathbf{v} = 0 \ , \tag{2.8}$$

where ρ is the plasma density and

$$\frac{D}{Dt} = \frac{\partial}{\partial t} + \mathbf{v} \cdot \nabla \ ,$$

is the convective time derivative.

The equation of motion can be written as

$$\rho \frac{D\mathbf{v}}{Dt} = -\nabla p + \mathbf{j} \times \mathbf{B} + \rho \mathbf{g} + \rho \nu \left(\nabla^2 \mathbf{v} + \frac{\nabla(\nabla \cdot \mathbf{v})}{3} \right) \ , \tag{2.9}$$

where p is the plasma pressure, $\mathbf{g}$ the acceleration due to gravity and ν the coefficient of kinematic viscosity, which is assumed to be uniform throughout the plasma. (2.9) states that a volume of plasma will experience an acceleration due to the various forces acting upon it, namely the plasma pressure gradient, the magnetic (or Lorentz) force, the gravitational force and any frictional force arising from viscosity. A comparison of the magnitudes of the terms in (2.9) gives the ratio of the inertial effects to viscous effects as

$$R_e = \frac{l_0 v_0}{\nu} ,$$

where R_e is the Reynolds number (cf. the magnetic Reynolds number, R_m). For many aspects of solar theory the Reynolds number is far greater than unity, allowing viscous effects to be neglected. When considering a plasma at rest, such as is the case for the global equilibrium of prominences, equation (2.9) reduces to the magnetohydrostatic equation. More will be said about this in Section 2.3.

The plasma pressure is assumed to be given by the ideal gas law, i.e.

$$p = \frac{\rho R T}{\tilde{\mu}} , \tag{2.10}$$

where T is the temperature and R is the gas constant. $\tilde{\mu}$ is the mean atomic weight, or the average mass per particle in terms of the proton mass, and so for a fully ionised hydrogen plasma, $\tilde{\mu} = 0.5$.

Finally we have an energy equation

$$\rho T \frac{Ds}{Dt} = -\mathcal{L} , \tag{2.11}$$

where s is the entropy per unit mass of the plasma and $\mathcal{L}$ is the energy loss function due to all the sources and sinks of energy. This may be written as the energy loss minus the energy gain, i.e.

$$\mathcal{L} = \nabla \cdot \mathbf{q} + L_r - \frac{j^2}{\sigma} - h ,$$

where $\mathbf{q}$ is the heat flux due to particle conduction, L_r is the net radiation, j^2/σ is the ohmic dissipation and h is the sum of all the remaining sources of heat. (2.11) may be rewritten in terms of the plasma pressure and density as

$$\frac{\rho^\gamma}{\gamma - 1} \frac{D}{Dt} \left(\frac{p}{\rho^\gamma} \right) = H + \frac{j^2}{\sigma} - L_r - \nabla \cdot \mathbf{q} , \tag{2.12}$$

where γ is the ratio of the specific heat of the gas at constant pressure to that at constant volume. If $\mathcal{L} = 0$ entropy is conserved and a thermal equilibrium is reached in which the energy gains balance the energy losses. This has important prominence applications (for example, see Hood and Priest (1979a); Priest and Smith (1979); Oran et al. (1982); Poland and Mariska (1986); Mok et al. (1990); Antiochos and Klimchuk (1991); Van Hoven et al. (1992); and references therein) as certain solutions permit cool, dense material to remain in equilibrium within the hot coronal surroundings. In this case the heat gained through conduction along the field lines is radiated away from the dense material in a steady-state solution.

Important velocities associated with the plasma are the sound speed

$$c_s = \sqrt{\frac{\gamma p}{\rho}} \ ,$$

and the Alfvén speed

$$v_A = \frac{B}{\sqrt{\mu\rho}} \ .$$

For a typical prominence plasma, these have the values of $c_s \approx 10\ km\ s^{-1}$ and $v_A \approx 90\ km\ s^{-1}$.

To summarise, the basic equations of MHD are

the induction equation:

$$\frac{\partial \mathbf{B}}{\partial t} = \nabla \times (\mathbf{v} \times \mathbf{B}) + \eta \nabla^2 \mathbf{B} \ ,$$

the continuity equation:

$$\frac{D\rho}{Dt} + \rho \nabla \cdot \mathbf{v} = 0 \ ,$$

the equation of motion:

$$\rho \frac{D\mathbf{v}}{Dt} = -\nabla p + \mathbf{j} \times \mathbf{B} + \rho \mathbf{g} + \rho\nu \left(\nabla^2 \mathbf{v} + \frac{\nabla(\nabla \cdot \mathbf{v})}{3} \right) \ ,$$

the ideal gas law:

$$p = \frac{\rho R T}{\tilde{\mu}} \ ,$$

and the energy equation:

$$\frac{\rho^\gamma}{\gamma - 1} \frac{D}{Dt} \left(\frac{p}{\rho^\gamma} \right) = h + \frac{j^2}{\sigma} - L_r - \nabla \cdot \mathbf{q} \ .$$

This set of equations determines $\mathbf{v}$, $\mathbf{B}$, ρ, p and T subject to the condition

$$\nabla \cdot \mathbf{B} = 0 \ .$$

In addition, $\mathbf{j}$ and $\mathbf{E}$ are given by **Ampère's law:**

$$\nabla \times \mathbf{B} = \mu \mathbf{j} \ ,$$

and Ohm's law:

$$\mathbf{j} = \sigma(\mathbf{E} + \mathbf{v} \times \mathbf{B}) \ .$$

2.3 The Equations of Magnetohydrostatics

The study of quiescent prominences involves structures which are either static or only very slowly evolving in time. When the flow speed v_0 is much less than the sound speed $(\gamma p_0/\rho_0)^{\frac{1}{2}}$, the Alfvén speed $B_0/(\mu\rho_0)^{\frac{1}{2}}$ and the gravitational free-fall speed $(2gl_0)^{\frac{1}{2}}$, for a vertical length-scale l_0, the equation of motion reduces to

$$\mathbf{0} = -\nabla p + \mathbf{j} \times \mathbf{B} + \rho \mathbf{g} \ . \tag{2.13}$$

This, coupled with the equations

$$\mathbf{j} = \frac{\nabla \times \mathbf{B}}{\mu} \ , \qquad \nabla \cdot \mathbf{B} = 0 \ , \qquad p = \frac{\rho R T}{\tilde{\mu}} \ ,$$

and an energy equation for the temperature, constitute the set of magnetohydrostatic (MHS) equations.

If gravity acts in the negative $\hat{y}$-direction then resolving forces along a field line gives

$$p = p_0 \exp\left(-\int_0^y \frac{1}{H(y')} dy'\right) \ , \tag{2.14}$$

where p_0 is the pressure at $y = 0$ and $H(y)$ is the pressure scale-height given by the ideal gas law as

$$H(y) = \frac{RT(y)}{\tilde{\mu} g} \ . \tag{2.15}$$

If we consider an isothermal atmosphere then H is constant and (2.14) becomes

$$p = p_0 \, e^{-y/H} \ . \tag{2.16}$$

(2.14) and (2.16) state that the pressure along a given magnetic field line decreases exponentially with height. These equations represent the background hydrostatic atmosphere in which gravity tends to stratify the atmospheric pressure along the magnetic field. In the corona, the scale-height is approximately $10^8 m$ $(= 100 Mm)$ and in a prominence it is two orders of magnitude lower.

The magnetic term (the Lorentz force) in (2.13) is particularly interesting. It is directed across the magnetic field so that any motion or density variation along field lines must be produced by gravity or pressure gradients. Using (2.5) it may be broken down into two terms, i.e.

$$\mathbf{j} \times \mathbf{B} = \frac{(\mathbf{B} \cdot \nabla)\mathbf{B}}{\mu} - \nabla \left(\frac{B^2}{2\mu} \right) \ . \tag{2.17}$$

On the right-hand side of this equation, the first term represents a magnetic tension force which acts in a direction perpendicular to curved field lines. This is a resultant restoring force which arises from the tension, of magnitude B^2/μ, along the field. Thus, field lines have a similar restoring property to elastic strings: in a catapult, the restoring force from the stretched elastic can be used to fire missiles large distances, whereas here the magnetic tension from kinked field lines may provide the force to support dense prominence sheets against gravity. The second term in (2.17) results from gradients in magnetic pressure $(B^2/2\mu)$ and acts from locations of strong field to locations of weak field. In vertical prominence sheet models, this force opposes the outwards plasma pressure gradient and acts to confine the plasma to a thin sheet. Along lines of force (field lines) the magnetic tension and pressure forces cancel so that the resultant force $\mathbf{j} \times \mathbf{B}$ acts perpendicularly to the field.

The ratio of plasma pressure to magnetic pressure is known as the plasma beta, written

$$\beta = \frac{2\mu p_0}{B_0^2} \ ,$$

for a given plasma pressure p_0 and magnetic pressure $B_0^2/2\mu$. In the corona, $\beta \approx 10^{-3}$ and in a prominence, $\beta \approx 10^{-2}$. Thus, magnetic forces dominate pressure variations so that it is difficult for plasma motions to distort the field.

2.3.1 Force-Free Fields

If the typical length-scales of a coronal structure, such as a prominence, are much less than the coronal scale-height then gravitational forces may be neglected when compared to plasma pressure gradients. In addition, if the plasma beta is much less than unity, these pressure gradients are negligible in comparison to Lorentz forces. If these two cases hold then the equation of magnetohydrostatic equilibrium (2.13) reduces to

$$\mathbf{j} \times \mathbf{B} = \mathbf{0} \ . \tag{2.18}$$

Magnetic fields satisfying this condition are said to be "force-free". In this approximation, no significant Lorentz force can result because any pressure gradients would be too weak to balance it. (2.18) implies that the electric current must flow along magnetic field lines and by using (2.5) it may be rewritten

$$(\nabla \times \mathbf{B}) \times \mathbf{B} = \mathbf{0} \ , \tag{2.19}$$

and so

$$\nabla \times \mathbf{B} = \alpha \mathbf{B} \ , \tag{2.20}$$

where α is some function of position. Taking the divergence of (2.20) yields

$$(\mathbf{B} \cdot \nabla)\alpha = 0 \ , \tag{2.21}$$

since $\nabla \cdot \mathbf{B} = 0$. Thus, α is constant along a field line or, alternatively, $\mathbf{B}$ and $\mathbf{j}$ lie on surfaces of constant α. When α is constant, the curl of (2.20) reduces to

$$(\nabla^2 + \alpha^2)\mathbf{B} = \mathbf{0} \ , \tag{2.22}$$

which is the equation of a constant-α or linear force-free field. In general, (2.19) does not reduce to a linear equation and solutions are particularly difficult to find. In this case, progress can be made by assuming the field to be invariant in one direction. For prominence models, this is usually taken to be the direction of the prominence long axis, which we specify to be the $\hat{\mathbf{z}}$-direction here. Writing the field in terms of a vector potential

$$\mathbf{B} = \nabla \times \mathbf{A} \ , \tag{2.23}$$

ensures that $\nabla \cdot \mathbf{B} = 0$ is satisfied. Taking

$$\mathbf{A} = A(x, y)\ \hat{\mathbf{z}} \ ,$$

where $A(x, y)$ is a scalar flux function, gives the following expression for $\mathbf{B}$ in Cartesian coordinates:

$$\mathbf{B} = \left(\frac{\partial A(x,y)}{\partial y}, -\frac{\partial A(x,y)}{\partial x}, B_z(x,y) \right) \ , \tag{2.24}$$

where a third field component, $B_z(x, y)$ is included. After substitution of (2.24) in (2.19) and equating the components it can be shown that

$$B_z = B_z(A) \qquad \text{and} \qquad \nabla^2 A + \frac{d}{dA}\left(\frac{B_z^2(A)}{2} \right) = 0 \ . \tag{2.25}$$

This is a form of the Grad-Shafranov equation, derived independently by Lust and Schlüter (1957), Shafranov (1958), and Grad and Rubin (1958) for non-constant-α force-free fields. It can be verified that $(\mathbf{B} \cdot \nabla)A = 0$ and so A (and hence B_z) is constant along field lines.

The Grad-Shafranov equation may be solved for A if $B_z(A)$ is prescribed and then (2.24) allows the field components B_x and B_y to be explicitly determined. For example, taking $B_z(A) = \alpha A$ implies that

$$(\nabla^2 + \alpha^2)A = 0 \ .$$

This is the linear Helmholtz equation which yields constant-α force-free fields. Taking $B_z(A) = 2\alpha A^{\frac{1}{2}}$ implies that

$$\nabla^2 A = -2\alpha^2 \ ,$$

which is Poisson's equation corresponding to a constant current force-free field. The twisted flux tube model presented in Chapter 3 uses such a field. Other forms of $B_z(A)$ for which there are known analytical solutions are $B_z(A) = e^{-2A}$ and $B_z(A) = A^{-1}$.

An important case occurs for which $B_z(A) = \alpha$. Here we obtain

$$\nabla^2 A = 0 \ ,$$

which implies that the electric current is zero. These are *potential* fields in which there are no volumetric currents and are discussed in the next section.

2.3.2 Potential Fields

When $\mathbf{j} = \mathbf{0}$, (2.5) implies that

$$\nabla \times \mathbf{B} = \mathbf{0} \ , \tag{2.26}$$

and so no electric currents are generated through gradients in the magnetic field. Keeping the assumption that all quantities are independent of z, the x and $y-$components of (2.26) require that B_z must now be constant and the z-component gives

$$\frac{\partial B_y}{\partial x} = \frac{\partial B_x}{\partial y} \ . \tag{2.27}$$

Also, from (2.2) we have

$$\frac{\partial B_x}{\partial x} = -\frac{\partial B_y}{\partial y} \ . \tag{2.28}$$

We now note that (2.27) and (2.28) take the form of Cauchy-Riemann equations, the general solution of which is given by an analytic function

$$B(w) = B_y + i \ B_x \ , \tag{2.29}$$

of the complex variable $w = x + i \ y$.

Furthermore, we can define a holomorphic function (or complex flux function), $F(w)$, given by

$$F(w) = A(x, y) + i \ \Phi(x, y) \ , \tag{2.30}$$

and so $\mathbf{B}$ may be written as

$$\mathbf{B} = -\nabla\Phi \ , \text{ or } \qquad \mathbf{B} = \nabla \times (A\hat{\mathbf{z}}) \ ,$$

or

$$B(w) = -\frac{dF}{dw} \ . \tag{2.31}$$

Then

$$A(x,y) = \mathrm{Re}\left\{\int -B(w)\ dw\right\} = \text{constant}\ ,$$

defines field lines and

$$\Phi(x,y) = \mathrm{Im}\left\{\int -B(w)\ dw\right\} = \text{constant}\ ,$$

defines orthogonal curves to the field lines.

Equation (2.29) allows the field to be written in terms of a single complex variable, w, and so many of the powerful tools of complex variable theory may be applied. For example, in Appendix A the integrals over an infinite domain are transformed to contour integrals and easily evaluated by seeking the appropriate residues; branch cuts in the complex plane can be used to represent discrete current sheets (Chapters 4, 6, 7) since they are the location of a tangential discontinuity in $B(w)$; and conformal mappings may be used to transform the geometry of these fields to produce additional solutions (Aly and Amari, 1989). This latter technique is not used in this thesis, but the related work of Amari (1988) provides good evidence of the versatility of this method.

Now we have introduced the relevant equations and techniques we present a short review of important existing models for the equilibrium of quiescent solar prominences.

2.4 Summary of Prominence Models

This summary of significant magnetohydrostatic equilibrium models is intended to provide the background information for subsequent chapters. It is by no means a complete review as we only focus on particular models which describe the external and internal equilibrium properties of quiescent prominences and the surrounding magnetic field. For additional information on this subject the books and conference proceedings by Tandberg-Hanssen (1974), Poland (1986), Priest (1989) and Ruzdjak and Tandberg-Hanssen (1989) provide an extensive range of contributed papers and reviews on all aspects of theoretical modelling.

2.4.1 External Models

First we consider some important models which concentrate on the global equilibrium of prominences. In these models the prominence is represented either by a line current or a current sheet supported in an external force-free or potential coronal magnetic field. Priest (1989) suggested that such models can be categorised as either *normal polarity* or *inverse polarity*, depending on whether the magnetic field passes through the prominence in the same direction as the underlying photospheric field or the opposite direction, respectively.

The development of such models began with Kippenhahn and Schlüter (1957) who gave a simple model for the support of a prominence in a normal-polarity configuration. The basic topology is shown in Figure 2.1 where the prominence is represented as a sheet

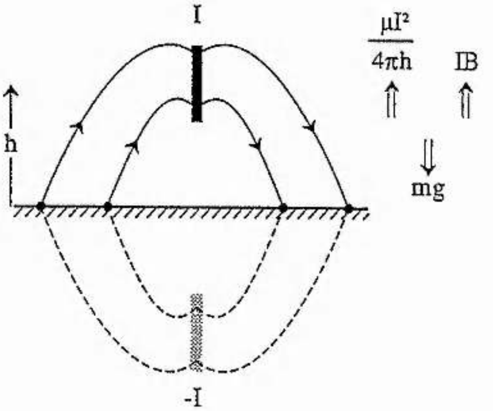

Figure 2.1: The external potential field of the Kippenhahn-Schlüter model showing also the image sheet (-I) and the associated forces.

with current I at a height h above the photosphere. The current is directed out of the plane and results from a discontinuity in the vertical field component. If the photospheric footpoints are line-tied during the formation of the prominence, the preservation of the footpoint position can be modelled by adding an image current $(-I)$ at a distance h below the photosphere to the original arcade and prominence sheet. Thus the prominence mass m is supported against gravity both by the line tying (the repulsion $\mu I^2/(4\pi h)$ between I and (-I)) and also by the Lorentz force IB acting on I in the original background field B at height h.

An alternative magnetic topology (inverse-polarity) was proposed by Kuperus and Raadu (1974) where the magnetic field passes through the prominence in the opposite direction. They represent the prominence by a line current embedded in the background field of a vertical neutral sheet. Again, to simulate the line-tying during the formation, an image current is required and this provides the upward repulsive force $\mu I^2/(4\pi h)$ to balance

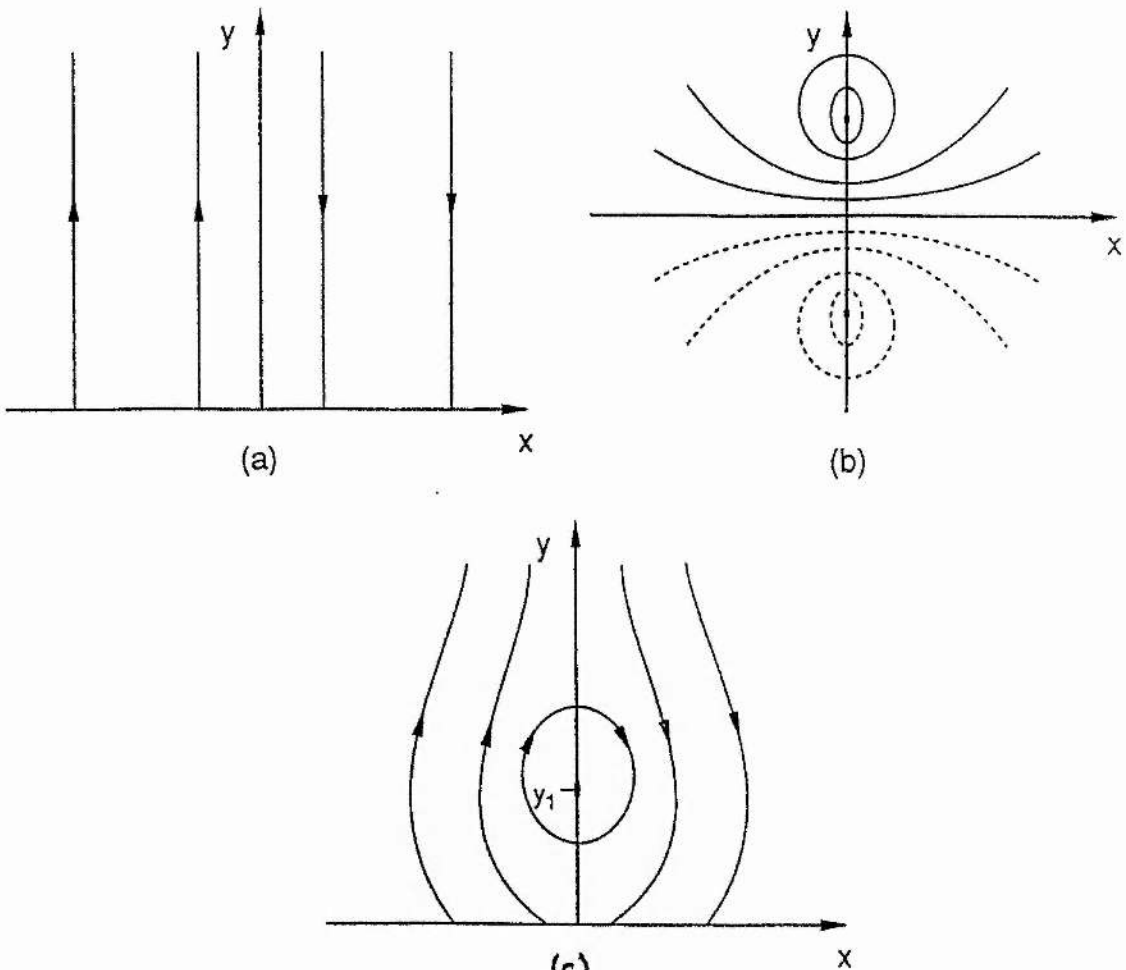

Figure 2.2: The Kuperus-Raadu solution. The final equilibrium (c) is obtained from the superposition of the neutral sheet field (a) and the line current system (b).

the weight of the filament. A unique equilibrium position for the prominence can then be found from the balance of forces. Figure 2.2 shows the construction of this solution. In this case the current in the filament must be in the opposite direction to the Kippenhahn-Schlüter sheet and Anzer (1984) postulated that this may be achieved through an upward stretching and opening of the arcade field through the action of the solar wind or an MHD instability. For the Kippenhahn-Schlüter case, the correct current sign may be produced by a simple deformation of the arcade due to gravity. Anzer and Priest (1985) developed

Anzer's idea by considering a current sheet which has formed due to the opening of the field. In their model the current sheet moves downward, cools and contracts to a line filament of inverse polarity. However, if the current is conserved, the final equilibrium position of the filament is lower than the observed prominence heights. They tried to extend this model to incorporate a vertical current sheet but the upper part of the sheet is not in local equilibrium. Anzer (1989) explained that this is a common defect of inverse-polarity current sheet models and occurs because the internal attraction of the current elements in the sheet gives rise to a self-pinching effect. This results in a downward force on the upper part of the sheet which dominates over the repulsion force from the image sheet and hence there is no equilibrium.

Models of Kuperus-Raadu type have the appealing feature that the prominence is located within a region of *closed* magnetic field. Thermal conduction is weak across field lines and so this type of configuration helps to shield the prominence from the corona and keep it in a cool equilibrium. Low and Hundhausen (1995) have suggested that such closed field lines may form the coronal cavity which is observed to surround prominences.

Van Tend and Kuperus (1978) and Kuperus and Van Tend (1981) extended the work of Kuperus and Raadu by allowing for an additional background field. Given the form of this field they found that increasing the current I results in a state of non-equilibrium when it exceeds a critical value, possibly leading to a dynamic evolution such as an eruption.

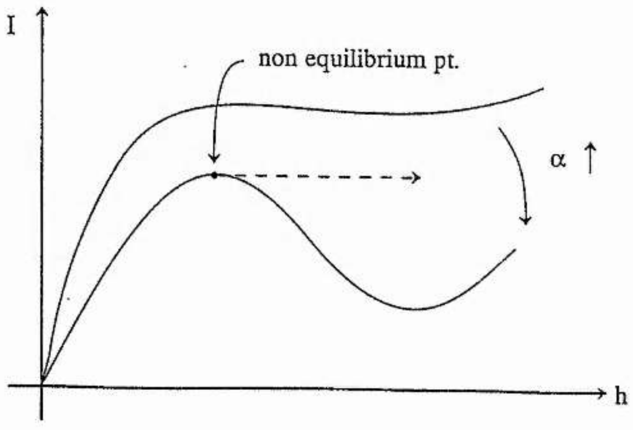

Figure 2.3: The variation of $I(h)$ as α, the shear parameter, is adjusted in the model of Démoulin and Priest.

However, the weak feature of their order of magnitude model is that the background field is imposed in an ad hoc manner. Amari and Aly (1989) gave a more detailed analysis including the ambient field in a self-consistent manner. Once again, they modelled the prominence as a line of mass and current, but this time supported in a constant-α force-free field in which the flux function satisfies

$$\nabla^2 A + \alpha^2 A = \delta(x)\delta(y-h) ,$$

where the delta functions represent the line current at $x = 0$, $y = h$. When the current is negative the field is of inverse polarity and when I is positive it is of normal polarity. They did not find a state of non-equilibrium, but this was discovered by Démoulin and Priest (1988) when they generalised the work to include the second harmonic of the basic arcade field. They found that the prominence can erupt when the current and a shear parameter, α, are too large since the functional form of $I(h)$ changes from monotonic to one with a maximum and minimum as shown in Figure 2.3.

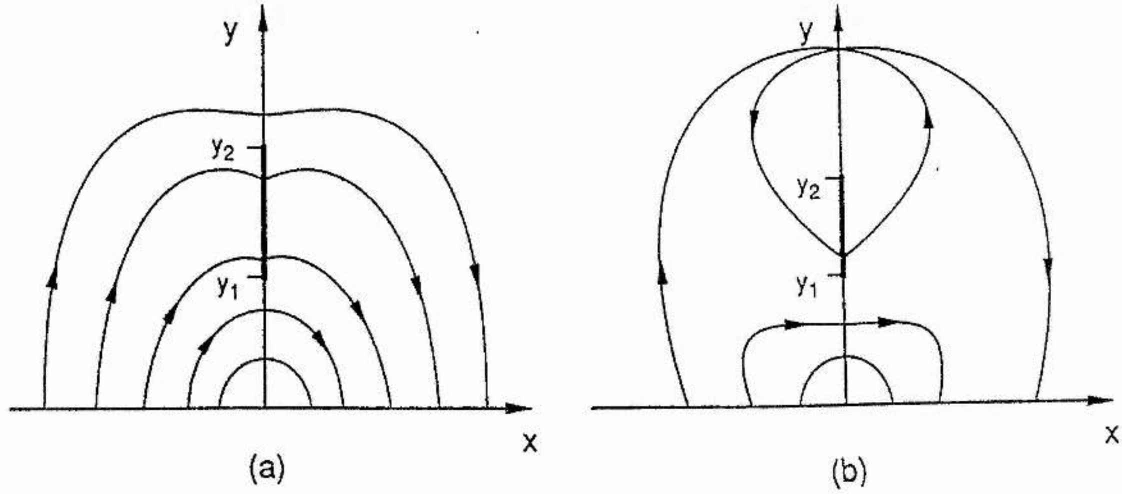

(a) (b)

Figure 2.4: Examples of Malherbe-Priest configurations showing normal-polarity ((a), (b)) and inverse-polarity ((c), (d)) prominence solutions.

Malherbe and Priest (1983) used complex variable theory to generate prominence equilibria in potential magnetic fields. They found particular solutions of both normal and inverse polarity in which the prominence sheet is represented as a branch cut in the complex plane. It is supported against gravity by the tension forces from the discontinuous vertical

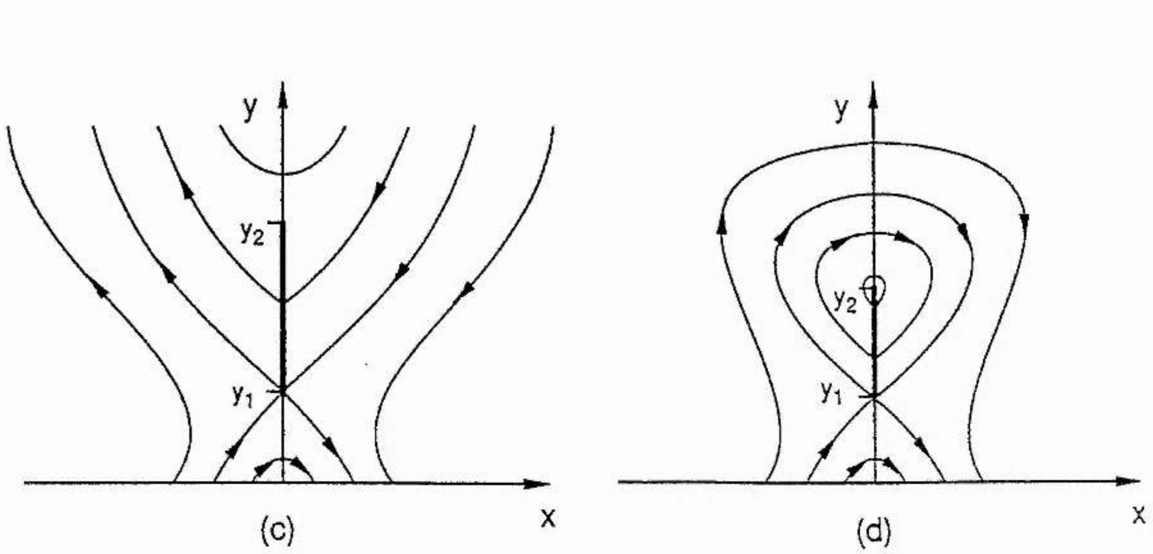

Figure 2.4

field component. Examples of some of their solutions are shown in Figure 2.4. They also examined the effect of slow ($< 100\ ms^{-1}$) converging and diverging photospheric flows at the base of the magnetic structures and suggested that these are responsible for the upward plasma motions observed by Malherbe et al. (1983). The method of inspection used by Malhèrbe and Priest produces a large class of prominence models and is a very valuable technique. However, it does not allow the observable properties (e.g. the normal field

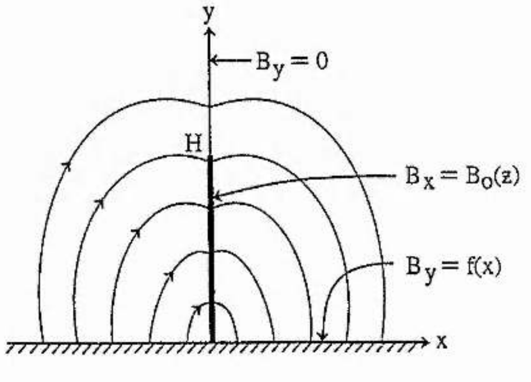

Figure 2.5: Anzer's normal-polarity current sheet model.

component in the prominence and the photosphere) to be prescribed *a priori*. This requires a different approach which was first applied by Anzer (1972). He considered the problem in which the normal field components are imposed as functions of position at the photosphere and across the current sheet which extends from the photosphere to a finite height as sketched in Figure 2.5. Assuming a potential field to exist outside the sheet, the resulting mixed boundary-value problem can be solved to obtain the field throughout the corona. Unfortunately, the numerical solutions he found are unphysical due to a downward Lorentz force acting in the lower part of the sheet. This problem was resolved by Démoulin et al. (1989) by considering the base of the prominence sheet to be detached from the photosphere. This introduces a free parameter (the flux between the base of the sheet and the photosphere) which can be physically adjusted to give the correct behaviour of the Lorentz force. They were able to find both normal and inverse-polarity solutions using this formulation. More recently, Ridgway, Amari and Priest (1991, 1992) have made significant developments by generating current sheet solutions in a constant-current force-free field for both normal and inverse-polarity topologies, although not all of their solutions are bounded. Amari and Aly (1990, 1992) gave a method to calculate bounded solutions for current sheets in a constant-α force-free field but their inverse-polarity configurations are still subject to the self-pinching effect at the top of the sheet.

Priest et al. (1989) proposed a twisted flux tube model to give better agreement

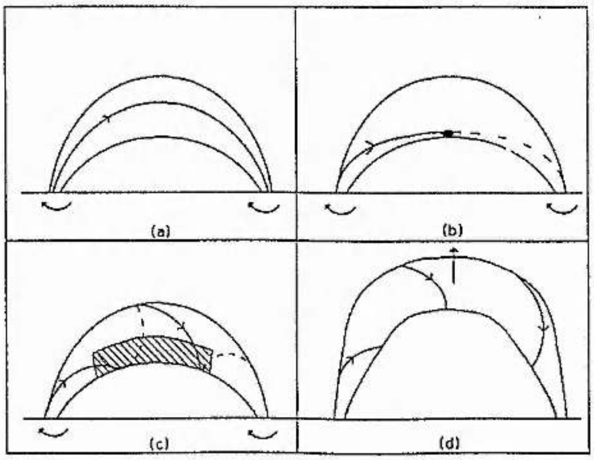

Figure 2.6: The Priest, Hood and Anzer twisted flux tube model showing the various stages as the twist is increased.

with some of the observed features. For example, against the disc active-region prominences often display plasma motions in a transverse direction, i.e. along the long-axis of the prominence. Also, these prominences sometimes appear to have one end rooted in a sunspot. Both of these features contradict the Kippenhahn-Schlüter model. The scenario for the model is shown in Figure 2.6 in which the basic geometry is a large-scale curved flux tube. Twist of the tube may be created by general evolutionary footpoint motions, Coriolis forces or flux cancellation. As the twist increases, a dip with upwards curvature is created at the summit of the tube and at this point the prominence can form either by condensation or chromospheric injection of plasma (Figure 2.6b). The existence of dipped field lines is a necessary condition for formation by thermal condensation as it creates a well in which material can collect without falling down to the solar surface. As twisting or flux-cancellation continues, the prominence grows in length (Figure 2.6c) and ultimately, when the twist or prominence length is too large, the tube becomes unstable and the prominence erupts, filling the tube with plasma and revealing the helical structure for the first time (Figure 2.6d). A classic example of this is in the huge eruptive prominence in Figure 1.10 where the twist is particularly evident.

Van Ballegooijen and Martens (1989) presented an alternative mechanism through which the helical structure is formed via reconnection processes, driven by converging photospheric motions that act on a sheared arcade (Figure 2.7). Initially, a potential arcade

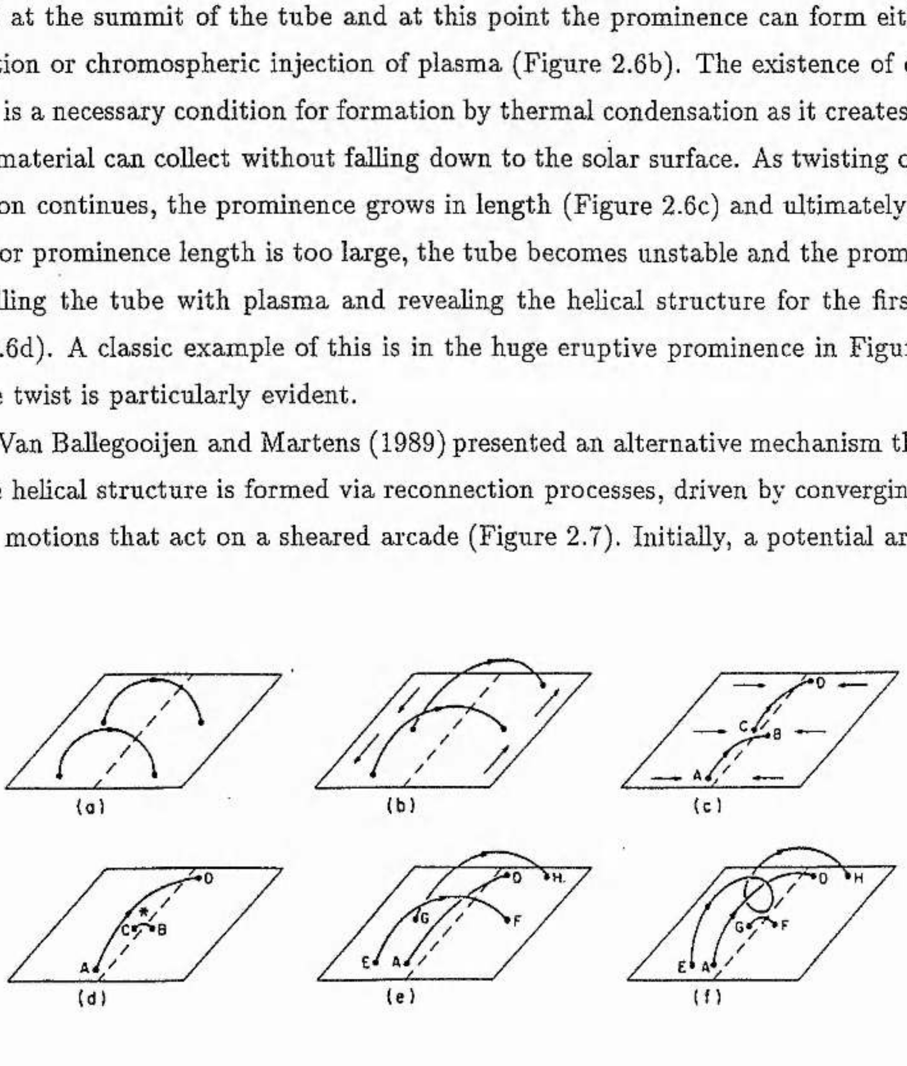

Figure 2.7: The model of Van Ballegooijen and Martens which provides a possible solution for the formation and eruption of a twisted flux tube.

is sheared due to photospheric motions parallel to the polarity inversion line. Converging motions then bring the footpoints of the sheared field lines together so that strong current gradients are produced and the effects of magnetic diffusion are no longer negligible. This allows field lines to reconnect, producing a short, highly curved field line (which submerges due to the magnetic tension forces) and a long field line around which subsequently reconnected field lines wrap themselves. In this way, a helical structure is formed along the polarity inversion line in which dense material can collect in the lowest points of the helical windings. Eventually, the overlying arcade is unable to confine the flux tube, allowing it to erupt. The 'cancelling magnetic features' which occur as the reconnected field lines submerge are in good agreement with the videomagnetographs of Martin (1986,1990).

Ridgway, Priest and Amari (1991) found constant-current force-free solutions for the local equilibrium of a prominence sheet in a twisted flux tube, neglecting the large-scale curvature of the tube, although in their solution the sheet does not vanish at the edge of the flux tube. That is a feature which we rectify in Chapter 3 by considering further harmonics in the series solution.

We conclude our discussion on external models by considering a particular category of prominences to which little theoretical attention has been paid in the past. These are *polar-crown prominences* and are almost always observed to be of inverse polarity (Leroy et al., 1983). In a recent paper, Démoulin and Priest (1993) suggested a modification to a

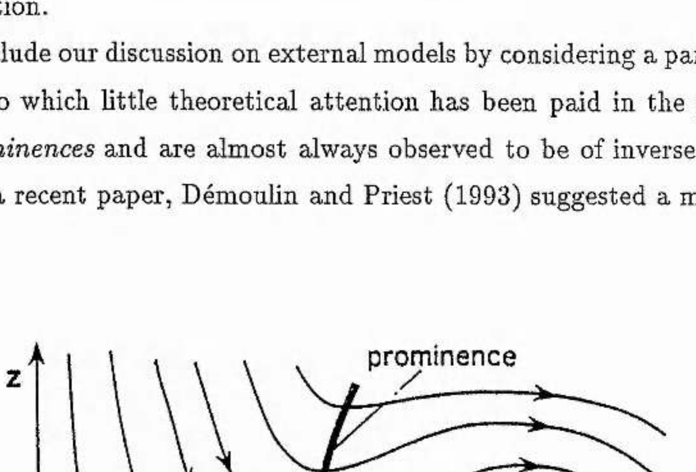

Figure 2.8: A possible topology for a polar-crown prominence suggested by Démoulin and Priest.

quadrupolar configuration could be used to model these prominences. Their idea is given in the sketch in Figure 2.8 but they did not proceed with any calculations. Anzer (1993) has stressed the need for a reasonable polar-crown prominence model and in some preliminary calculations using appropriate flux distributions he reported that he could not find a suitable configuration with field line dips (Anzer, 1994) although his study was not exhaustive. In Chapters 4 and 5 we are able to overcome this difficulty and find solutions for the equilibrium of a polar-crown prominence.

2.4.2 Internal Models

As in the previous section, an appropriate place to start is with the internal model proposed by Kippenhahn and Schlüter (1957). They set up a simple model for the magnetohydrostatic support of a vertical sheet of material by assuming that the temperature (T) and the horizontal field components (B_x, B_z) are constant while the vertical field B_y, pressure p, and density ρ, depend on x alone. The horizontal and vertical components of the force balance equation (2.13) then reduce to

$$p + \frac{B_y^2}{2\mu} = \frac{B_{y0}^2}{2\mu} \tag{2.32}$$

and

$$\frac{dB_y}{dx}\frac{B_x}{\mu} - \rho g = 0 \ , \tag{2.33}$$

where B_y approaches $\mp B_{y0}$ as x tends to $\pm\infty$ and p approaches zero. The magnetic field plays two roles. According to (2.32) it compresses the plasma sheet laterally and increases the plasma pressure in the sheet by a small amount equal to the external magnetic pressure ($B_{y0}^2/2\mu$) associated with the vertical field. In addition (2.33) indicates that the tension in the magnetic field supports the plasma against gravity. The solution of (2.32) and (2.33) may be written as

$$B_y = -B_{y0}\tanh(x/l) \ , \qquad p = (B_{y0}^2/2\mu)\text{sech}^2(x/l) \ , \tag{2.34}$$

where the prominence half-width l is given by

$$l = 2\frac{B_x}{B_{y0}}H \ ,$$

H being the prominence scale-height. Figure 2.9a shows the field lines through the prominence interior.

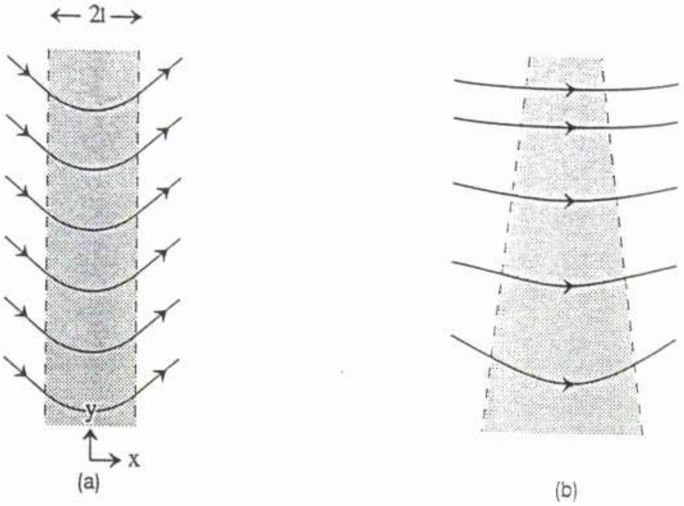

Figure 2.9: (a) The internal Kippenhahn-Schlüter model in which the curved field lines support dense prominence material. (b) A modification to the K-S model to include variations with height.

Several generalisations of this solution have been constructed. Poland and Anzer (1971) allowed for imposed spatial variations $T(x)$ of the temperature so that

$$B_y = B_{y0} \tanh \int_0^x dx/l(x) \; .$$

Low (1975) also found hydrostatic equilibria with the temperature varying as

$$T \sim A^{\frac{2}{7}} \; ,$$

where A is the flux function. The resulting solution has the property that the magnetic field tends to a constant value as $|x| \to \infty$ and therefore $A \to \text{const} \times |x|$ This implies that $T \to \text{const} \times |x|^{2/7}$ and so the temperature tends to infinity at large distances. Thus, taking a low prominence temperature at $x = 0$ allows the temperature profile to reach coronal values for large enough values of x. Beyond this value the solutions become unphysical, though, and so they must be somehow matched onto a correct coronal solution.

Milne et al. (1979) coupled the magnetohydrostatics to a simple energy balance equation and found that the solutions depend on the plasma beta and the prominence shear angle. Prominence-like solutions are found when β is less than a critical value.

A further modification was presented by Ballester and Priest (1987) to allow slow variations with height by writing the magnetic field as

$$\mathbf{B} = \mathbf{B}_0(x) + \epsilon \mathbf{B}_1(x, y) ,$$

where $\mathbf{B}_0(x)$ is the Kippenhahn-Schlüter solution. The result is that the width of the prominence decreases slowly with height (Figure 2.9b), while the field lines become less curved and the field strength increases, in agreement with observations.

In order to compute a more complete prominence solution it is necessary to match the external current sheet solution onto an appropriate internal solution. Hood and Anzer (1990) achieved this and found a global model for a normal-polarity prominence in which a cool, internal MHS solution matches onto a hot, external arcade solution with field lines rooted in the photosphere. A sketch of their matched field lines is shown in Figure 2.10.

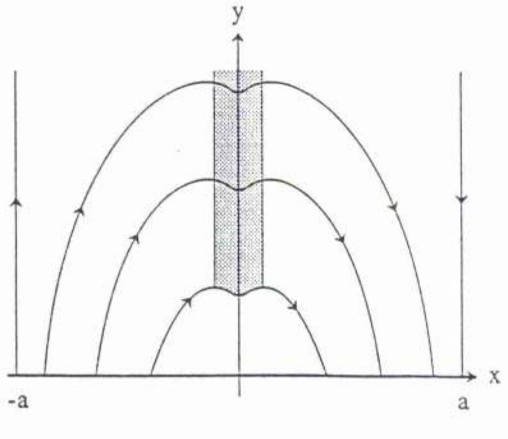

Figure 2.10: The field lines in the Hood-Anzer prominence model showing how the current sheet has been replaced by a finite internal region.

In Chapters 6 and 7 we construct matched internal-external solutions for a polar-crown prominence model in which the support of slanted and curved material is required. Firstly, though, we present a modification to the twisted flux tube model of Ridgway, Priest and Amari (1991) which includes both a finite-height current sheet and an appropriate matched internal solution.

Chapter 3

Twisted Flux Tube Prominence Model

3.1 Chapter Summary

In this chapter the twisted flux tube model for the support of a prominence sheet with constant axial current density, given by Ridgway, Priest and Amari (1991), is considered.

The model is extended in Section 3.3 to incorporate a current sheet of finite height. The sheet is supported in a constant current density force-free field in the configuration of a twisted flux tube. The mass of the prominence sheet, using a typical height and field strength, is computed. Outside the flux tube the background magnetic field is assumed to be potential but the matching of the flux tube onto this background field is not considered here.

Instead our attention is focussed, in Section 3.4, on the interior of the prominence. An expanded scale is used to stretch the prominence sheet to a finite width. We analytically select solutions for the internal magnetic field in this region which match smoothly onto the external force-free solutions at the prominence edge.

The force balance equation applied inside the prominence then yields expressions for the pressure and density and a corresponding temperature may be computed.

3.2 Introduction

Theoretical prominence models have tended to fall into one of two groups. These are current sheet and internal models. *Current sheet* models assume that the prominence thickness is so small, when compared with coronal length scales, that it is replaced by a current sheet. This allows a surface with a jump in the vertical magnetic field component. If the external coronal field is potential, then complex variable theory can be used to describe this field and the current sheet becomes a branch cut in the complex plane. This technique has been used by several authors (see for example Anzer (1972); Malherbe and Priest (1983); Démoulin, Malherbe and Priest (1989)). The basic idea of replacing the prominence by a current sheet has been used by Amari and Aly (1990) for a linear, force-free coronal field and by Ridgway, Amari and Priest (1991,1992) for a constant current density coronal field. All of these authors have assumed Cartesian geometry that is invariant in the axial direction.

Recently it has been proposed that a prominence can form inside a large, twisted, flux tube. Priest et al. (1989) suggested that slow twisting motions could create the necessary magnetic field line dip for the formation of a prominence. They proposed that, after the formation of a cool condensation, a current sheet would form but now in cylindrical geometry. Depending on the source of twist either a normal or inverse polarity prominence can be formed. Van Ballegooijen and Martens (1989) suggested that a twisted, flux tube could be formed by suitable shearing and converging photospheric flows and magnetic reconnection. The resulting prominence will always be of inverse polarity type. Their ideas were based on an earlier model by Pneuman (1983) although the mechanisms by which the flux tube is formed are different. Pneuman considered the emergence of a bipolar region which is distented outward, into the corona, by pressure gradients. At low heights the pressure forces cannot balance the Lorentz force, provided the field lines remain line-tied. This causes an inward collapse of the field and subsequent reconnection at the neutral line occurs to form the helical flux tube. Inhester et al. (1992) extended this idea of flux tube formation in a detailed numerical simulation. A natural result of the formation of a twisted, flux tube is an enhanced density that could trigger prominence formation.

An investigation of a current sheet prominence model in a twisted, flux tube was carried out by Ridgway, Priest and Amari (1991). Their model was based on a constant axial coronal current density and contained no singularities near the origin. They showed that a current sheet could be in equilibrium out to the edge of the flux tube. Anzer (1989) explains that this equilibrium is of fundamental importance and can only be achieved if the Lorentz force is directed vertically upwards at every point in the sheet. However, one weakness of their model, that will be rectified in this chapter, in Sections 3.3.3 and 3.3.4, is that the current sheet does not vanish at the outer edge. This will create problems when matching to an unsheared external field.

One important drawback to all current sheet models is that the internal prominence structure is not considered and quantities like the density and pressure are determined from horizontal and vertical force balance and are not free to be chosen. *Internal models* consider the local behaviour within the prominence without worrying about matching onto a suitable external magnetic field. The isothermal models of Menzel (1951) and Brown (1958) have been extended to a non-isothermal model proposed by Hood and Anzer (1990) that links the internal and external fields in a self-consistent manner giving the typical structure of a normal-polarity prominence. A two-temperature prominence, of finite height, has been investigated in the numerical studies of Fiedler and Hood (1992, 1993). Thus, it is important that any internal solution matches onto a realistic external equilibrium solution. This will be considered in Section 3.4.

There have been many publications on magnetic equilibria of coronal fields that could be used in a prominence model. The main requirement is the existence of a dip in the field. Some of the recent 3-D equilibria presented by Low (1991; see references within) offer possibilities of modelling realistic coronal fields.

This chapter is concerned with the twisted, magnetic flux tube model of prominences. The flux tube is represented in cylindrical coordinates and is assumed independent of variations in the axial direction. In Section 3.3 the basic equations and a current sheet model for constant axial current density is presented. Section 3.4 "expands" the current sheet giving an internal description of the prominence. The internal solution is matched onto the previous external solution. Finally the results and conclusions are discussed in the last section.

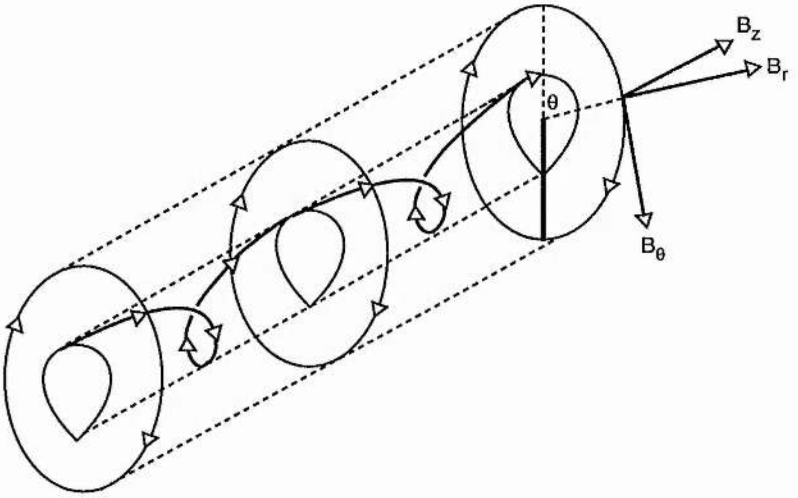

Figure 3.1: The notation used for a flux tube in which a current sheet is supported along the line $\theta = \pi$.

3.3 Current Sheet Prominence Model

3.3.1 Basic Solution

The basic geometry is shown in Figure 3.1. A cylindrical geometry is taken in which the magnetic field is assumed to be invariant in the axial direction. In cylindrical coordinates the magnetic field can be represented in terms of a flux function $A(r, \theta)$ as

$$\mathbf{B} = \left(\frac{1}{r}\frac{\partial A}{\partial \theta}, -\frac{\partial A}{\partial r}, B_z(A)\right) , \tag{3.1}$$

where the arbitrary function $B_z(A)$ is selected as

$$B_z(A) = 2cA^{\frac{1}{2}} . \tag{3.2}$$

Thus, for realistic solutions (B_z real) we require the external boundary of the flux tube to lie on $A(r, \theta) = 0$ so that the flux tube region is defined by $A(r, \theta) \geq 0$. The surface $A = 0$

is not a cylindrical one (there is a radial dependence on θ) but $B_z(A=0)=0$ so the field can be matched to an unsheared external potential field there.

In addition, there is a background hydrostatic atmosphere, based on an isothermal corona,

$$p = p_o e^{-r\cos\theta/H} \ , \qquad \rho = \rho_o e^{-r\cos\theta/H} \ , \tag{3.3}$$

for the pressure and density. The pressure scale height is defined as

$$H = \frac{RT}{\tilde{\mu} g} = \frac{P_o}{\rho_o g} \ , \tag{3.4}$$

with the choice of $B_z(A)$ given by (3.2) and using (3.3) the force balance equation

$$\nabla p = \frac{1}{\mu}(\nabla \times \mathbf{B}) \times \mathbf{B} + \rho g \ ,$$

reduces to

$$\nabla^2 A + 2c^2 = 0 \ . \tag{3.5}$$

Thus, the axial current density, $-\nabla^2 A$, is a constant. (3.5) may be solved by superimposing a non-potential, cylindrically symmetric solution A_p that has no current sheet, and a potential solution A_c that does possess a current sheet. The cylindrically symmetric field is simply the particular solution

$$A_p = \frac{c^2}{2}(h^2 - r^2) \ , \tag{3.6}$$

where h is a constant. The potential solution

$$\nabla^2 A_c = 0 \ ,$$

can be obtained using complex variable theory but we restrict attention to simple separable solutions of the form

$$A_c = \sum_k b_k r^k \cos k\theta \ . \tag{3.7}$$

To avoid singularities in the current at $r=0$ we require $k \geq 1$, but a sign change in B_θ within the flux tube is only avoided by taking $k \geq 2$. For non-integer values of k there is a current sheet, or equivalently a jump in the value of B_r at $\theta = \pm\pi$. For simplicity we restrict k to

$$k = n + \frac{1}{2} , \qquad n \geq 2 . \tag{3.8}$$

Finally, we give some physical meaning to the constant c by defining the field strength to be B_0 at $r = 0$. Hence,

$$c^2 = \frac{B_0}{\sqrt{2}h} . \tag{3.9}$$

Thus, the flux function is given by

$$A = A_p + A_c = \frac{\sqrt{2}B_0}{4h}(h^2 - r^2) + \sum_{n=2}^{\infty} b_n r^{n+\frac{1}{2}} \cos(n + \frac{1}{2})\theta , \tag{3.10}$$

for $A > 0$. Special solutions are now presented that depend on the number of terms considered in the series.

3.3.2 One Term in the Series in (3.10)

Following Ridgway, Priest and Amari (1991), only one term in the series in (3.10) is considered. Thus

$$A = \frac{B_1}{h}(h^2 - r^2) + b_2 r^{\frac{5}{2}} \cos\frac{5\theta}{2} , \tag{3.11}$$

where $B_1 = \sqrt{2}B_0/4 > 0$.

If we scale r so that $r = \hat{r}h$ and define $\lambda = b_2 h^{3/2}/B_1$ then

$$A = B_1 h \left[(1 - \hat{r}^2) + \lambda \hat{r}^{\frac{5}{2}} \cos\frac{5\theta}{2}\right] ,$$

giving field components

$$\begin{aligned} B_r &= \frac{1}{h\hat{r}}\frac{\partial A}{\partial \theta} = \frac{5}{2}B_1(-\lambda)\hat{r}^{\frac{3}{2}} \sin\frac{5\theta}{2} , \\ B_\theta &= -\frac{1}{h}\frac{\partial A}{\partial \hat{r}} = 2B_1\hat{r} + \frac{5}{2}B_1(-\lambda)\hat{r}^{\frac{3}{2}} \cos\frac{5\theta}{2} . \end{aligned} \tag{3.12}$$

For a current sheet at $\theta = \pi$ that provides support, $B_r(\hat{r}, \pi)$ must be positive, since $B_\theta(\hat{r}, \pi) > 0$, and so $-\lambda > 0$.

The mass density of the current sheet, per unit area m_A, was obtained by Ridgway, Priest and Amari (1991) as

$$m_A(\hat{r}) = \frac{[B_r](\hat{r})\ B_\theta(\hat{r},\pi)}{\mu\ g}\ , \tag{3.13}$$

where $[B_r]$ is the jump in B_r across the prominence from $\theta = -\pi$ to $\theta = \pi$. Thus

$$[B_r](\hat{r}) = 5B_1(-\lambda)\ \hat{r}^{\frac{3}{2}}\ . \tag{3.14}$$

Pressure balance across the prominence gives the plasma pressure at the sheet as

$$p = \frac{1}{8\mu}[B_r]^2\ .$$

As we have mentioned, A must be positive for real values of B_z (equation 3.2) so that $A = 0$ defines the outer surface of the flux tube, passing through the line $(r = h,\ \theta = \pi)$. Outside this surface a potential field can be matched onto this solution.

However, in general it is only possible to match the average field strength around this surface and the boundary is not in equilibrium. The one exception to this situation is when the boundary is circular. Low (1993) used image currents to make this matching surface circular and derived a consistent equilibrium for both regions. This analysis can be done but the complexity of the solutions obscures the properties of the field and current sheet without substantially altering the behaviour.

There is also a surface inside which B_θ is always positive and there is an X-type neutral point at

$$\begin{aligned} B_r &= 0 \quad , \quad \theta = \frac{2\pi}{5}\ , \\ B_\theta &= 0 \quad , \quad \hat{r} = \left[\frac{4}{5(-\lambda)}\right]^2\ . \end{aligned} \tag{3.15}$$

Note that this is not a neutral point of the 3-D field, as $B_z \neq 0$. It is a neutral point of the projected field onto the (r, θ) plane. Figure 3.2c illustrates such a projection. The restriction that this X-type neutral point lies *outside the edge of the current sheet flux tube*, defined by $A = 0$, bounds the value of $-\lambda$. Thus, there is a maximum value for the potential solution when compared with the non-potential field. Using (3.15) and (3.11) gives

$$-\lambda \leq \frac{4}{5^{5/4}} = 0.535\ . \tag{3.16}$$

Ridgway, Priest and Amari (1991) do not mention this restriction. However, their field line plots are still valid since their parameter choices satisfy this constraint.

One obvious weakness of solution (3.12) is that B_r, and hence the current density in the current sheet, increases with radius. Thus, the current density is non-zero at the outer edge of the flux tube. This is rectified in the next section.

3.3.3 Two Terms in the Series in (3.10)

Consider two terms in the series for $A(r,\theta)$ so that

$$A = B_1 h \left[(1-\hat{r}^2) + \frac{b_2 h^{\frac{3}{2}}}{B_1} \hat{r}^{\frac{5}{2}} \cos\frac{5\theta}{2} + \frac{b_3 h^{\frac{5}{2}}}{B_1} \hat{r}^{\frac{7}{2}} \cos\frac{7\theta}{2} \right] . \tag{3.17}$$

Now $A(\hat{r}=1,\pi)=0$ defines the edge of the flux tube and

$$0 \le \hat{r} \le 1 .$$

If, additionally, we take $b_3 = 5b_2/7h$ we can satisfy $[B_r](\hat{r}=1)=0$ and so the current sheet has a finite height.

Thus, we have

$$A = B_1 h \left[(1-\hat{r}^2) + \lambda \hat{r}^{\frac{5}{2}} \left(\cos\frac{5\theta}{2} + \frac{5}{7}\hat{r}\cos\frac{7\theta}{2} \right) \right] , \tag{3.18}$$

with λ defined as before.

The field components are

$$\begin{aligned} B_r &= \frac{5}{2}\hat{r}^{\frac{3}{2}} B_1(-\lambda) \left[\sin\frac{5\theta}{2} + \hat{r}\sin\frac{7\theta}{2} \right] , \\ B_\theta &= 2B_1\hat{r} + \frac{5}{2}\hat{r}^{\frac{3}{2}} B_1(-\lambda) \left[\cos\frac{5\theta}{2} + \hat{r}\cos\frac{7\theta}{2} \right] , \\ B_z &= 2cA^{\frac{1}{2}} = \left(\frac{8B_1}{h} A \right)^{\frac{1}{2}} \\ &= \left[8B_1^2 \left((1-\hat{r}^2) + \lambda\hat{r}^{\frac{5}{2}} \left(\cos\frac{5\theta}{2} + \frac{5\hat{r}}{7}\cos\frac{7\theta}{2} \right) \right) \right]^{\frac{1}{2}} . \end{aligned} \tag{3.19}$$

As before, the current within the current sheet is given by $[B_r]$ so that

$$[B_r](\hat{r}) = 5\hat{r}^{\frac{3}{2}} B_1(-\lambda)(1-\hat{r}) . \tag{3.20}$$

We observe that $-\lambda$ must be positive ($b_2 < 0$) for $[B_r]$ to be positive near $\hat{r}=0$. There will be a similar restriction to (3.16) on the value of λ which can be adjusted to give a physically realistic solution involving no X-type points, but we can still increase the mass of the current sheet by increasing B_1.

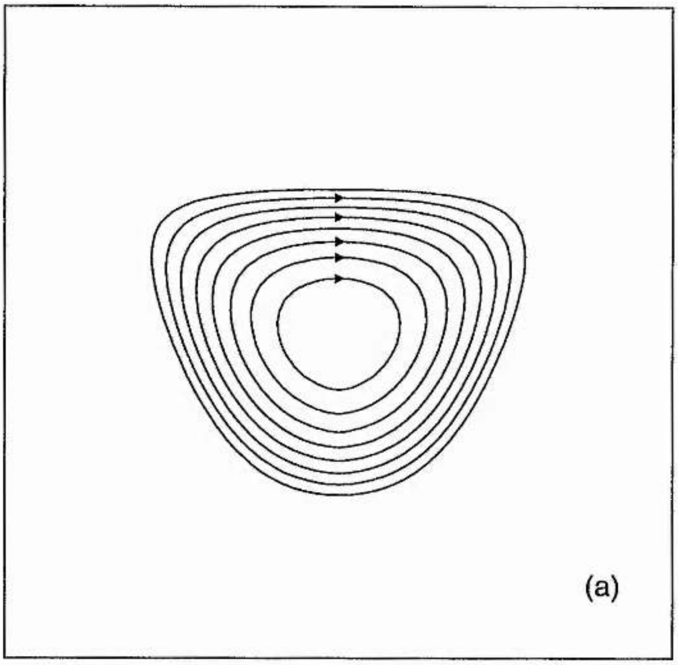

Figure 3.2: Magnetic field configurations in the (r, θ) plane of a twisted flux tube in which 2 terms in the series equation (3.10) have been taken, as in Equation (3.18). $B_1 = 4.0$ and (a) $-\lambda = 0.20$, (b) $-\lambda = 0.26$, (c) $-\lambda = 0.33$

The field lines projected onto the (r, θ) plane are shown in Figure 3.2a and the effect of varying λ is illustrated in Figures 3.2b and 3.2c, where Figure 3.2b corresponds to the critical value of λ (equation 3.21) and Figure 3.2c illustrates an unphysical solution.

We find that the solution will have no X-type points (and so the edge of the flux tube at $A = 0$ is closed) for values of λ such that

$$-\lambda < \frac{1}{3.86} = 0.259 \ . \tag{3.21}$$

The variation of the field components as a function of $\hat{r}$ at $\theta = \pi$ is shown in Figure 3.3a where we observe the current sheet behaviour as B_r reaches a maximum and then falls to zero at the edge of the tube ($\hat{r} = 1$). The variation of B_r as λ is changed is shown in Figure 3.3b where we observe that the magnitude of the current density in the current sheet drops as we decrease $-\lambda$. Figure 3.3c shows the mass density along the current sheet. As expected, the mass drops to zero at the ends of the current sheet.

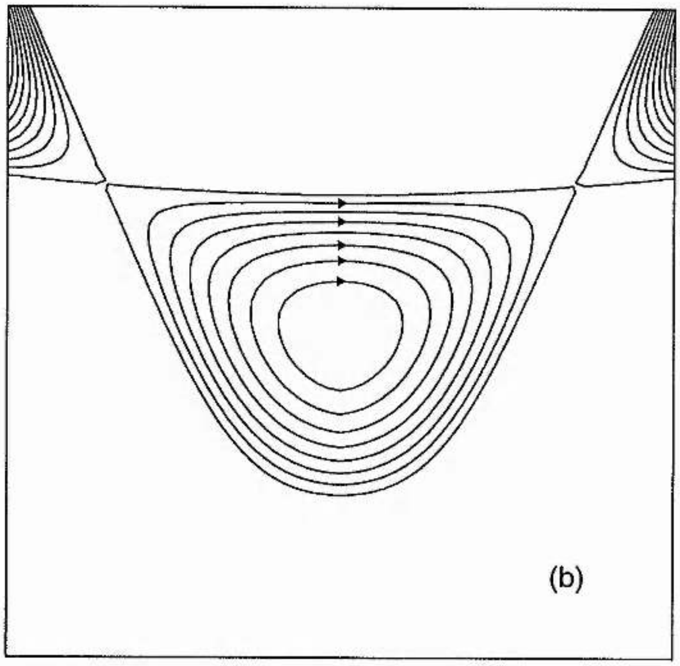

Figure 3.2b

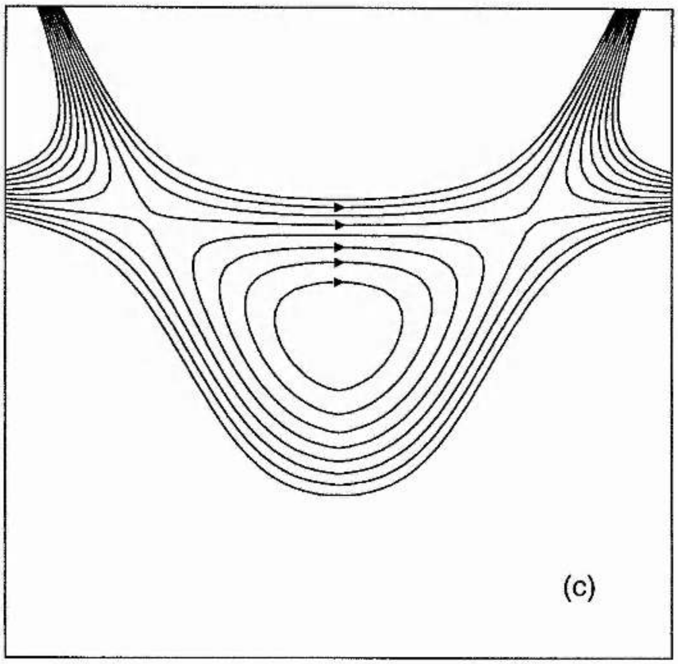

Figure 3.2c

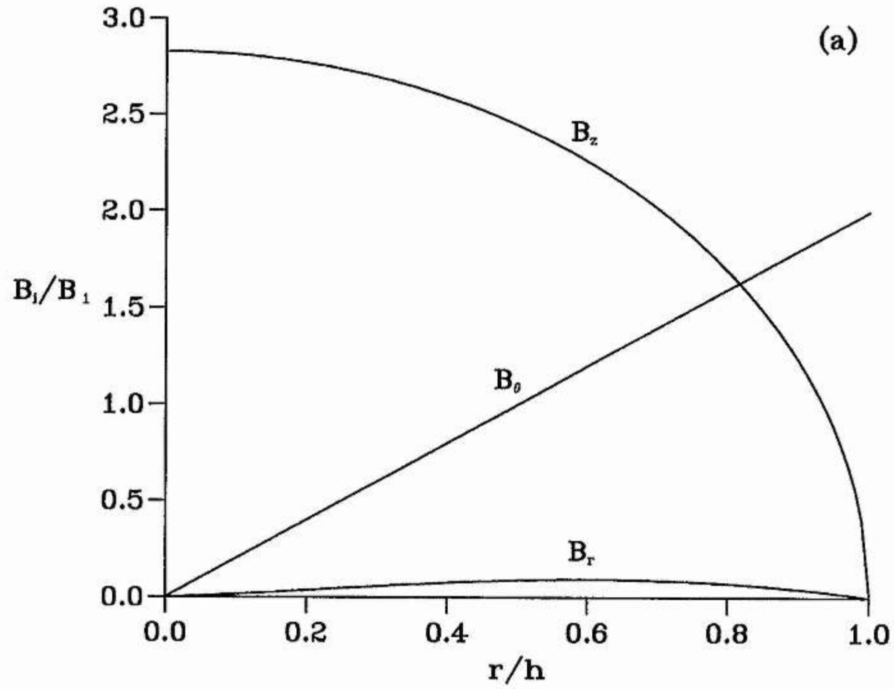

Figure 3.3: (a) The variation of the magnetic field components, given by Equation (3.19), along the prominence sheet for $-\lambda = 0.2$. (b) The variation of the radial field component, given by equation (3.19), along the current sheet for various values of λ. (c) The variation of mass density, given by equation (3.13), along the sheet for $-\lambda = 0.2$.

The total prominence mass (per unit length in the z direction) is

$$M = \int_0^1 m_A(\hat{r})h \, d\hat{r} = \frac{40B_1^2 h(-\lambda)}{63\mu g} \; . \tag{3.22}$$

Thus, the prominence mass falls as $-\lambda$ is decreased from its critical value given by (3.21). If we take $\lambda = -\frac{1}{20}$ and let $B_\theta(\frac{1}{2}, \pi) = 50 \times 10^{-4}T$ then with $h = 50 \times 10^6 m$ we find a value of

$$M = 1.2 \times 10^5 \; kg \; m^{-1} \; .$$

This is of the observed order of magnitude.

From (3.19), $[B_r]$ and $B_\theta(\theta = \pi)$ increase with B_1. Hence the Lorentz force is increased and this must be balanced by a corresponding increase in the prominence mass. From (3.22) we see that M is increased with B_1 and so this condition is indeed satisfied.

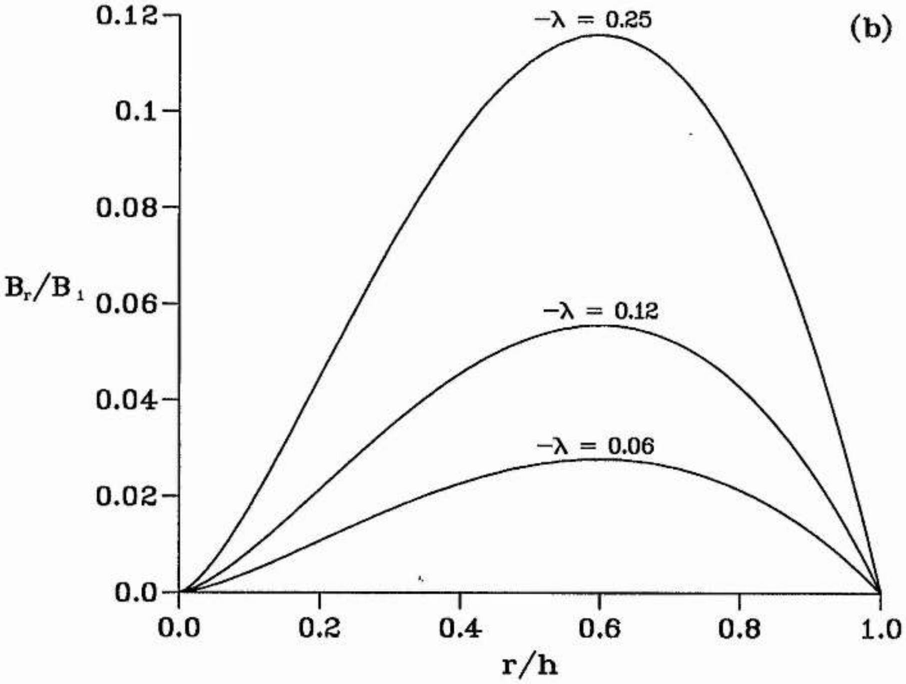

Figure 3.3b

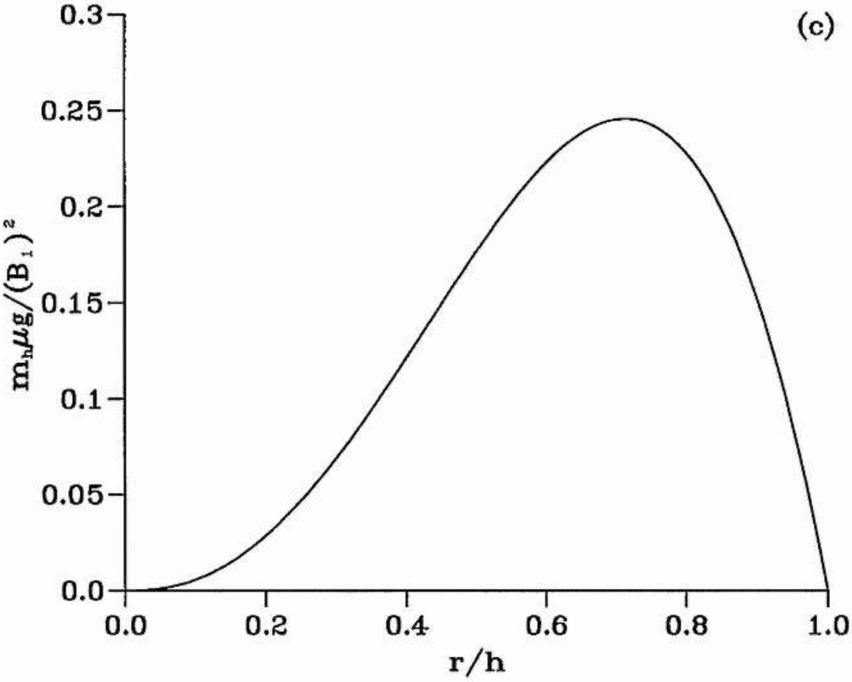

Figure 3.3c

Alternative choices for the constants k in (3.7) will give a similar expression for the mass but with an extra constant term. For example, if we take

$$k = n + \frac{p}{q} , \qquad p < q ,$$

then the modified mass density equation becomes

$$m_A \mu g = 2B_1(-\lambda)\hat{r}^{(1+p/q)} \left(2 + \frac{p}{q}\right) [1 - \hat{r}] \sin \left(2 + \frac{p}{q}\right)\pi \times$$
$$\left[2B_1\hat{r} + B_1(-\lambda)\hat{r}^{(1+p/q)} \left(2 + \frac{p}{q}\right) \left(\cos \left(2 + \frac{p}{q}\right)\pi - \hat{r} \sin \left(2 + \frac{p}{q}\right) \pi \ \cot \left(3 + \frac{p}{q}\right) \pi\right)\right] .$$

3.3.4 Three Terms in the Series in (3.10)

Taking three terms in the series allows even more flexibility. For example it is possible to have not only $[B_r] = 0$ but also $d[B_r]/dr = 0$ at the edge of the current sheet.

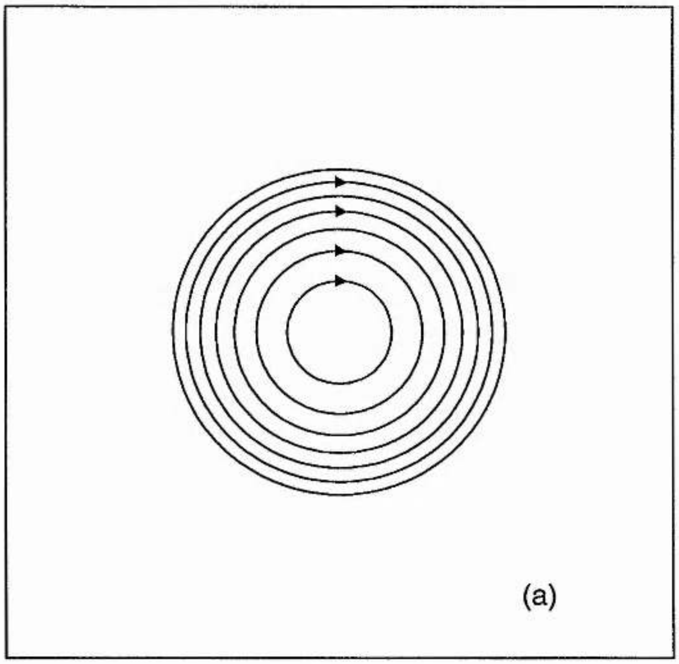

Figure 3.4: Magnetic field configurations in the (r, θ) plane of a flux tube in which 3 terms in the series solution have been taken, as in equation (3.23). $B_1 = 8.0$ and (a) $-\lambda = 0.001$, (b) $-\lambda = 0.065$, (c) $-\lambda = 0.2$

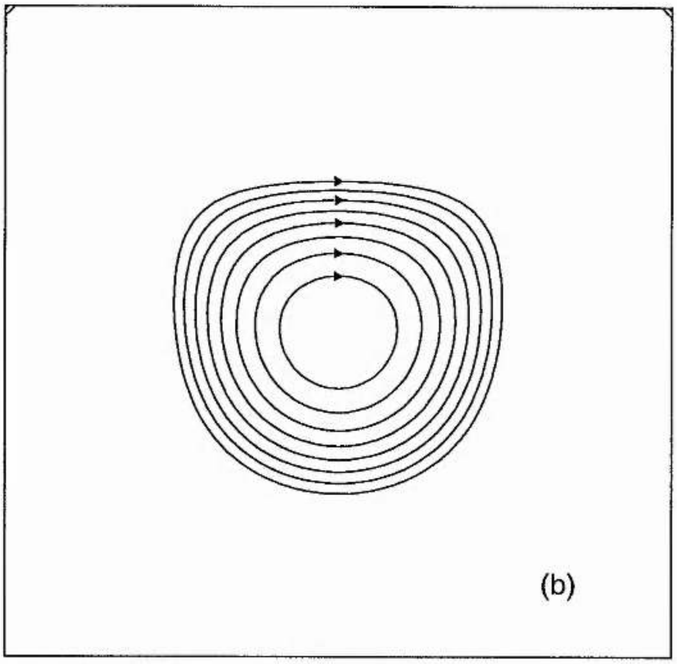

Figure 3.4b

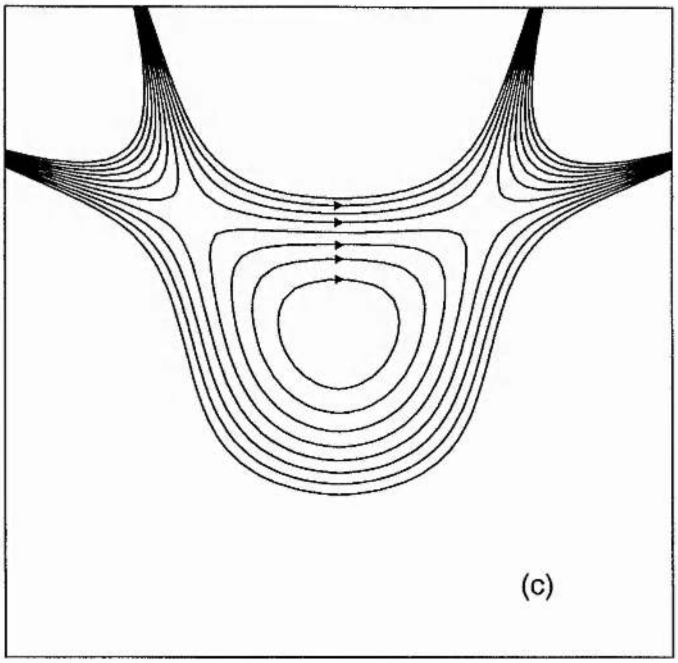

Figure 3.4c

However, other possibilities also exist. For example, the shape of the edge of the flux tube can be made more circular in order to simplify the matching onto an external potential field.

For illustration the first suggestion is considered and

$$A = B_1 h \left[(1 - \hat{r}^2) + \lambda \hat{r}^{\frac{5}{2}} \left(\cos\frac{5\theta}{2} + \frac{10}{7}\hat{r}\cos\frac{7\theta}{2} + \frac{5}{9}\hat{r}^2\cos\frac{9\theta}{2} \right) \right] . \tag{3.23}$$

Thus, across the prominence

$$[B_r](\hat{r}) = 5\hat{r}^{\frac{3}{2}} B_1 (-\lambda)(1 - \hat{r})^2 , \tag{3.24}$$

and the total prominence mass is now reduced by approximately a factor of 3. The projected field lines are shown in Figure 3.4 for various values of λ. Observe the near-circular topology for the low value of $-\lambda$. The critical value of λ for a physically realistic field is now approximately

$$-\lambda < \frac{1}{8} = 0.125 .$$

Figure 3.4c illustrates the topology of an unphysical solution.

Thus, as the number of terms in the series is increased the critical value of $-\lambda$ decreases.

Figure 3.5a shows the variation of B_r along the current sheet and clearly demonstrates the way in which B_r drops to zero smoothly. The mass distribution is shown in Figure 3.5b. Obviously more and more terms could be considered but instead a simple description of the internal structure of the prominence is now considered.

3.4 Internal Prominence Structure

To obtain information about the internal structure the prominence is assumed to be of finite thickness lying between

$$\pi - \delta \leq \theta \leq \pi + \delta, \quad \delta << 1 .$$

The external solution is given by the two-term solution (3.17) and the hydrostatic background atmosphere:

$$p = p_o e^{-\hat{r}h\cos\theta/H}, \quad \rho = \rho_o e^{-\hat{r}h\cos\theta/H} .$$

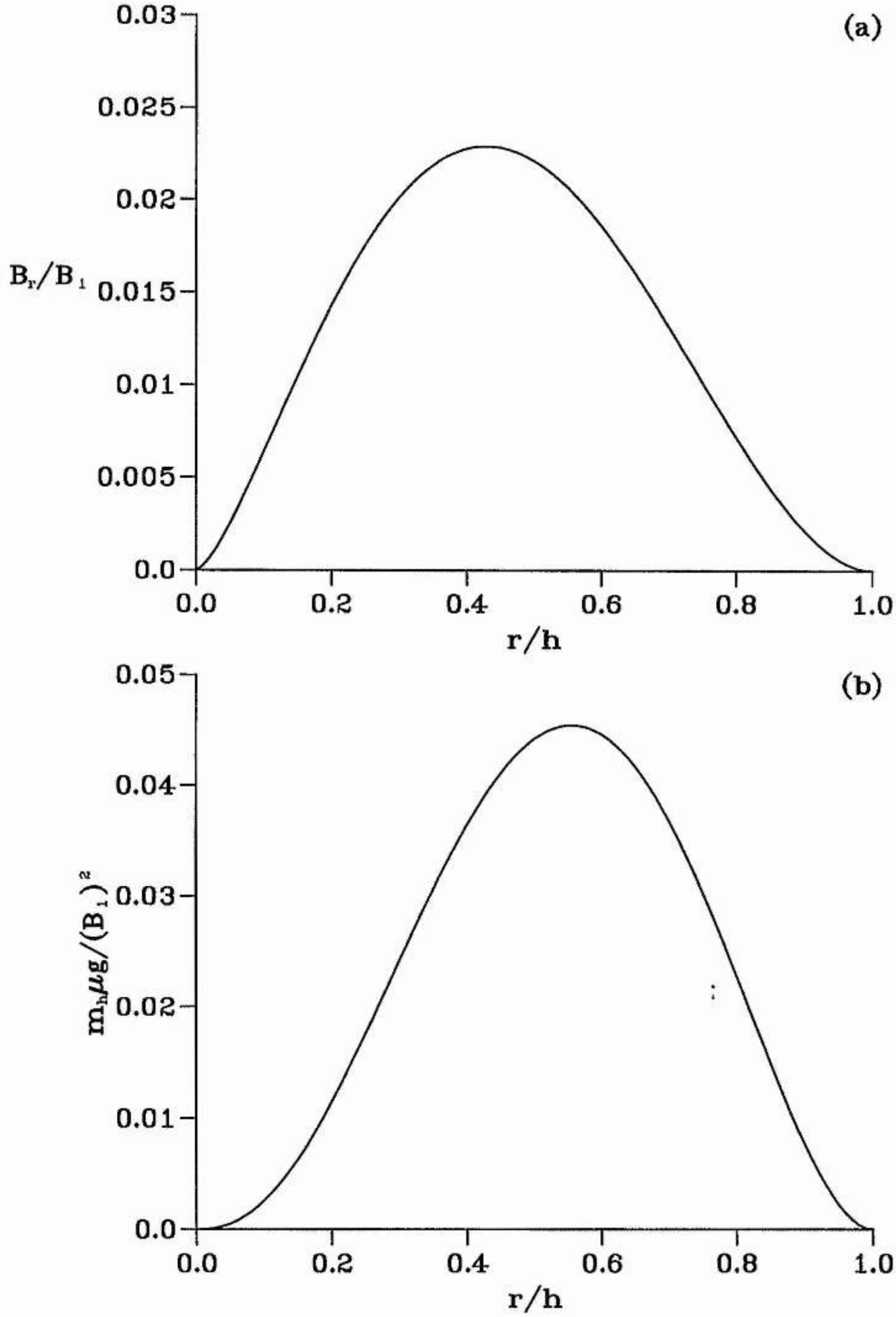

Figure 3.5: (a) The variation of B_r along the current sheet for 3 terms in the series, with $-\lambda = 0.1$. (b) The variation of mass density along the current sheet for 3 terms in the series, with $-\lambda = 0.1$.

At the prominence edge $(\theta = \pi - \delta)$,

$$\begin{aligned} A &= B_1 h \left[(1-\hat{r}^2) - \frac{5(-\lambda)}{2} \delta \hat{r}^{\frac{5}{2}} (1-\hat{r}) \right] + 0(\delta^3) \ , \\ B_r &= \frac{5(-\lambda)}{2} B_1 \hat{r}^{\frac{3}{2}} (1-\hat{r}) + 0(\delta^2) \ , \\ B_\theta &= 2B_1\hat{r} + \frac{5B_1(-\lambda)}{4} \delta \hat{r}^{\frac{3}{2}} (5-7\hat{r}) + 0(\delta^3) \ . \end{aligned} \tag{3.25}$$

This solution, for $\delta << 1$, will be matched onto the internal solution. Since B_r must change rapidly from the value given by (3.25) at $\theta = \pi - \delta$ to zero at $\theta = \pi$, for symmetric solutions, it is useful to define an expanded scale with

$$\phi = \frac{\pi - \theta}{\delta} \ . \tag{3.26}$$

The prominence now lies between $-1 \leq \phi \leq 1$. Taking the same expression for $B_z(A)$, the force balance equation in cylindrical coordinates is

$$\frac{\partial p}{\partial r} + \rho g \cos\theta = -\frac{1}{\mu} \frac{\partial A}{\partial r} \left[\nabla^2 A + 2c^2 \right] \ , \tag{3.27}$$

$$\frac{1}{r} \frac{\partial p}{\partial \theta} - \rho g \sin\theta = -\frac{1}{\mu r} \frac{\partial A}{\partial \theta} \left[\nabla^2 A + 2c^2 \right] \ . \tag{3.28}$$

Expressing (3.27) and (3.28) in terms of $\hat{r}$ and ϕ and expanding $\cos\theta$ and $\sin\theta$ in powers of δ gives

$$\frac{1}{h} \frac{\partial p}{\partial \hat{r}} - \rho g = -\frac{1}{\mu h} \frac{\partial A}{\partial \hat{r}} \left[\frac{1}{\hat{r} h^2} \frac{\partial}{\partial \hat{r}} \left(\hat{r} \frac{\partial A}{\partial \hat{r}} \right) + \frac{1}{\hat{r}^2 h^2 \delta^2} \frac{\partial^2 A}{\partial \phi^2} + 2c^2 \right] \ , \tag{3.29}$$

$$-\frac{1}{h\delta\hat{r}} \frac{\partial p}{\partial \phi} = \frac{1}{\mu h \delta \hat{r}} \frac{\partial A}{\partial \phi} \left[\frac{1}{\hat{r} h^2} \frac{\partial}{\partial \hat{r}} \left(\hat{r} \frac{\partial A}{\partial \hat{r}} \right) + \frac{1}{\hat{r}^2 h^2 \delta^2} \frac{\partial^2 A}{\partial \phi^2} + 2c^2 \right] \ . \tag{3.30}$$

In order to match to the external solution, given by (3.25) at $\phi = 1$, it is necessary that

$$\frac{\partial A}{\partial \hat{r}} = 0(1) \quad \text{and} \quad \frac{\partial A}{\partial \phi} = 0(\delta) \ .$$

This can be achieved if

$$A = B_1 h (1 - \hat{r}^2) + \delta A_1(\hat{r}, \phi) + 0(\delta^3) \ .$$

Then the leading order behaviour of (3.30) gives

$$p(\hat{r},\phi) = p_1(\hat{r}) - \frac{1}{2\mu}\left[\frac{1}{\hat{r}h}\left(\frac{\partial A_1}{\partial \phi}\right)\right]^2 . \tag{3.31}$$

Matching the pressure to the external solution, expanded about $\theta = \pi - \delta$, gives

$$p_1(\hat{r}) = \frac{B_1^2}{2\mu}\left[\beta e^{\hat{r}h/H} + \frac{25}{4}(-\lambda)^2\hat{r}^3(1-\hat{r})^2\right] , \tag{3.32}$$

where $\beta = 2\mu p_0/B_1^2$ is the plasma beta associated with the cylindrically symmetric component of the field.

Using (3.31) in (3.29) gives the leading order behaviour of the density as

$$\rho(\hat{r},\phi)g = \frac{-2B_1}{\mu\hat{r}h^2\delta}\frac{\partial^2 A_1}{\partial\phi^2} + \frac{1}{h}\frac{\partial p}{\partial \hat{r}} . \tag{3.33}$$

Thus, for a positive density $\partial^2 A_1/\partial\phi^2$ must be negative.

It is possible to have a jump in density at the edge of the prominence but if $\partial^2 A_1/\partial\phi^2 = 0$ at $\phi = 1$ then the order unity pressure gradient term must also be included.

Since the pressure and magnetic field components match to the external solution, to leading order, one way to proceed is to specify $A_1(\hat{r},\phi)$ and deduce the pressure from (3.31), the density from (3.33) and the temperature from the gas law

$$p = \rho RT . \tag{3.34}$$

In reality the temperature is determined from an appropriate energy equation and restricts the choice of A_1 and hence the equilibrium. The energetics are not, however, considered here but A_1 is selected such that suitable realistic density and temperature profiles are achieved.

Obviously, the solutions must be checked to see if they are physically relevant. For example, we choose

$$A_1(\hat{r},\phi) = -\frac{5B_1h}{2}(-\lambda)\hat{r}^{\frac{5}{2}}(1-\hat{r})F(\phi) , \tag{3.35}$$

where $F(\phi)$ is an arbitrary function that must satisfy

$$\begin{aligned} F(1) = 1,\ (F(-1) = 1) &\ :\ \textit{matching to } (3.25) , \\ F'(1) = 1,\ (F'(-1) = -1) &\ :\ B_r \textit{ is continuous at edge} , \\ F'(0) = 0 &\ :\ B_r \textit{ is zero at centre} , \\ F''(\phi) \geq 0 &\ :\ \textit{from } (3.33) . \end{aligned} \tag{3.36}$$

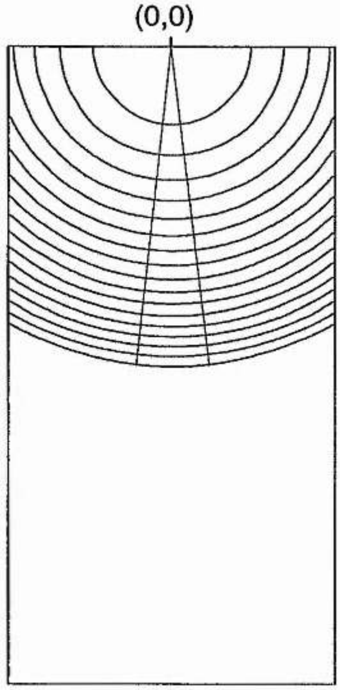

Figure 3.6: The magnetic field lines across the prominence with the expanded scale defined by (3.26) and the internal field given by $F(\phi)$ in (3.37).

We now present the results for some different functions, $F(\phi)$.

Case i)

A simple function, satisfying these constraints is

$$F(\phi) = 1 - \frac{2}{\pi}\ \cos\ \frac{\pi\phi}{2}\ . \tag{3.37}$$

Thus

$$A_1(\hat{r},\phi) = -\frac{5}{2}B_1 h(-\lambda)\hat{r}^{\frac{5}{2}}(1-\hat{r})\left(1 - \frac{2}{\pi}\ \cos\ \frac{\pi\phi}{2}\right)\ .$$

The field lines are shown in Figure 3.6 for the expanded scale.

Using (3.32), (3.31) becomes

$$p(\hat{r},\phi) = \frac{B_1^2}{2\mu}\left[\beta e^{\hat{r}h/H} + \frac{25}{4}(-\lambda)^2\hat{r}^3(1-\hat{r})^2\ \cos^2\ \frac{\pi\phi}{2}\right]\ . \tag{3.38}$$

Since $\frac{\partial^2 A_1}{\partial\phi^2}$ is zero at $\phi = 1$, the 0(1) terms in (3.33) must be considered and so

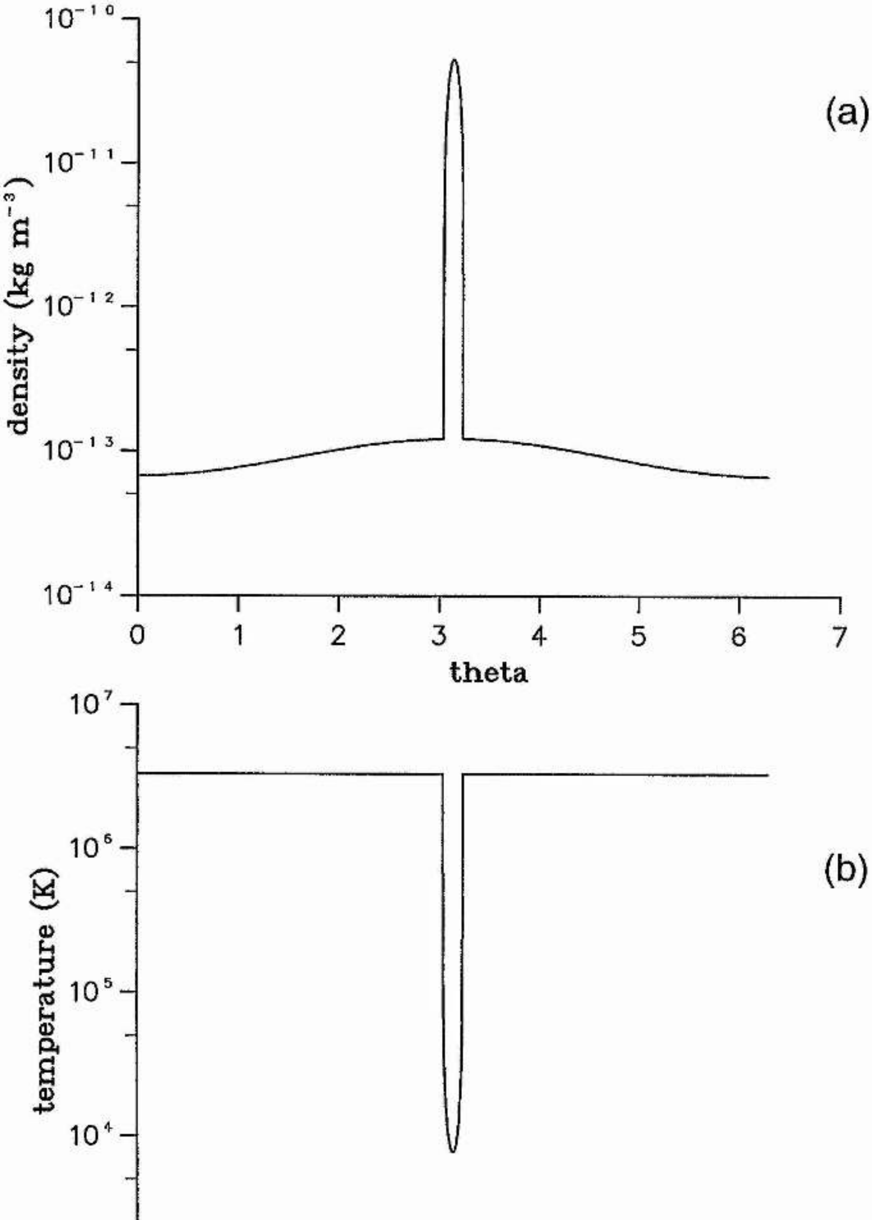

Figure 3.7: The variation with θ for the matched internal and external solutions for a) density b) temperature with $\delta = 0.1$, $-\lambda = 0.01$ and $\tilde{r} = 0.6$. c) Solutions for the internal prominence temperature as λ is varied with $\delta = 0.1$ and $\tilde{r} = 0.6$.

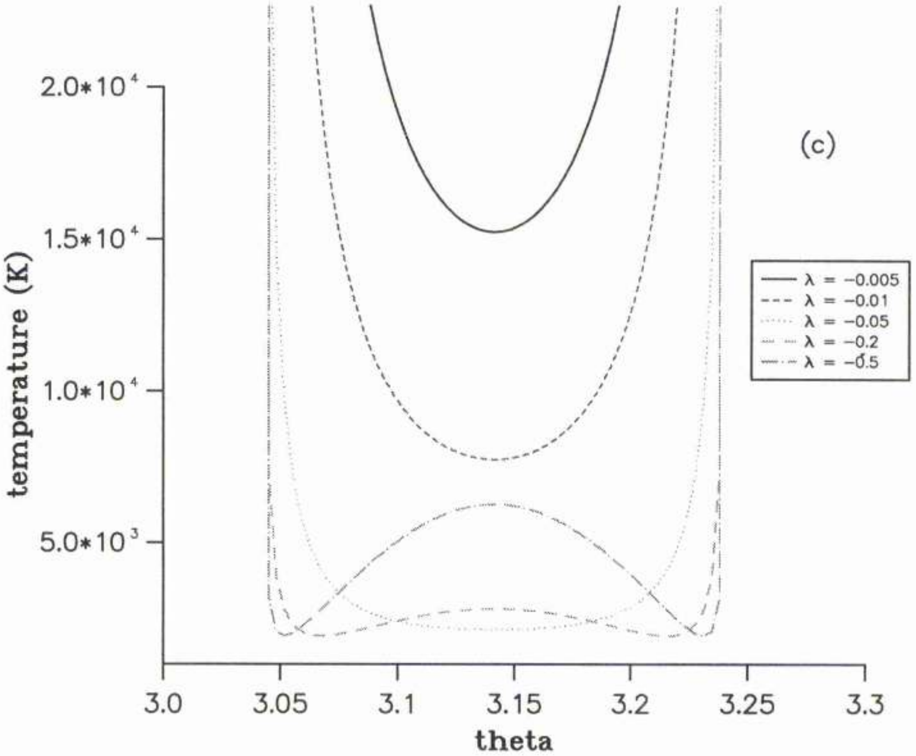

Figure 3.7c

$$\rho(\hat{r},\phi)g = \frac{B_1^2}{2\mu}\left[\frac{\beta e^{\hat{r}h/H}}{H} + \frac{5\pi}{\delta h}(-\lambda)\hat{r}^{\frac{3}{2}}(1-\hat{r})\ \cos\ \frac{\pi\phi}{2}\right] . \tag{3.39}$$

Also

$$T(\hat{r},\phi) = \frac{P(\hat{r},\phi)}{R\rho(\hat{r},\phi)} .$$

We observe that the external, coronal temperature is given by

$$T(\hat{r},1) = \frac{gH}{R} \approx 3\times 10^6 K .$$

The variations of density and temperature, at constant radius, for the matched internal and external solution are illustrated in Figures 3.7a and 3.7b respectively.

If we assume a temperature profile that increases monotonically from a minimum value at the centre of the prominence ($\phi = 0$) to the value given by the external solution (gH/R) at the edge ($\phi = \pm 1$) then there is an additional restriction on the value of λ given by

$$-\lambda \le 0.05\ .$$

The variation of temperature with ϕ for different values of λ is shown in Figure 3.7c.

This restriction on λ is quite severe. It means that the field is inclined to the horizontal by an angle of less than three degrees. However, relaxing the monotonic assumption of the temperature allows us to retrieve the earlier restriction (3.21). In addition, modifying the internal magnetic field structure will modify the temperature and the addition of a realistic energy balance equation will also influence the temperature. Thus, this restriction should not be considered too seriously.

Contours of density, on the expanded scale are shown in Figure 3.8a. Note that the wedge shape only applies to the low-density contours and for high-density values the contours are almost elliptical. Figure 3.8b shows a surface plot of the density in which the wedge is clearly seen.

Case ii)

$$F(\phi) = \frac{1}{2}(1+\phi^2)\ . \tag{3.40}$$

Now

$$A_1(\hat{r},\phi) = -\frac{5}{2}B_1 h(-\lambda)\hat{r}^{\frac{5}{2}}(1-\hat{r})\frac{1}{2}(1+\phi^2)\ ,$$

and

$$p(\hat{r},\phi) = \frac{B_1^2}{2\mu}\left[\beta e^{\hat{r}h/H} + \frac{25}{4}(-\lambda)^2\hat{r}^3(1-\hat{r})^2(1-\phi^2)\right]\ . \tag{3.41}$$

In this case we see that $\frac{\partial^2 A_1}{\partial\phi^2} \ne 0$ at $\phi = 1$ so the order unity terms in the expression for $\rho(\hat{r},\phi)$ may be neglected:

$$\rho(\hat{r},\phi)g = \frac{B_1^2}{2\mu}\left[\frac{10(-\lambda)}{h\delta}\hat{r}^{\frac{3}{2}}(1-\hat{r})\right]\ . \tag{3.42}$$

It can be seen from (3.41) that the internal pressure increases from the external value at $\phi = \pm 1$ to a maximum at the centre ($\phi = 0$). However, (3.42) indicates that the density is independent of ϕ and so it can be deduced from (3.34) that, although the temperature drops rapidly, as before, at the edge ($\phi = \pm 1$) from the external coronal value, there is a slight increase to a local maximum at the centre ($\phi = 0$).

On this basis it seems that the more physically realistic function is that given in case i).

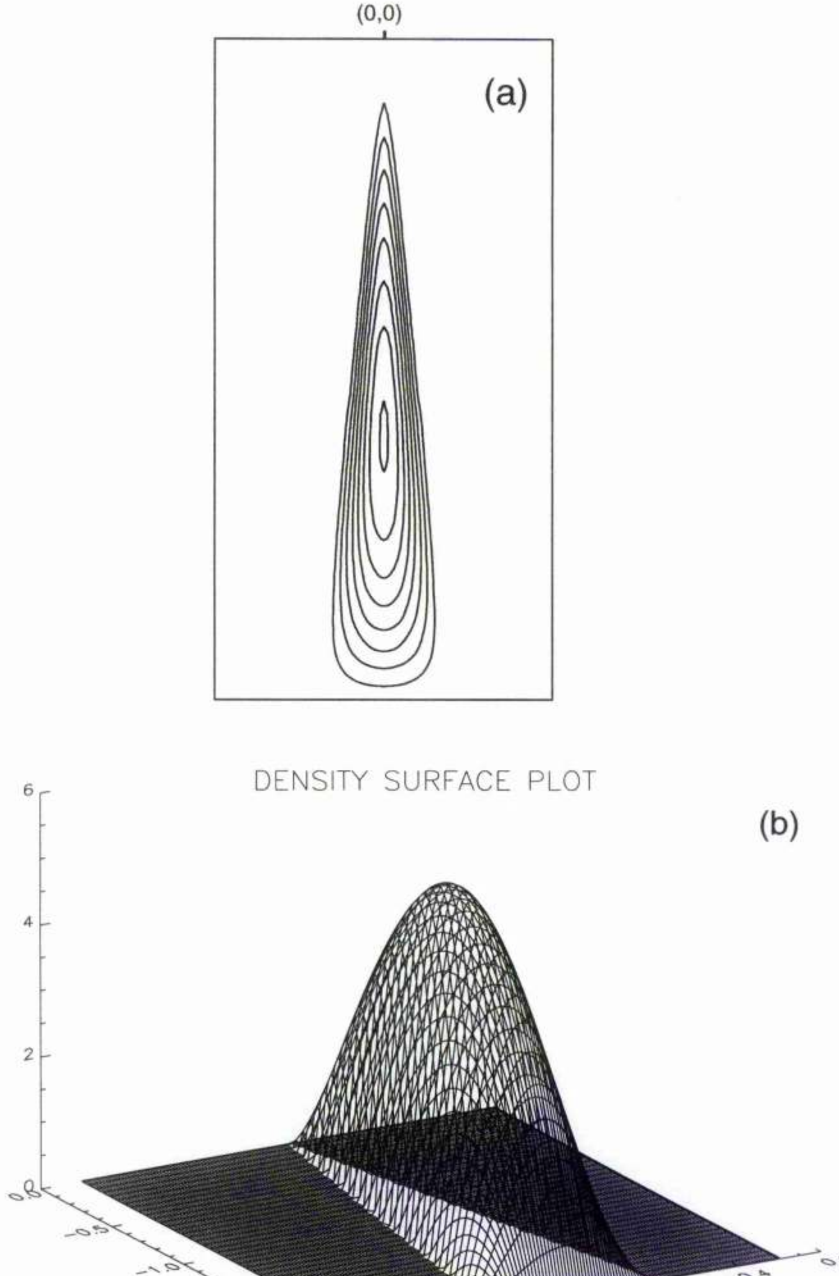

Figure 3.8: a) Contour plot of the density using the expanded scale defined by (3.37). b) Surface plot of the density highlighting the wedge shape.

3.5 Discussion

Following the work of Ridgway, Priest and Amari (1991), the external force-free solution for a current sheet with constant axial current density has been modified to model a *finite height* current sheet. By considering two terms in the series solution in (3.10), the jump in the radial field component, $[B_r]$, along the current sheet can be made to vanish at both the axis and at the *lower edge of the flux tube* thus enabling the flux tube to be matched onto a background potential coronal field. If additionally, a third term in the series is included it is possible for the current to drop to zero in a *smooth* manner and also for the outer edge of the flux tube to be made more *circular*, both of which facilitate an easier match onto the background field.

From Figure 3.3a we observe that the value of B_z/B_θ (ie. the shear of the field through the prominence) goes from ∞ to 0 as $\hat{r}$ increases from 0 to 1 so the top of the sheet is infinitely sheared whereas the base has zero shear. This is not observed in prominences but the model could be rectified by scaling r so that the sheet lies somewhere between the origin and the edge of the flux tube.

We have also observed that there is a critical value of $-\lambda$, a dimensionless parameter proportional to the current in the current sheet, above which the outermost field line of the tube ($A = 0$) ceases to be a simple closed contour but opens out to include an unphysical field topology with two *X-type* neutral points. Thus, there is a limit on the size, in terms of the mass and current, of the current sheet. However, this can be compensated to some extent by increasing the axial magnetic field. The critical value of $-\lambda$ is also affected by the additional requirements we impose on the magnetic field as the number of terms in the series is increased.

In Section 3 the prominence sheet is expanded to a narrow but finite width, of angle 2δ, to allow an analysis of the internal structure of the prominence. Two appropriate forms of the internal magnetic field have been selected that match smoothly onto the external force-free field at the edge of the prominence. This allows the internal pressure and density to be evaluated, to leading order, from the force balance equation (3.27) and (3.28) and hence the temperature from the gas law (3.34).

Using the first of these internal solutions we have successfully modelled a prominence that has an enhanced density and reduced temperature in comparison with the external coronal environment. There is a further restriction, however, on the value of $-\lambda$ if the temperature profile is assumed to increase *monotonically* from the centre of the prominence to the edge.

Following this method, different forms of the internal field could be tried in an attempt to adjust the internal structure of a prominence, for example modelling inhomogeneities in the density. Also, it is possible to consider variations in the prominence width with height, rather than taking a wedge shape of constant angle.

Chapter 4

Polar-Crown Prominence Model

4.1 Chapter Summary

In this chapter we present a 2-D potential field model for the magnetic field structure in the environment of a typical quiescent polar-crown prominence. The field is computed using the general method of Titov (1992) in which a curved current sheet, representing the prominence, is supported in equilibrium by upwardly directed Lorentz forces to balance the prominence weight. The mass density of the prominence sheet is computed in this solution using a simple force balance and observed values of the photospheric and prominence magnetic field. This calculation gives a mass density of the correct order of magnitude. The prominence sheet is surrounded by an inverse-polarity field configuration adjacent to a region of vertical, open polar field in agreement with observations.

A perturbation analysis provides a method for studying the evolution of the current sheet as the parameters of the system are varied together with an examination of the splitting of an X-type neutral point into a current sheet.

4.2 Introduction

Prominences that are observed at high latitudes ($> 45°$) are known as *polar prominences* and an array of such prominences, known as *polar-crown prominences*, is often seen to form a ring or crown around the pole as they overlie an East-West oriented polarity inversion line (PIL). This PIL separates the region of open flux, which constitutes the polar coronal hole, and adjacent large scale magnetic regions of lower latitude (McIntosh, 1980). In contrast to the general behaviour of sunspots and active regions which move towards the equator as the solar cycle progresses, the polar-crown PIL actually migrates towards the pole. It does so at an increasing rate so that the overlying prominences appear to "rush to the poles" (Waldmeier, 1957). Towards the end of the solar cycle, the polar-crown PIL reaches the pole and the prominences disappear as the polar polarity reverses and the new solar cycle begins. Occasionally, the migration of a second band of polar-crown prominences will occur, following the first band after an interval of two or three years (Waldmeier, 1973).

Leroy et al. (1983) describe many of the general properties from an observed sample of 120 polar-crown prominences. They find that an average field strength of 8 G is present in the sample, that the field is more or less constant except for a tendency to increase (at a rate of 0.5×10^{-4} G km^{-1}) with height, and that the average field shear angle is 25° to the prominence long axis. There is an average filling ratio of 0.1, i.e. only a tenth of the prominence's total width along the line of sight is comprised of dense material, being clumped in the form of fine threads. They also describe the variation of polar prominence properties with the solar cycle. For example, the maximum field strength at the cycle maximum is double that at the beginning of the cycle, and there is a reversal of the field direction along the inversion line at each new cycle. Finally, and very importantly, they find that the associated magnetic field of polar-crown prominences is of inverse-polarity.

In this chapter we suggest that polar-crown prominences form and are supported in field line dips which may occur between the open field of the pole and a neighbouring bipolar region. The resulting field topology naturally allows inverse-polarity prominence equilibria to exist, an example of which is computed in Section 4.4 using complex variable theory to generate an appropriate potential field.

Many authors have used complex variable theory with a current sheet to model a 2-D prominence supported in the magnetic field. The current sheet may be represented by a branch cut in the complex plane where a tangential discontinuity in the field appears

Anzer (1972); Malherbe and Priest (1983); Wu and Low (1987); Démoulin et al. (1989)). The interaction between the magnetic field and the current in the sheet produces a Lorentz force. In order to sustain the support, and hence the equilibrium of the sheet, this force must be directed vertically upwards at every point in the sheet (Anzer, 1989).

Due to the considered asymmetric distribution of photospheric flux, the resulting solutions will contain prominence sheets that are non-vertical and even *curved*. Previously, Wu and Low (1987) published a paper which demonstrates the support of curved current sheets in a potential field. However, they only found particular solutions for the case of two dipoles on the photosphere, in which the current sheet forms an arc of a circle. Aly and Amari (1988) presented a more general method which generates other equilibria by using a known solution and an appropriate conformal mapping but this method does not allow the imposition of the observed normal photospheric field component. That problem is resolved in this chapter as we adapt a technique, due to Titov (1992), that constructs general 2-D potential fields with curved current sheets from a given photospheric distribution. We utilise this technique to generate a suitable field configuration for the case of a curved polar-crown prominence supported in equilibrium between a region of uniform vertical field and a dipole field. The evolution of the prominence sheet, as the external parameters are varied, is studied in Section 4.5.2 together with an analysis of the splitting of an X-type neutral point into a current sheet of either *normal* or *inverse* sense (Section 4.5.3). These cases are both considered to produce prominence solutions in different configurations with an emphasis on the solutions that are of inverse-polarity type, the polar-crown prominences.

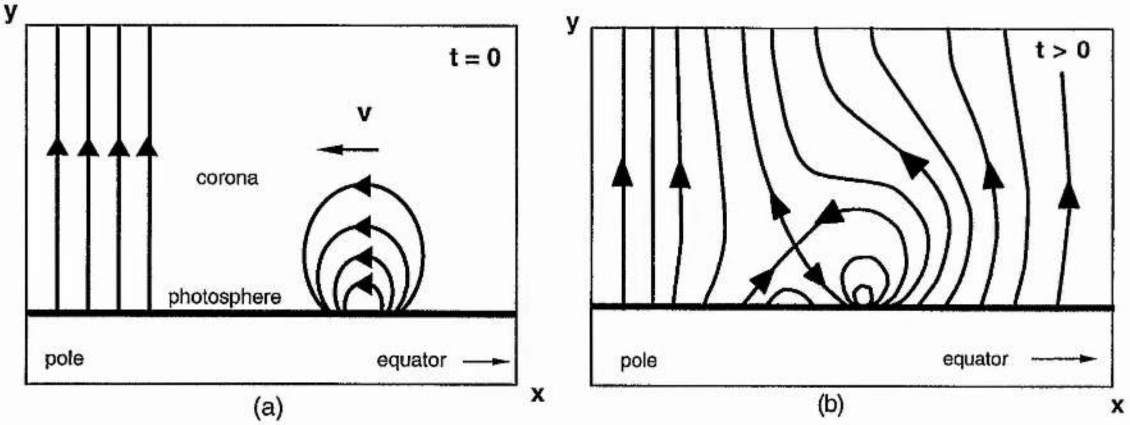

Figure 4.1: The field topology as the bipolar region pushes against and interacts with the polar field.

4.3 Description of the Model

We consider a region of uniform vertical magnetic field to represent the open polar field and investigate the interaction of a bipolar region as it pushes into this field (Figure 4.1a). Reconnection of the field lines will occur at the X-type neutral point that appears due to the oppositely directed contiguous fields (Figure 4.1b). Above the neutral point, a location of dipped magnetic field is formed and it is here that suitable conditions arise for cool, dense material to collect and form into the familiar quiescent prominences that are readily observed in the corona. This "pre-prominence" field configuration is discussed in more detail in Chapter 5 where we study the behaviour of the dips for various possible distributions of the photospheric flux.

It is the object of this chapter, however, to compute an appropriate *potential* field structure that contains a weighted current sheet (representing the prominence), supported in equilibrium at the location of these dips and so we use a very basic distribution of flux for simplicity.

4.4 Formulation of the Problem

4.4.1 Introductory Equations

The magnetohydrostatic force balance is given by

$$-\nabla p + \mathbf{j} \times \mathbf{B} + \rho \mathbf{g} = \mathbf{0} \tag{4.1}$$

with

$$\mathbf{j} = \frac{\nabla \times \mathbf{B}}{\mu} \quad \text{and} \quad \nabla \cdot \mathbf{B} = 0 \ . \tag{4.2}$$

In the coronal region, but outside the current sheet, the gas pressure is much less than the magnetic pressure ($\beta \ll 1$) and so we may neglect the pressure gradient term in (4.1). By considering length scales, l, that are significantly less than the pressure scale height ($l \ll H = 10^8$ m), (4.1) reduces to the force-free equation

$$\mathbf{j} \times \mathbf{B} = \mathbf{0} \ . \tag{4.3}$$

In particular, a potential field with $\mathbf{j} = \mathbf{0}$ may be used to represent crudely magnetic configurations supporting current sheet prominences.

Following from the analysis given in Chapter 2 we may write the field in terms of the complex variable, $w = x + i\ y$, so that

$$B(w) = B_y + i\ B_x \ . \tag{4.4}$$

Thus, the imaginary part of the magnetic field represents the horizontal field component, B_x, and the real part equates to B_y, the vertical field component. We now consider a simple example, without a current sheet, which may be used to represent approximately the pre-prominence polar magnetic field.

4.4.2 Purely Potential Case

We adopt a Cartesian system of coordinates where the (x, y) plane represents a section across the prominence, the long axis of the prominence lying in the $\hat{\mathbf{z}}$-direction. The photosphere may be taken to be the horizontal plane $y = y_{\text{ph}} > 0$ such that $y_{\text{ph}} \leq y_1$, where y_1 is the vertical coordinate of the lower end-point, w_1, of the prominence. In this way, a dipole at

$(y = 0)$ producing the bipolar flux is submerged below the surface. For simplicity, though, we refer to the plane $y = 0$ as being the photosphere.

To introduce a semblance of (current free) shear into the field, a constant third component, $B_z\,\hat{\mathbf{z}}$, is included in the configuration without invalidating the assumption that the whole field be potential $(\mathbf{j} = \mathbf{0})$. The field in the (x, y) plane may then be written in terms of the complex variable w $(= x + iy)$ as in equation (4.4).

By superimposing the two potential fields of (a) a dipole of strength m and position $(0, 0)$ and (b) a constant vertical field of magnitude B_{y0}, we obtain, in complex notation

$$B(w) = B(x + iy) = B_{y0} + \frac{im}{w^2} \qquad (y > 0)\ . \tag{4.5}$$

This field exhibits the general properties illustrated in Figure 4.1b.
As $w \to \infty$, $B(w) \to B_{y0}$, a constant vertical value, as required. The neutral point is located at w_N, given by

$$B_{y0} + \frac{im}{w_N^2} = 0\ . \tag{4.6}$$

One such field is shown in Figure 4.2a. Note that the values of B_{y0} and m have been set to unity in this and all subsequent figures. In each field line plot, constant intervals of the flux function, A, have been taken and the separatrix lines have been included as a dashed field line. Field lines close to the dipole have been omitted in all plots.

In Figure 4.2a, a small region of field line dips is apparent above the neutral point and a current sheet could assume a *curved* geometry in this vicinity. It must be noted that, although we form this sheet by changing the parameter values (e.g. increasing m) and partially or completely prohibiting reconnection at the neutral point, this is purely a mathematical trick for setting up a current sheet which then represents the prominence. In this model, prominence formation could occur in a dip in the field and would be controlled by the appropriate physical mechanism responsible for formation. It may be, for example, the traditional mechanism of thermal instability or the less traditional mechanism of lifting material from below the photospheric inversion line due to a spatial evolution of magnetic field on the photosphere (Titov et al., 1993). For the subsequent considerations it does not matter which mechanism forms the prominence, since only its final result, i.e. the magnetohydrostatic equilibrium configuration, will be the focus of this chapter.

4.4.3 Inclusion of the Current Sheet

To make progress we utilise the method of Titov (1992) to calculate general 2-D potential fields with neutral current sheets. The main result for an arbitrary photospheric component $B_y(x,0)$ is

$$B(w,\mathbf{r_e}) = -\frac{i}{\pi} Q_{\mathrm{hp}}(w,\mathbf{r_e}) \int_{-\infty}^{+\infty} \frac{B_y(\xi,0)\,d\xi}{(\xi - w) Q_{\mathrm{hp}}(\xi,\mathbf{r_e})} \,, \tag{4.7}$$

where $\mathbf{r_e} = (x_1, y_1, x_2, y_2)$ represents the endpoints (w_1, w_2) of the current sheet and

$$\begin{aligned} Q_{\mathrm{hp}}(w,\mathbf{r_e}) &= [(w - w_1)(w - w_2)(w - \bar{w}_1)(w - \bar{w}_2)]^{\frac{1}{2}} \\ &= \left[(w - x_1)^2 + y_1^2\right]^{\frac{1}{2}} \left[(w - x_2)^2 + y_2^2\right]^{\frac{1}{2}} , \end{aligned} \tag{4.8}$$

the overbars denoting complex conjugates. Q_{hp} determines branch cuts in the complex plane for the current sheet and its image sheet in $y < 0$.

The image sheet which extends from $\bar{w}_1$ to $\bar{w}_2$ ensures that the normal component $B_y(x,0)$ of the field on $y = 0$ (the photosphere) from the purely potential case (as in section 4.4.2) is preserved.

Consider a distribution of flux on $y = 0$ given by

$$B_y(x,0) = B_{y0} + m\pi\delta'(x) \,,$$

where δ is the Dirac-delta function and δ' is its derivative.

Writing $Q(x)$ to represent the x dependence of the function $Q_{\mathrm{hp}}(x,\mathbf{r_e})$ for convenience and substituting $B_y(x,0)$ into (4.7) we obtain

$$B(w,\mathbf{r_e}) = -\frac{i}{\pi} Q(w) \left\{ \int_{-\infty}^{+\infty} \frac{B_{y0}\,d\xi}{(\xi - w) Q(\xi)} - \frac{m\pi}{w^2 Q(0)} + \frac{m\pi Q'(0)}{w Q^2(0)} \right\} , \tag{4.9}$$

where the identity

$$\int_{-\infty}^{+\infty} f(\alpha)\, \delta'(p - \alpha)\, d\alpha \equiv f'(p) \,,$$

is used. It is possible to show that equation (4.9) reduces to the purely potential case as $w_1, w_2 \rightarrow w_N$ (Appendix A). All that remains is for the end-points, $\mathbf{r_e}$, of the current sheet

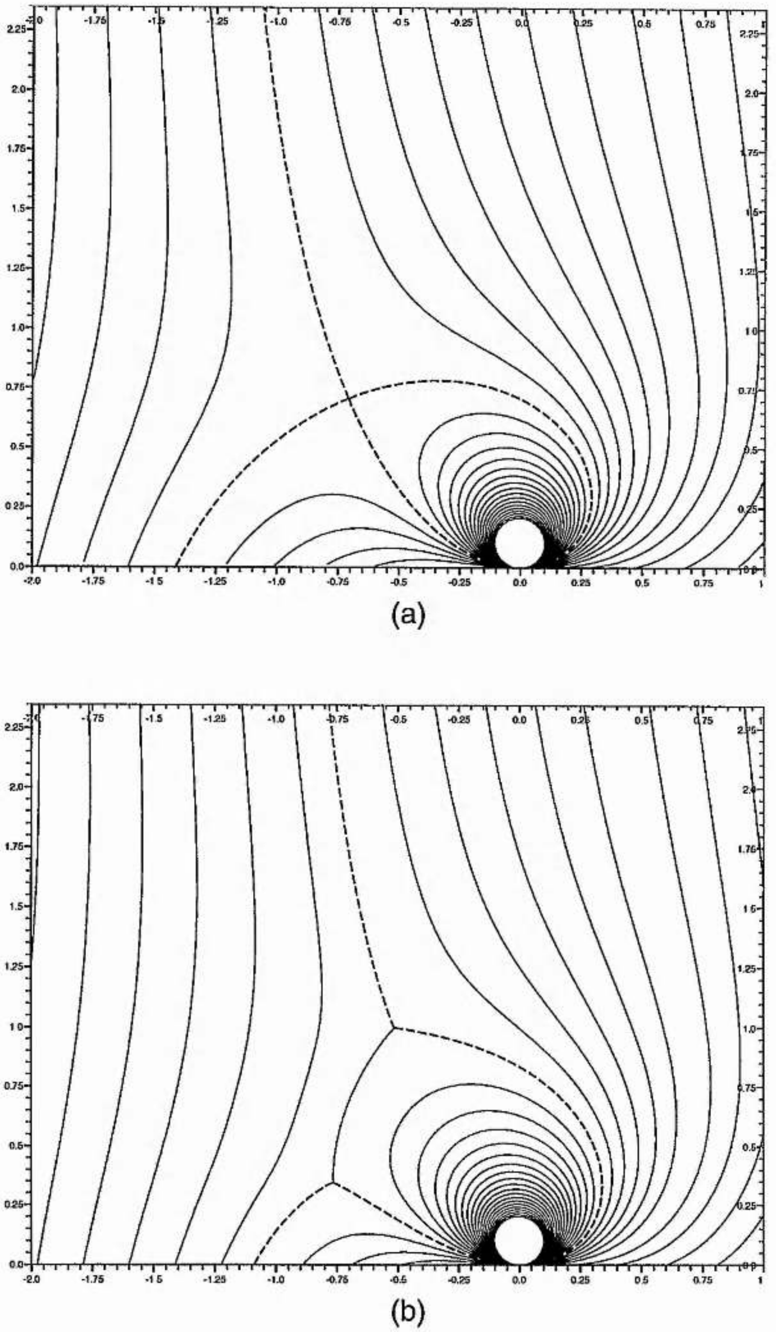

(a)

(b)

Figure 4.2: The field lines in the (x,y) plane for (a) the purely potential case with vertical field at infinity, and (b) the neutral sheet case with the same boundary conditions.

to be determined. There is one degree of freedom here, fixed by a physical mechanism of material accumulation in the prominence (which we do not consider here) so if we impose the vertical extent $(y_2 - y_1)$, say, of the current sheet, three conditions are needed to determine x_1, x_2 and y_1. These come from the asymptotic behaviour of the field as $w \to \infty$. Equation (4.9) then determines the field subject to these conditions.

Neutral Current Sheet

For a large value of w the unipolar source of field on the photosphere will behave as a point source of strength

$$\int_{-\infty}^{+\infty} B_{y0}\ dx\ .$$

In general, B_{y0} will be a function of x, as we model finite sources of photospheric flux and so this integral will be convergent. In this example, however, our infinite photospheric distribution leads to a divergence of the integral, but this may be easily resolved, although it requires a more extended analysis (see Appendix C).

The resulting magnetic field (4.9) can be considered as the superposition of the initial purely potential field and the field generated by the current sheet and its image. Physically, the contribution of the latter to the resultant field has only a dipolar asymptotic behaviour ($\sim 1/w^2$), so we require that our formal solution must behave, to order $1/w$, as

$$B(w, \mathbf{r_e}) \to 0w + 0w^0 + \frac{1}{\pi w} \int_{-\infty}^{+\infty} B_{y0}\ d\xi\ , \tag{4.10}$$

which gives the same asymptotic behaviour as the purely potential field (4.5). Comparing these coefficients of w with those of the general field (4.9) gives our three required conditions, derived in Appendix B. The solution of these three nonlinear and transcendental equations determines $\mathbf{r_e}$.

For the above boundary conditions (4.10), we obtain the field given in Figure 4.2b. The neutral sheet is clearly seen near the location of the previous neutral point and has a curved geometry as expected. The field becomes vertical at large distances, as required. There is a tangential discontinuity in the field across the sheet. This sheet, however, does not yet represent a prominence since the field is tangential to the sheet and so no supporting Lorentz force results.

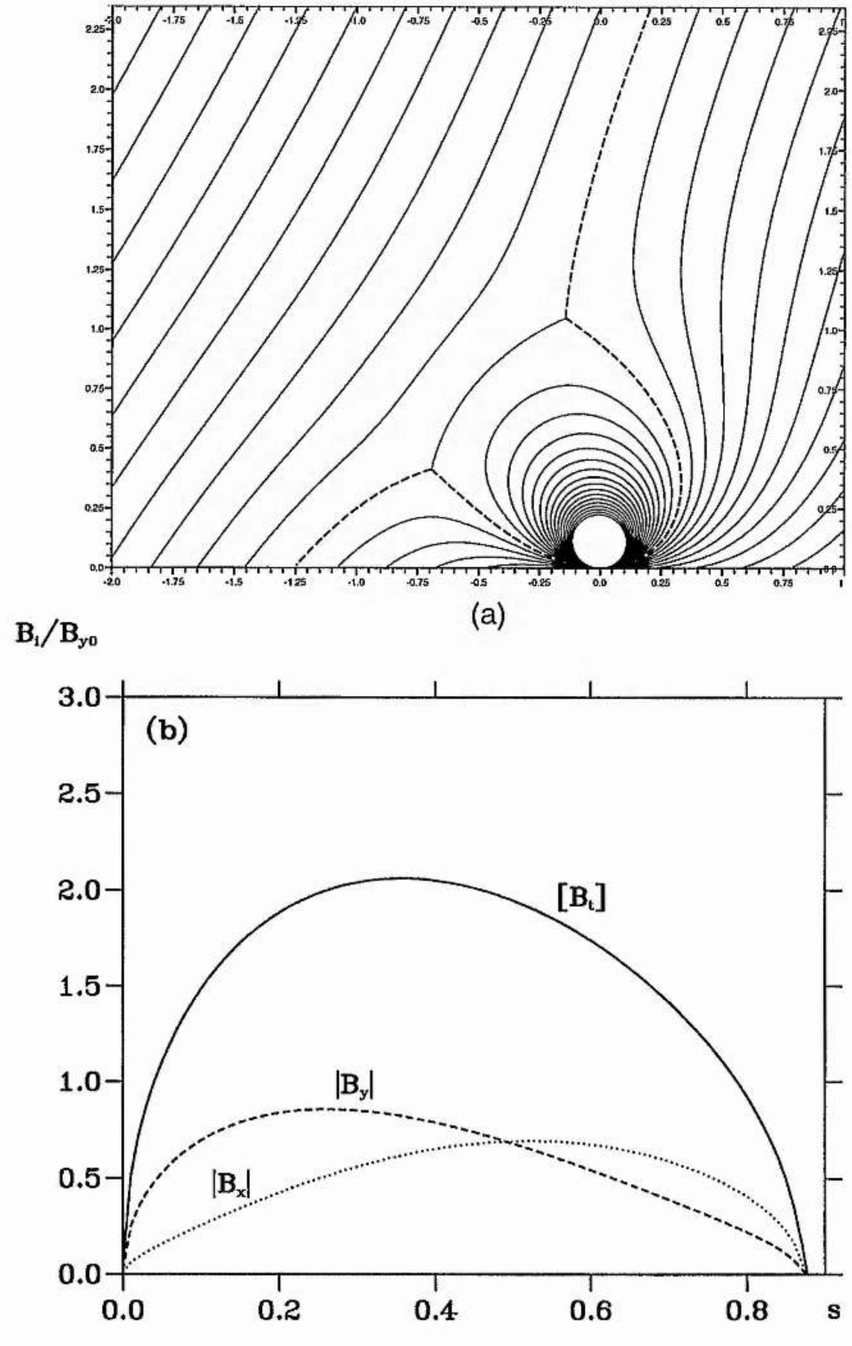

Figure 4.3: (a) The field lines for the boundary conditions given by (4.11) containing a neutral sheet (no mass). (b) The field components along the sheet showing also the jump in the tangential component, B_t, across the sheet.

Prominence Sheet

If the current sheet is to represent a prominence then it must be a sheet comprising dense material. The equilibrium of such a sheet is only possible if it is subject to a purely vertical force along its entire length to balance gravity. This force is magnetic and comes from the Lorentz force, $\mathbf{j} \times \mathbf{B}$. If this is to be directed upwards, the field which threads through the sheet must be purely horizontal since $\mathbf{j}$ is in the $\hat{\mathbf{z}}$-direction. The simplest way of providing this force is to superimpose a constant horizontal field $(-iB_{x0})$ on the configuration. However, if we take our asymptotic and photospheric conditions as before the result will be field lines that are slanted at infinity, i.e.

$$B(w) \sim B_{y0} - iB_{x0} \ ,$$

as $w \to \infty$. Thus, we must modify our conditions slightly, by changing the constant term in (4.10) so that

$$B(w, \mathbf{r}_{\mathrm{e}}) \to 0w + iB_{x0}\ w^0 + \frac{1}{\pi w}\int_{-\infty}^{+\infty} B_{y0}\ d\xi \ . \tag{4.11}$$

Again, the derivation of the equations that determine the end-points of the sheet is given in Appendix B. This results in a field, given by (4.9), containing a neutral current sheet with a slanted field at large distances as illustrated in Figure 4.3a. Figure 4.3b shows the field components along this neutral sheet from $w = w_1$ $(s = 0)$ to $w = w_2$ $(s = s^*)$. From now on, we take s to measure distance traversed along the sheet in a left-right direction.

Hence, our final field, vertical at a large distance and incorporating a prominence sheet is given by

$$B(w, \mathbf{r}_{\mathrm{e}}) = -\frac{i}{\pi}Q(w)\left\{\int_{-\infty}^{+\infty} \frac{B_{y0}\ d\xi}{(\xi - w)Q(\xi)} - \frac{m\pi}{w^2 Q(0)} + \frac{m\pi Q'(0)}{wQ^2(0)}\right\} - iB_{x0} \ . \tag{4.12}$$

This field is displayed in Figure 4.4a.

A new X-type neutral point appears just below the lower end of the prominence sheet which is of inverse-polarity type, i.e. the field through the prominence is in the reverse direction to the underlying photospheric field. The tangential discontinuity in B is now evident from the field lines that thread the prominence.

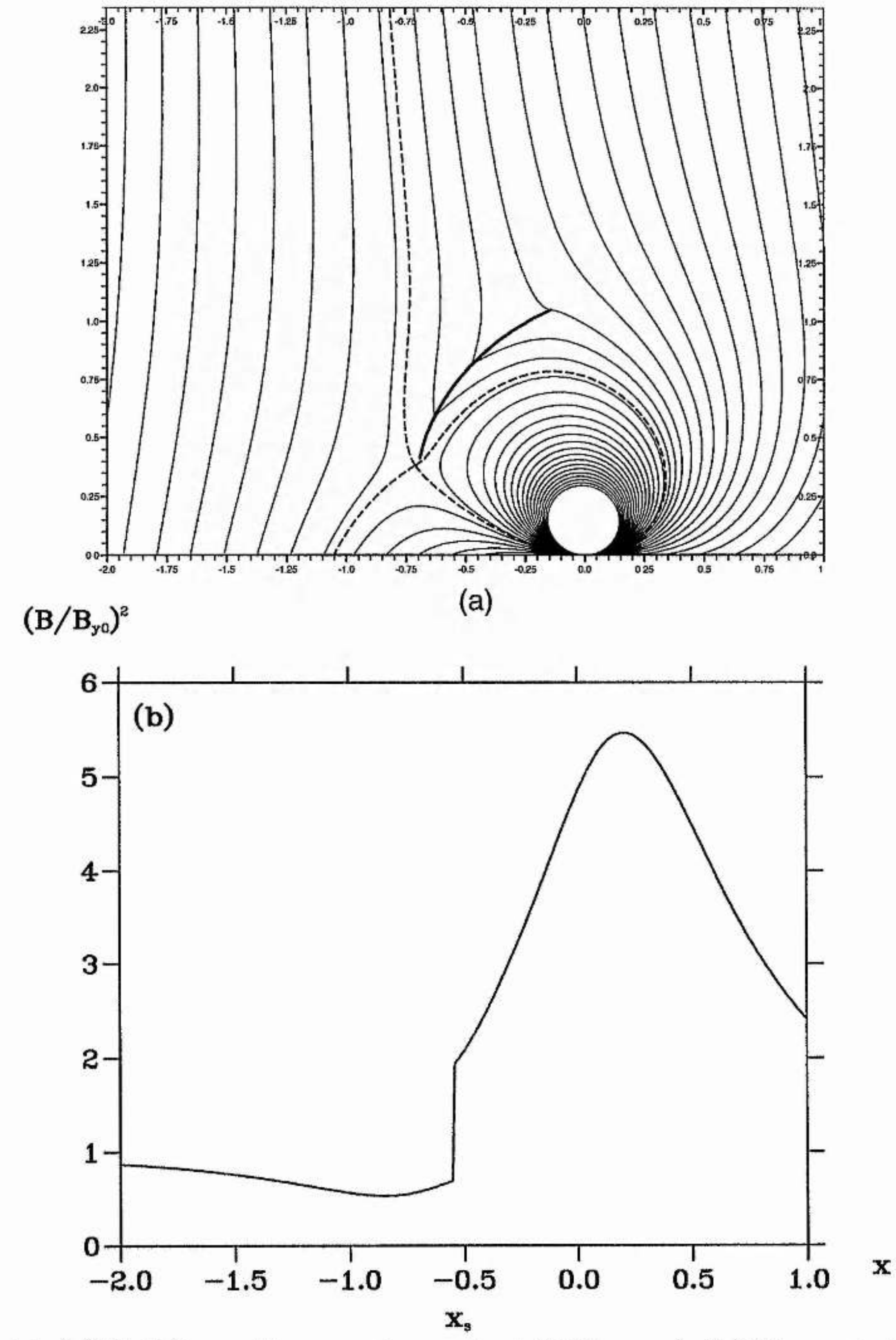

Figure 4.4: (a) Field lines with a prominence sheet (thick curve). (b) The magnetic pressure variation with x across the sheet at a constant height $y_s = (y_1 + y_2)/2$. x_s indicates the position of the sheet.

The Lorentz force may be written

$$\mathbf{j}\times\mathbf{B} = \frac{(\nabla\times\mathbf{B})}{\mu}\times\mathbf{B} = \frac{(\mathbf{B}\cdot\nabla)}{\mu}\mathbf{B} - \nabla\left(\frac{B^2}{2\mu}\right) \ , \tag{4.13}$$

where the first term on the right-hand side represents a magnetic tension force due to the curvature of field lines and the second term is a magnetic pressure force which acts from areas of strong field to areas of weak field.

It is interesting to identify the effects of these two components in Figure 4.4a. The tension force clearly acts *along* the current sheet and balances the component of the prominence weight in this direction ($\hat{\mathbf{t}}$). There is a jump in the magnetic pressure (B^2) across the sheet (illustrated in Figure 4.4b), the total field being stronger on the lower/equatorward side of the sheet, and it is the resulting magnetic pressure gradient that balances the component of prominence weight in the normal direction ($\hat{\mathbf{n}}$).

Force balance at the sheet gives

$$\mathbf{j}\times\mathbf{B} = -\rho\mathbf{g} \ ,$$

which leads to the result

$$m_A \ \mu \ g = [B_t](s) \ B_{x0} \ , \tag{4.14}$$

where m_A is the mass per unit area of the current sheet surface and $[B_t](s)$ is the jump in the tangential field component across the sheet. Note that

$$[B_t](s) = B_{t_L}(s) - B_{t_R}(s) = 2B_{t_L}(s) \ ,$$

where B_{t_L} is the tangential component at the left edge of the neutral sheet. Thus, the solid curve in Figure 4.3b, showing $[B_t]$, gives the basic variation of mass density along the sheet.

4.5 Perturbation Analysis

The parameters of this system are B_{x0}, B_{y0} and m. From these we can form one dimensionless parameter,

$$B^*_{x0} = \frac{B_{x0}}{B_{y0}} ,$$

which gives a measure of the angle of the field lines from the vertical, as $w \to \infty$. We also note that the combination m/B_{y0} has dimensions of (length)^2 and so the natural non-dimensionalisation for the variables is

$$\mathbf{B}^* = \frac{\mathbf{B}}{B_{y0}} \quad , \quad \mathbf{r}^* = \frac{\mathbf{r}}{\sqrt{m/B_{y0}}} .$$

The three dimensionless end-point equations may then be written using the vector notation

$$\mathbf{F}(\mathbf{r}^*_{\mathbf{e}}, B^*_{x0}) = \mathbf{0} , \tag{4.15}$$

where $F_i(\mathbf{r}^*_{\mathbf{e}}, B^*_{x0})$ represents the expression given by equation (B 1), (B 2) or (B 3) as i assumes the integer value of 1, 2 or 3, respectively. If we expand these equations about the fixed point solution $(\mathbf{R}^*_E, B^*_{X0})$ we obtain

$$\begin{aligned} \mathbf{F}(\mathbf{R}^*_E, B^*_{X0}) + \frac{\partial \mathbf{F}}{\partial \mathbf{r}^*_{\mathbf{e}}}(\mathbf{R}^*_E, B^*_{X0}) \cdot \delta \mathbf{r}^*_{\mathbf{e}} &+ \frac{\partial \mathbf{F}}{\partial B^*_{x0}}(\mathbf{R}^*_E, B^*_{X0}) \cdot \delta B^*_{x0} + \\ &+ \text{second order terms} + \ldots = \mathbf{0} , \end{aligned} \tag{4.16}$$

where

$$\mathbf{F}(\mathbf{R}^*_E, B^*_{X0}) \equiv \mathbf{0} . \tag{4.17}$$

Henceforth the stars will be dropped for brevity.

We may write the expansion (4.16) using the notation

$$\mathbf{F}^{(0)} + \mathbf{F}^{(1)} + \mathbf{F}^{(2)} + \ldots = \mathbf{0}$$

where the superscripts represent the order of the terms in the expansion. In this way, any single term of order j may be written as $F_i^{(j)}$, $(i = 1..3)$.

In this expansion, the order-zero terms provide the system of equations which determine the end-points of the current sheet while the first-order terms allow small changes in the end-points to be evaluated, given a corresponding perturbation of the system. It will be shown that this perturbation analysis holds except for the particular instance in which an infinitesimal current sheet forms from the neutral point as the system is initially perturbed. In this case, the second-order terms must be introduced to enable a complete solution for the sheet. The details of this analysis are given in the following subsections.

4.5.1 Order Zero Terms : Fixed-Point Solution

The vector equation (4.17) may easily be solved for the neutral point case, $\mathbf{R}_E = \mathbf{r}_N$. In this case, only two of the component equations ($i = 1, 2$) are needed to solve for x_N and y_N, whilst the third equation happens to be a consequence of the first two, as expressed in the following linear combination:

$$F_3^{(0)} = 2x_N F_2^{(0)} - (x_N^2 + y_N^2) F_1^{(0)} \ . \tag{4.18}$$

Hence, we obtain

$$B_{x0} = \frac{(x_N^2 - y_N^2)}{2x_N y_N} \quad , \quad 2x_N y_N = -(x_N^2 + y_N^2)^2 \ , \tag{4.19}$$

from which the solution, with $m > 0$ and $B_{y0} > 0$, may be explicitly written (Appendix D) as

$$x_N = -\frac{\sqrt{2(\sqrt{B_{x0}^2+1} - B_{x0})^3}}{1 + (\sqrt{B_{x0}^2+1} - B_{x0})^2} \ , \qquad y_N = \frac{\sqrt{2(\sqrt{B_{x0}^2+1} - B_{x0})}}{1 + (\sqrt{B_{x0}^2+1} - B_{x0})^2} \ . \tag{4.20}$$

Figure 4.5 shows the position of the neutral point as B_{x0} is varied. The neutral point approaches the origin as $B_{x0} \to \pm\infty$, corresponding to a horizontal background field. For $B_{x0} = 0$, the field lines are vertical at a large distance and the neutral point is located at

$$x_N = -\frac{1}{\sqrt{2}} \quad , \quad y_N = \frac{1}{\sqrt{2}} \ .$$

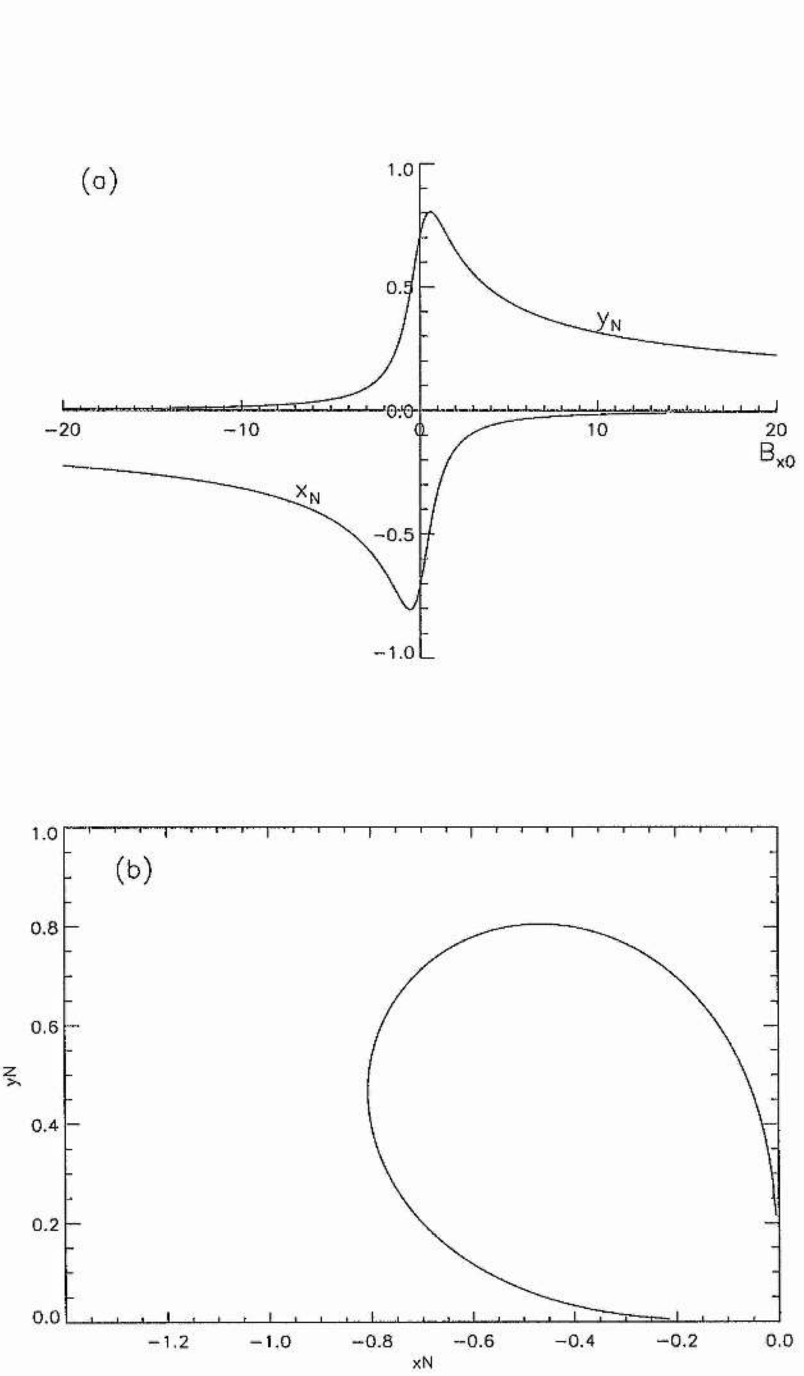

Figure 4.5: (a) The dependence of x_N and y_N on B_{x0}. (b) The path of the neutral point as B_{x0} is varied.

4.5.2 First-Order Terms : Evolution of the Current Sheet

Now consider equation (4.16) taken to the first order, i.e.

$$\begin{pmatrix} \frac{\partial F_1}{\partial x_1} & \frac{\partial F_1}{\partial x_2} & \frac{\partial F_1}{\partial y_1} & \frac{\partial F_1}{\partial y_2} \\ \frac{\partial F_2}{\partial x_1} & \frac{\partial F_2}{\partial x_2} & \frac{\partial F_2}{\partial y_1} & \frac{\partial F_2}{\partial y_2} \\ \frac{\partial F_3}{\partial x_1} & \frac{\partial F_3}{\partial x_2} & \frac{\partial F_3}{\partial y_1} & \frac{\partial F_3}{\partial y_2} \end{pmatrix} \begin{pmatrix} \delta x_1 \\ \delta x_2 \\ \delta y_1 \\ \delta y_2 \end{pmatrix} + \begin{pmatrix} \frac{\partial F_1}{\partial B_{x0}} \\ \frac{\partial F_2}{\partial B_{x0}} \\ \frac{\partial F_3}{\partial B_{x0}} \end{pmatrix} \delta B_{x0} = \begin{pmatrix} 0 \\ 0 \\ 0 \end{pmatrix}$$

This system may be solved for $\delta \mathbf{r_e}$ by imposing (a) the change in height ($\delta h = \delta y_2 - \delta y_1$) of the current sheet, and (b) a perturbation, δB_{x0}. Then we find

$$\begin{pmatrix} \frac{\partial F_1}{\partial x_1} & \frac{\partial F_1}{\partial x_2} & \frac{\partial F_1}{\partial y_1} + \frac{\partial F_1}{\partial y_2} \\ \frac{\partial F_2}{\partial x_1} & \frac{\partial F_2}{\partial x_2} & \frac{\partial F_2}{\partial y_1} + \frac{\partial F_2}{\partial y_2} \\ \frac{\partial F_3}{\partial x_1} & \frac{\partial F_3}{\partial x_2} & \frac{\partial F_3}{\partial y_1} + \frac{\partial F_3}{\partial y_2} \end{pmatrix} \begin{pmatrix} \delta x_1 \\ \delta x_2 \\ \delta y_1 \end{pmatrix} = - \begin{pmatrix} \frac{\partial F_1}{\partial B_{x0}} \\ \frac{\partial F_2}{\partial B_{x0}} \\ \frac{\partial F_3}{\partial B_{x0}} \end{pmatrix} \delta B_{x0} - \begin{pmatrix} \frac{\partial F_1}{\partial y_2} \\ \frac{\partial F_2}{\partial y_2} \\ \frac{\partial F_3}{\partial y_2} \end{pmatrix} \delta h$$

or

$$A\,\mathbf{X} \;=\; \mathbf{Y} \;+\; \mathbf{Z}\;,$$

and so, if $\det(A) \neq 0$, we may invert A to find the solution:

$$\mathbf{X} \;=\; A^{-1}(\mathbf{Y}+\mathbf{Z})\;.$$

Thus, given a small perturbation of the parameter, δB_{x0}, and a small change in the height of the current sheet, the corresponding increment, $\mathbf{X}$, in the end-points is determined and so the new end-points are given by

$$\mathbf{r_e} = \mathbf{R}_E + \delta \mathbf{r_e}\;,$$

where $\delta \mathbf{r_e} = (\delta x_1, \delta y_1, \delta x_2, \delta h + \delta y_1)$. In this way a linear iterative scheme may be set up so that the evolution of the current sheet is studied as the external parameters are varied.

Degeneracy of the Solution

A problem occurs when considering the initial step in this iteration, i.e. the splitting of the X-type neutral point, $\mathbf{r_N} = (x_N, y_N, x_N, y_N)$, into an *infinitesimal* current sheet with end-points $\mathbf{r_e} = \mathbf{r_N} + \delta\mathbf{r_e}$. Due to the bifurcation of the neutral point, which is essentially two coincidental end-points, into two distinct end-points, the matrix A evaluated at $\mathbf{r_N}$ is degenerate with $\mathrm{Rank}(A) = 2$. In this case, the initial 3×4 matrix in this section contains two pairs of identical columns, since

$$\frac{\partial F_i}{\partial x_1} = \frac{\partial F_i}{\partial x_2} = \frac{\partial F_i}{\partial x_N} \quad , \quad \frac{\partial F_i}{\partial y_1} = \frac{\partial F_i}{\partial y_2} = \frac{\partial F_i}{\partial y_N} \qquad (i = 1 \ldots 3) \ .$$

Then the matrix equation reduces to

$$\begin{pmatrix} \frac{\partial F_1}{\partial x_N} & \frac{\partial F_1}{\partial y_N} \\ \frac{\partial F_2}{\partial x_N} & \frac{\partial F_2}{\partial y_N} \\ \frac{\partial F_3}{\partial x_N} & \frac{\partial F_3}{\partial y_N} \end{pmatrix} \begin{pmatrix} \delta x_1 + \delta x_2 \\ \delta y_1 + \delta y_2 \end{pmatrix} = - \begin{pmatrix} \frac{\partial F_1}{\partial B_{x0}} \\ \frac{\partial F_2}{\partial B_{x0}} \\ \frac{\partial F_3}{\partial B_{x0}} \end{pmatrix} \delta B_{x0}$$

and so only the 'mid-point', $(\delta x_1 + \delta x_2 \ , \ \delta y_1 + \delta y_2)$, of the infinitesimal sheet may be ascertained. Again, the third equation may be written in terms of the first two so that

$$F_3^{(1)} = 2x_N F_2^{(1)} - (x_N^2 + y_N^2) F_1^{(1)} \ . \tag{4.21}$$

However, since $\delta y_2 - \delta y_1$ is imposed, the vertical coordinates of the sheet may be explicitly determined, although x_1 and x_2 are not explicitly known, nor is the *orientation* of the sheet. Thus, to determine exactly the position of this sheet, the second-order terms in the expansion must be considered.

4.5.3 Second-Order Terms : Determination of the Infinitesimal Sheet

We now make a change of variable :

$$\begin{aligned} \delta x_1 &= \delta x_+ - \delta x_- \ , \\ \delta x_2 &= \delta x_+ + \delta x_- \ , \\ \delta y_1 &= \delta y_+ - \delta y_- \ , \\ \delta y_2 &= \delta y_+ + \delta y_- \ , \end{aligned}$$

so that the subscripts $(+)$ and $(-)$ represent the mid-point values and the increments in the width and height ($\delta h = 2\delta y_-$) of the sheet, respectively.

The system, to second order, is now written

$$F_i^{(1)} + F_i^{(2)} = 0 \qquad (i = 1\ldots 3)\ ,$$

since the zeroth-order terms are identically zero (fixed point solution).

To solve this system, we take the combination given by equations (4.18) and (4.21), namely

$$(F_3^{(1)} + F_3^{(2)}) - 2x_N(F_2^{(1)} + F_2^{(2)}) + (x_N^2 + y_N^2)(F_1^{(1)} + F_1^{(2)}) = 0\ .$$

Under this algebraic combination, the first-order terms drop out, due to (4.21), as do the purely quadratic terms. Only the mixed terms of second order are left and so the resulting equations may easily be solved, after back substitution of δx_+ and δy_+, for our final unknown, δx_-. The whole solution is given by

$$\delta x_+ \;=\; \frac{x_N^2\, y_N\, (3\, y_N^2 - x_N^2)}{\left(x_N^2 + y_N^2\right)^2}\, \delta B_{x0}\ , \tag{4.22}$$

$$\delta y_+ \;=\; \frac{x_N\, y_N^2\, (y_N^2 - 3\, x_N^2)}{\left(x_N^2 + y_N^2\right)^2}\, \delta B_{x0}\ , \tag{4.23}$$

$$\delta x_{-_1} \;=\; \frac{y_N^3 - 3\, x_N^2 y_N + \left(x_N^2 + y_N^2\right)^{3/2}}{x_N\, (x_N^2 - 3\, y_N^2)}\, \delta h/2\ , \tag{4.24}$$

$$\delta x_{-_2} \;=\; \frac{y_N^3 - 3\, x_N^2 y_N - \left(x_N^2 + y_N^2\right)^{3/2}}{x_N\, (x_N^2 - 3\, y_N^2)}\, \delta h/2\ . \tag{4.25}$$

It is interesting to note that there are in fact two solutions for δx_-. Consider the product

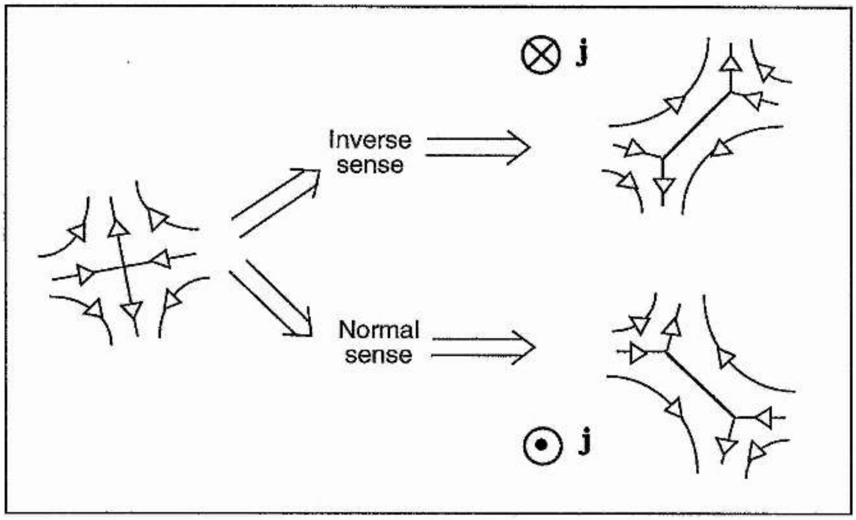

Figure 4.6: Splitting of the X-type neutral point to produce infinitesimal current sheets of either normal or inverse sense.

of the gradients of these two sheets :

$$\begin{aligned}\frac{\delta y_-}{\delta x_{-_1}} \cdot \frac{\delta y_-}{\delta x_{-_2}} &= \frac{x_N^2(x_N^2 - 3y_N^2)^2}{(y_N^3 - 3x_N^2 y_N)^2 - (x_N^2 + y_N^2)^3} \\ &= \frac{x_N^2(x_N^2 - 3y_N^2)^2}{-x_N^2(x_N^4 - 6x_N^2 y_N^2 + 9y_N^4)} = -1 \ ,\end{aligned}$$

and hence these solutions represent perpendicular infinitesimal sheets. Which of these solutions arises will depend on whether the field is compressed or stretched at the X-point. The two corresponding field topologies will result in sheets that have oppositely directed currents (see Figure 4.6). From now on, we will refer to these two types of solution as either *normal* or *inverse* sheets as they tend to generate solutions that correspond to normal or inverse-polarity prominences, respectively. This is because, for the required upward Lorentz force on the sheet, the current direction determines the sign of the applied prominence field, B_{x0}. For example, we refer to the sheet in Figure 4.2b as an inverse sheet.

The above solutions, (4.22) - (4.25), with (4.20) tell us that the mid-point of the infinitesimal sheet and its orientation tangent, $\delta y_- / \delta x_-$, depend purely upon the value of B_{x0}. The variation of the sheet angle with B_{x0} is shown in Figure 4.7. Considering the

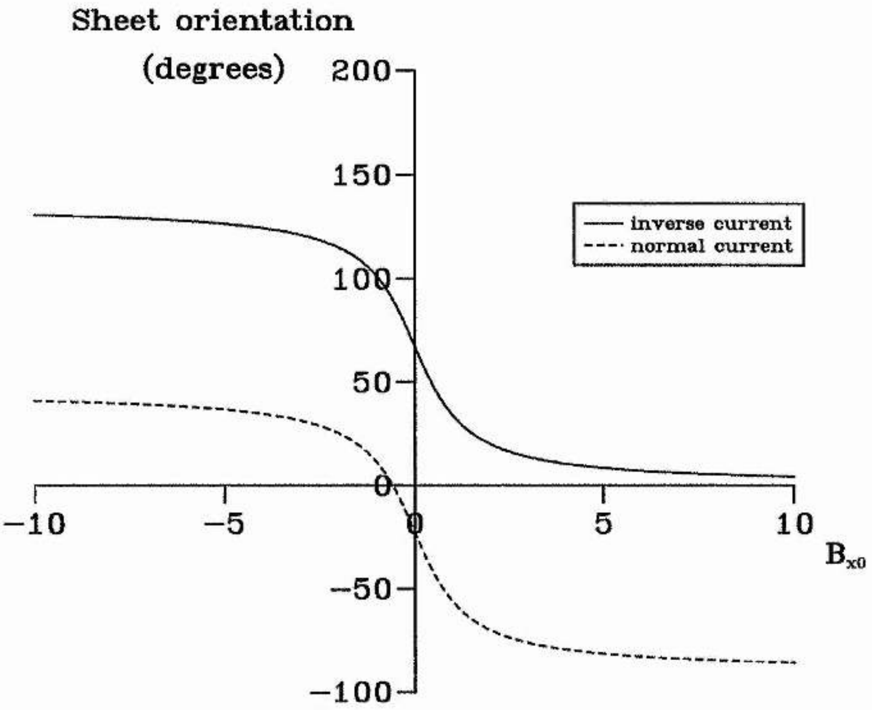

Figure 4.7: Orientation of the infinitesimal sheet for the normal and inverse sheet cases.

inverse sheet, we see that for $B_{x0} = 0$, the sheet is inclined at an angle of $\arctan(1 + \sqrt{2}) = 67.5°$ to the horizontal. As B_{x0} is increased, this angle decreases and the sheet moves clockwise along a path close to that in Figure 4.5b. It approaches the origin, as $B_{x0} \to \infty$, and the sheet becomes horizontally oriented. As B_{x0} is decreased from zero, the angle increases until the sheet is vertical (when $B_{x0} = 1/\sqrt{3}$ and $y_N = -x_N/\sqrt{3}$) and as $B_{x0} \to -\infty$, the angle asymptotes to 135°.

4.5.4 Calculation of the Current in the Infinitesimal Sheet

Consider the sheet to be a small perturbation about the neutral point, i.e.

$$\begin{aligned} w_1 &= w_N + \delta w_1 \quad ; \quad w_2 = w_N + \delta w_2 \ , \\ \bar{w}_1 &= \bar{w}_N + \delta \bar{w}_1 \quad ; \quad \bar{w}_2 = \bar{w}_N + \delta \bar{w}_2 \ . \end{aligned}$$

Now make an expansion of the field (4.9) to investigate its behaviour in the neighbourhood of this current sheet. Setting $w = w_N + \delta w$, where $\delta w_1, \delta w_2 \ll \delta w \ll 1$, we have

$$\begin{aligned} -\frac{i}{\pi}Q(w) &= -\frac{i}{\pi}\left[(\delta w - \delta w_1)(\delta w - \delta w_2)(\delta w - \delta\bar{w}_1 + 2\mathrm{i}y_N)(\delta w - \delta\bar{w}_2 + 2iy_N)\right]^{\frac{1}{2}} \\ &= \frac{2y_N}{\pi}\delta w\left[\left(1-\frac{\delta w_1}{\delta w}\right)\left(1-\frac{\delta w_2}{\delta w}\right)\left(1+\frac{\delta w - \delta\bar{w}_1}{2iy_N}\right)\left(1+\frac{\delta w - \delta\bar{w}_2}{2iy_N}\right)\right]^{\frac{1}{2}} . \end{aligned}$$

The field in the neighbourhood of the infinitesimal sheet will behave like the field due to a line current,

$$B(w) = \frac{s}{w} ,$$

where s is a real constant. Thus, the coefficient of the $O(1/\delta w)$ term in the expansion of (4.9), which we now denote by I_l, will give the *total current* in the current sheet. We should see, then, that the imaginary part of this coefficient is zero.

The dominant $1/\delta w$ term in the expansion of $-(i/\pi)Q(w)$ is given by

$$-\frac{y_N}{\pi\delta w}(\delta w_{-_k})^2 \quad , \quad k = 1, 2 ,$$

where we have allowed for the two solutions, δx_{-_1} and δx_{-_2}, by setting $\delta w_{-_k} = \delta x_{-_k} + i\delta y_{-}$. This term is multiplied by the $O(1)$ term which is contained in the braces in the expression (4.9) for $B(w)$. In this case the integral may be evaluated analytically by expressing it as a contour integral (as demonstrated for the analogous integral in Appendix A), i.e.

$$\oint_C \frac{d\xi}{(\xi - w_N)^2(\xi - \bar{w}_N)} ,$$

where the contour C encloses the whole of the upper-half plane. This is solved by finding the residue at the double pole, $\xi = w_N$.

Thus we obtain,

$$I_{l_k} = -\frac{y_N}{\pi}(\delta w_{-_k})^2\left\{2\pi i \lim_{\xi\to w_N}\frac{d}{d\xi}\left(\frac{1}{\xi - \bar{w}_N}\right) - \frac{\pi}{w_N}\frac{(3x_N - iy_N)}{(x_N^2 + y_N^2)^2}\right\} .$$

After use of equation (4.19) we can show that, for the dimensionless current, I_{l_k},

$$Re(I_{l_k}) = \frac{(x_N^2 + y_N^2)^2\delta x_{-_k}\delta y_{-}}{x_N^2 y_N(x_N^2 - 3y_N^2)} \quad , \quad Im(I_{l_k}) = 0 ,$$

as required.

4.5.5 Results for the Infinitesimal Sheet

We note here that it is impractical to impose the parameter δy_- since this implies an infinite sheet width, δx_{-_k}, as the sheet becomes horizontal. It is better to study the behaviour of the current and forces on the sheet for an imposed sheet length, δs.

The inclination, α, of the sheet, illustrated in Figure 4.7, is given by

$$\tan \alpha_k = \frac{\delta y_-}{\delta x_{-_k}} ,$$

and is fixed for an imposed value of B_{x0}. As the sheet is infinitesimally small, we may consider it to be a straight element of length δs such that

$$\delta s^2 = \delta x^2_{-_k} + \delta y^2_-$$

and so

$$\delta y_- = \sin(\alpha_k) \delta s .$$

Therefore, the current in the sheet is modified to

$$I_{l_k} = \frac{(x_N^2 + y_N^2)^2}{2x_N^2 y_N (x_N^2 - 3y_N^2)} \sin(2\alpha_k) \delta s^2 . \tag{4.26}$$

Using the previous result that the two sheet solutions are perpendicular, i.e. $\tan \alpha_1 \cdot \tan \alpha_2 = -1$, it is easily shown that $I_{l_1} = -I_{l_2}$, so the currents in the two sheets are indeed oppositely directed and of equal magnitude.

In order to obtain a prominence solution, we superimpose a counter-horizontal field, B_{x0_k}, threading the sheet and so the force on the sheet is proportional to $I_{l_k} B_{x0_k}$. Figure 4.8 shows this force and the current in the sheet for the inverse current sheet solution as the value of B_{x0} is varied. The results for the normal current sheet are obtained by a reflection in the x-axis.

For the inverse current sheet we observe that prominence solutions are only valid for $B_{x0} > 0$ (since the Lorentz force must be positive). This means that the field threading the prominence, $B_{x0_1} < 0$. The opposite is true for the normal current sheet.

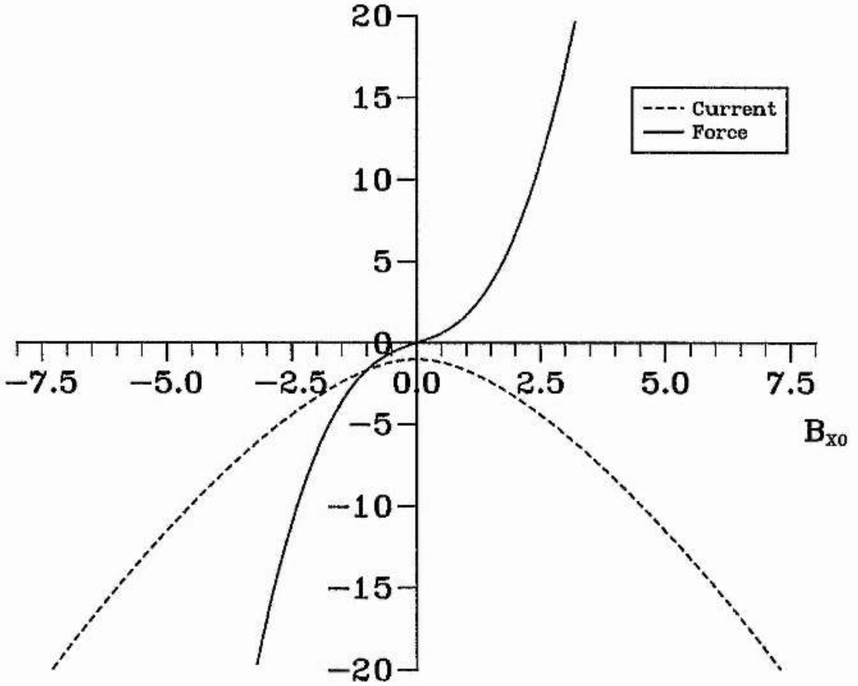

Figure 4.8: The variation of current and force on the infinitesimal sheet of inverse sense.

4.6 Resulting Solutions for a Finite, Curved Prominence

4.6.1 Field Topology

Once the infinitesimal sheet has been computed, it is a simple matter to expand the sheet, as described in Section 4.5.2, to produce the final configuration incorporating a finite, curved prominence sheet. An illustration of the evolution of the current sheet from the neutral point is shown in Figure 4.9. The paths of the two end-points are traced and a series of intermediate positions of the sheet is shown.

The ultimate shape and orientation of the sheet is determined by several factors. For example, the initial value of B_{x0} controls the orientation of the infinitesimal sheet (Figure 4.7) and then varying the ratio $\delta B_{x0}/\delta h$ at each step in the iteration allows a whole class of sheet shapes and sizes. In the examples of Figure 4.9, the initial value of B_{x0} is zero and we have fixed $\delta h = 2\ \delta B_{x0}$.

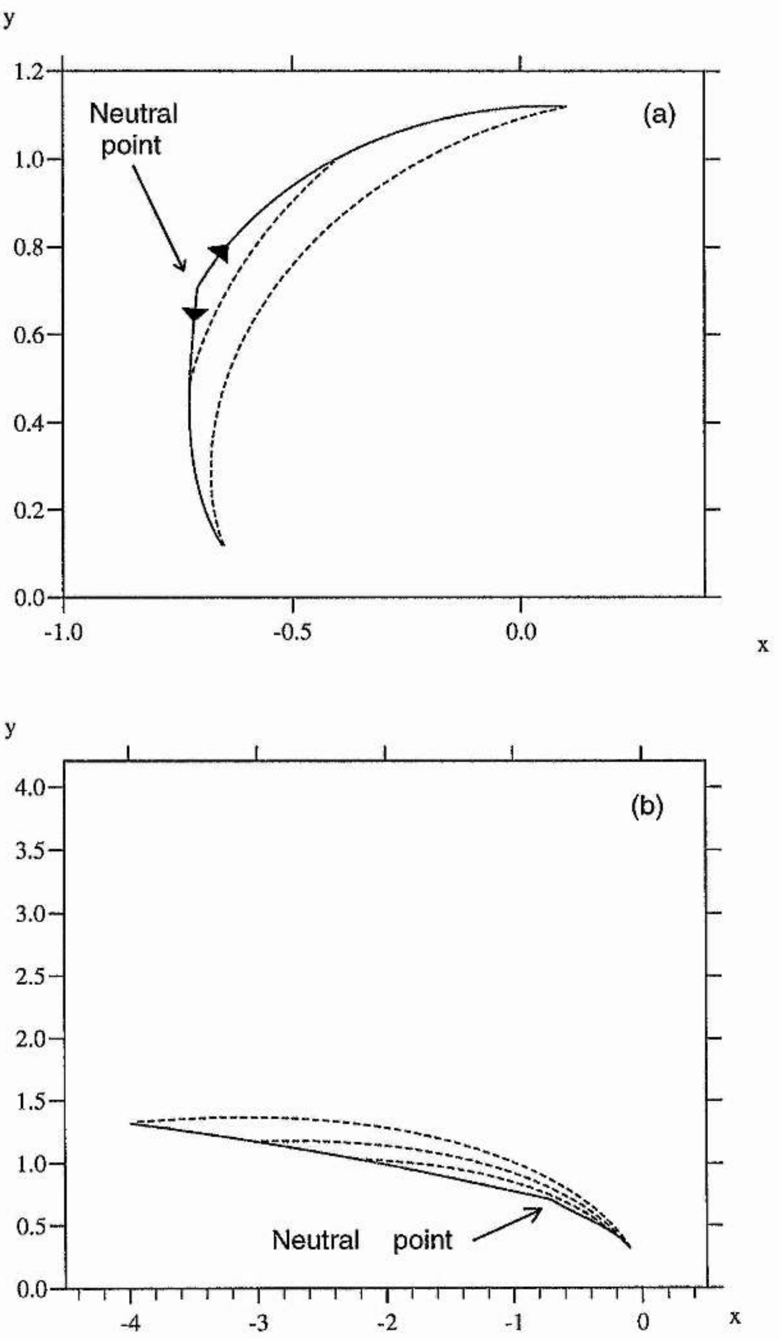

Figure 4.9: The growth of (a) inverse and (b) normal current sheets, as the external parameters are varied. The dotted lines illustrate intermediate sheet positions.

An example of a final prominence field for the inverse current sheet solution was previously shown in Figure 4.4a. This solution is suitable as a model of the field for a polar-crown prominence.

Figure 4.10 demonstrates two normal current sheet solutions where we observe a different field topology. Figure 4.10a was formed from an infinitesimal sheet oriented at an angle of 25° ($B_{x0} = -2.0$). Here, the prominence sheet lies in a locally arcade-like region of field with an X-type neutral point appearing *above* the prominence! The final value of B_{x0} has been increased to -2.2, yet for observed values of the horizontal component ($|B_{x0}| \approx 1.0$) the sheet's orientation will be very close to the horizontal. The sheet in Figure 4.10b is located in a topologically different region of field such that the field lines that pass through the prominence are open. This time, the sheet is inclined at a small *negative* angle. Again, large angles are not possible, since, in this case, a positive value of B_{x0} would be required resulting in a downward Lorentz force. In this example, the final value of B_{x0} is only -0.1.

This normal sense current cannot give rise to polar-crown prominence fields as the resulting solutions all lie in normal-polarity fields which is contrary to the observations. In any case, it would seem unlikely that these types of prominence would have chance to form, due to the lack of field line dips in the limit as the sheet tends to zero. However, it does demonstrate nicely the alternative solutions available using this method.

4.6.2 Total Mass of the Prominence

If (4.14) is integrated along the sheet we may obtain the mass per unit length (in the $\hat{\mathbf{z}}$-direction) of the sheet as

$$M_l = \int_0^{s^*} m_A(s)\, ds \ ,$$

where the integration is terminated at $w = w_2$ ($s = s^*$).

As an example, taking photospheric values of $B_{y0} = 10^{-3}\ T$ ($10\ G$) and dipole moment $= 10^{-3}\ T\ m^2$ with a prominence field of $B_{x0} = 5 \times 10^{-4}\ T$ ($5\ G$), we obtain a value of

$$M_l = 1.5 \times 10^5\ kg\ m^{-1} \ ,$$

which is of the observed order of magnitude, based on a particle density of $10^{17}\ m^{-3}$ and

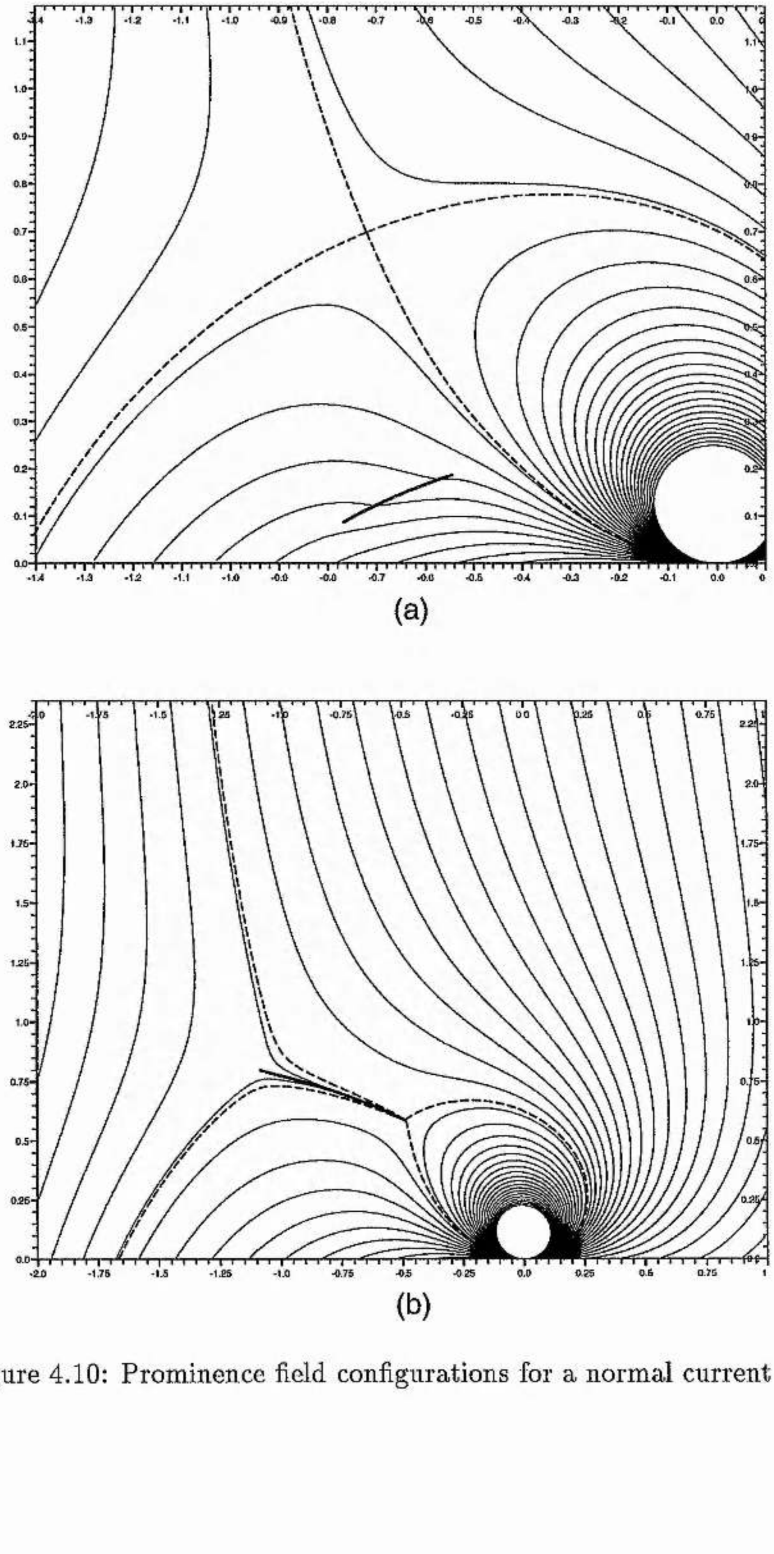

(a)

(b)

Figure 4.10: Prominence field configurations for a normal current sheet.

typical dimensions for the vertical extent and height of a mature high-latitude quiescent prominence.

4.7 Discussion

In this chapter we have set up prominence sheet equilibria in a potential field for a photospheric distribution that includes a dipole superimposed on an infinite domain of constant vertical flux. The direction of the current in the sheet determines whether the prominence thus formed will be of normal or inverse-polarity.

Considering the normal-polarity solutions (Figure 4.10), we observe that the sheet will always be slanted towards the horizontal since the more vertically oriented sheets require a large positive value of B_{x0} which would result in a downward force in the final prominence solution. These solutions almost certainly lie in unstable magnetic configurations and the lack of pre-prominence dips (in the limit as the sheet tends to zero) raises the question: how does the dense material originally collect there? Thus it seems improbable that a normal-polarity prominence would form in such a polar field configuration. This is reflected in the observations.

Conversely, on examination of the inverse-polarity solutions we see that the sheet lies in a tripolar configuration. The dips present in such a field are sufficiently large to allow prominence material to collect and form into a sheet that is stable to small perturbations of the field. As the dips lie in a curved geometry the prominence assumes a similar shape, its upper section tilted towards the equator: yet every point on the prominence is still subject to an upwardly directed Lorentz force. The mass density of this type of prominence, computed by taking observed values of the photospheric and prominence magnetic field, is of the correct order of magnitude.

Given a finite sheet solution, the first-order terms in the expansion of the end-point equations allow changes in the sheet to be computed for a perturbation in the parameters B_{x0} and h. In the purely potential case, however, where the end-points are coincident, the first-order terms only determine the mid-point of the infinitesimal sheet and so the next order must be considered. This permits two perpendicular solutions of opposing current sense that are associated with either a compression or stretching of the field at the neutral point.

This model, which considers an infinite domain of vertical flux, does not account completely for the original scenario illustrated in Figure 4.1a, because the bipolar region would have to move across such field lines. Thus, a modified distribution is required to include finite sources of flux. This forms the subject of the next chapter, although we do not consider the construction of the prominence sheet there.

The generation of curved, weighted current sheets, with a prescribed distribution of photospheric flux, as presented here, has not previously been possible and so we consider this analysis to be a significant advance within this branch of prominence modelling.

Chapter 5

Modified Photospheric Flux Distribution

5.1 Chapter Summary

In this chapter we investigate various potential fields generated from finite sources of photospheric flux to obtain a better approximation for the pre-prominence polar magnetic field. We do not construct the resulting prominence solutions here, although we mention some technical difficulties that may arise in such a formulation, given the considered flux distributions. For each case we study the behaviour of the neutral points, both the position and the orientation, to determine which parameters give field line dips. Solutions are selected for which good dips exist and for which the polar field has the correct type of behaviour. The effect of the solar wind in stretching out the field is included. A possible evolution sequence is given where a region of bipolar flux interacts with the polar field to produce dips, and an alternative formation mechanism is mentioned.

5.2 Introduction

In Chapter 4 a model for the magnetic configuration and magnetohydrostatic support of a polar-crown prominence was presented. This model is based on the supposition that the pre-prominence magnetic field possesses a location of dips in which prominence material may collect and form into the quiescent, elongated structures that are readily observed near the poles of the Sun (McIntosh, 1980). The resultant field of the model consists of a dipole superimposed on an infinite domain of uniform, vertical field. Although this generates the basic structure of the pre-prominence field, it is a somewhat crude flux distribution and needs to be modified by using separate, finite sources of flux. This allows the dipole to be replaced by a more realistic region of bipolar flux and also enables the evolution of the pre-prominence field to be studied. In the original model, the infinite domain of flux prevented such an analysis as it is not feasible to consider a dipole passing through fixed footpoints of open field!

This chapter concentrates on developing a more realistic flux distribution for which the pre-prominence field is a closer fit to the observations. A preliminary analysis is made in Section 5.3 using point sources of flux to help gain some insight into a possible configuration. This is complimented with a study of the behaviour (examining the position and orientation) of the neutral point to determine which parameter values produce magnetic field line dips. This experiment is performed firstly for a series of three sources and then in Section 5.4 for five sources to obtain a symmetric configuration (about the pole) in which the polar field is vertical. A more elaborate model is introduced in Section 5.5 using finite regions of flux to generate a more realistic field. This incorporates the effect of the solar wind in stretching out the field at large distances from the surface. Finally, a discussion in Section 5.6 highlights the main features of these models including the various weaknesses and aspects that need to be rectified and improved in further modelling.

5.3 Three-Source Distribution (Asymmetric Case)

We first consider three separate charges located along the x-axis to represent roughly the polar photospheric distribution by a positive source of unit strength at the pole ($x = 0$) and a bipolar pair of strength $-m$ and $+m$ located at $x = 1$ and $x = x_0$, respectively. The potential field generated from this distribution may be written in complex notation as

$$B(w) = B_y + i\ B_x = \frac{i}{w} - \frac{i\ m}{w-1} + \frac{i\ m}{w-x_0}\ , \tag{5.1}$$

where $x_0 > 1$ and $m > 0$.

Two neutral points (nulls) are present in the field. They are complex conjugates and are located at

$$w_N = x_N + i\ y_N = \frac{x_0 + 1 - m(x_0-1)}{2} \pm \frac{\sqrt{[m(x_0-1)-(x_0+1)]^2 - 4x_0}}{2}\ . \tag{5.2}$$

Note that, in the model, we do not consider any null in the lower-half plane since the photosphere is taken to be the x-axis (or a horizontal cut just above it). Thus, only the region above this axis, i.e. the corona, is of concern. Naturally, the whole field is symmetric in the x-axis (by reflection) as the point sources are all positioned along it.

5.3.1 Location of Dips

Prominence formation may occur due to a thermal instability in a location of horizontal or dipped (concave upward) magnetic field where the plasma can condense without falling down to the solar surface. We therefore seek in this analysis the range of parameters for which dips occur. This can be determined by the orientation of the neutral point and it is there that the subsequent prominence sheet will appear, after utilising the techniques presented in Chapter 4. If the neutral point, which is an X-type neutral point, has the same orientation as that depicted in Figure 5.1a, i.e. the separatrices are locally inclined at $\pi/4$ to the axes, then dips will be present and prominence material may collect, at least locally above the null. However, if the neutral point has the structure of a "+" symbol, e.g. the point $w_N = 0$ in the field $B = we^{-i\pi/2}$ (Figure 5.1b), then there will be no dips and any condensing plasma at the null will be free to slide away, along the lines of force. Of course, this is just a local analysis and there may well be dipped locations in other areas of the

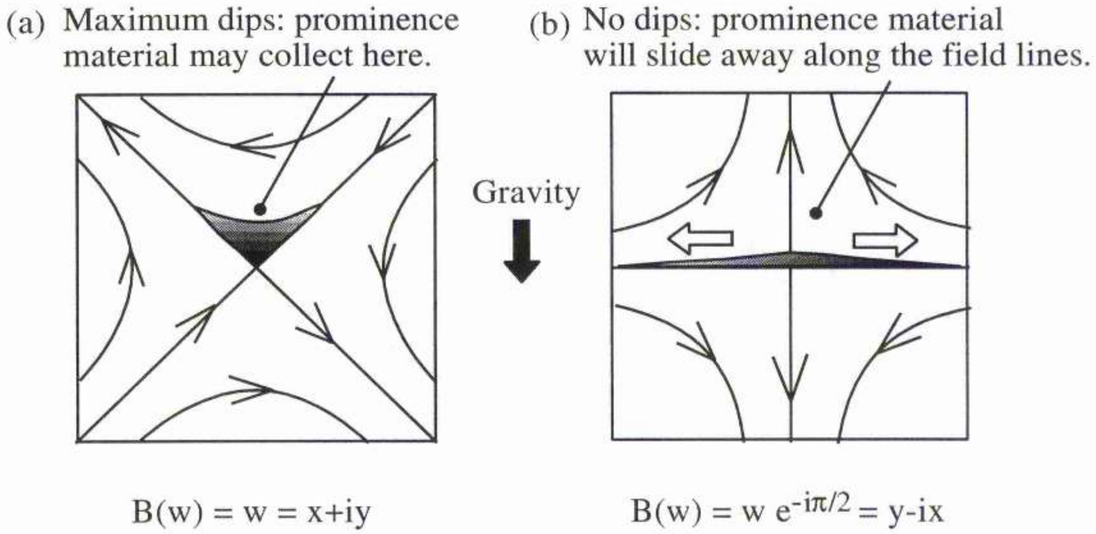

Figure 5.1: The relationship between the orientation of the null and the local existence of field line dips.

field, but that is not considered here.

To investigate which parameters have well developed locations of dips, we need to make an expansion of the field about the neutral point and determine the rotation of the local field from the classic X-point field of Figure 5.1a.

5.3.2 Orientation of the Neutral Point

Setting $w = w_N + \delta w$ in (5.1) we obtain, for $\delta w \ll 1$,

$$\begin{aligned} B(\delta w) &= -i\left[\frac{1}{w_N^2} - \frac{m}{(w_N-1)^2} + \frac{m}{(w_N-x_0)^2}\right]\delta w + \mathrm{O}(\delta w^2) \qquad (5.3) \\ &= \frac{dB(w)}{dw}\cdot\delta w + \mathrm{O}(\delta w^2) \quad , \quad \text{evaluated at } w = w_N \ . \end{aligned}$$

If the coefficient of δw is written in polar notation, then its argument, θ, determines the rotation of the local field from the field $B = \delta w$, and hence the nature of the dips is known.

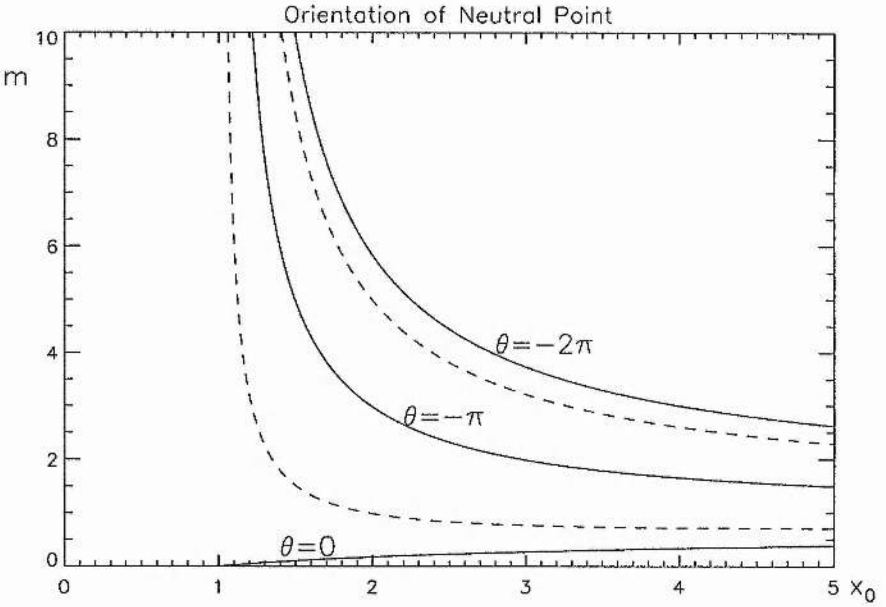

Figure 5.2: Parameter space plot showing the orientation of the neutral point for the asymmetric case.

Various orientations are shown in Figure 5.2 in the parameter space plot where we note that maximum dips are given by the solid curves and no dips occur along the dashed curves.

We now make a qualitative analysis to study the behaviour of the neutral points as m is varied.

5.3.3 Behaviour of the Neutral Points

In this analysis, x_0 remains fixed and the argument of the square root in (5.2),

$$w_A = [m(x_0 - 1) - (x_0 + 1)]^2 - 4x_0 \ , \tag{5.4}$$

is considered. There are three separate cases here corresponding to $w_A > 0$, $w_A = 0$ and $w_A < 0$.

Case i) $w_A > 0$. On-axis Nulls

If w_A is positive then $y_N = 0$ and the two nulls lie on the x-axis equidistant from a central point

$$x_{N0} = \frac{x_0 + 1 - m(x_0 - 1)}{2} \ . \qquad (5.5)$$

This occurs if either

$$a) \quad m < m_- \ = \ \frac{x_0 + 1 - 2x_0^{1/2}}{x_0 - 1} \quad ; \quad x_N > 0 \quad \text{(weak bipole)}$$

or

$$b) \quad m > m_+ \ = \ \frac{x_0 + 1 + 2x_0^{1/2}}{x_0 - 1} \quad ; \quad x_N < 0 \quad \text{(strong bipole)}$$

hold. The orientation of these nulls is given by

$$\theta = (2n+1)\frac{\pi}{2} \quad , \quad n \in \mathcal{Z} \ ,$$

i.e. they are "+ - type" neutral points. First consider the case $m < m_-$. This holds when the bipole strength is so weak that the polar source dominates and the nulls are located between the bipole pair, i.e. $1 < x_N < x_0 \ , \ y_N = 0$. An example of the field lines for this case is shown in Figures 5.3 (a and b). The corresponding region of parameter space lies below the solid curve $\theta = 0$ in Figure 5.2.

As m is increased, the two nulls move together and actually coalesce when $m = m_-$. This is the special case ii)

Case ii) $w_A = 0$. Coincident Nulls

When $m = m_-$ (or $m = m_+$), the argument of the square root is zero and the nulls coincide at the point $(x_{N0} \ , \ 0)$. There is a sudden change in the orientation here to $\theta = 0$ (or $\theta = -2\pi$) corresponding to a location of maximum dips. This is shown in Figure 5.3c. Note that there were large dips already present in case i) but this was the combined effect of two adjacent "+ - type" nulls.

As m is increased further, the nulls move apart but this time in a direction away from the x-axis.

Case iii) $w_A < 0$. Off-axis Nulls

Here $m > m_-$ and $\sqrt{w_A}$ is imaginary so y_N is no longer zero. The nulls are located at $(x_{N0} \ , \ \pm y_N)$ where $y_N = \sqrt{-w_A}/2$. Initially, good dips are present above the upper

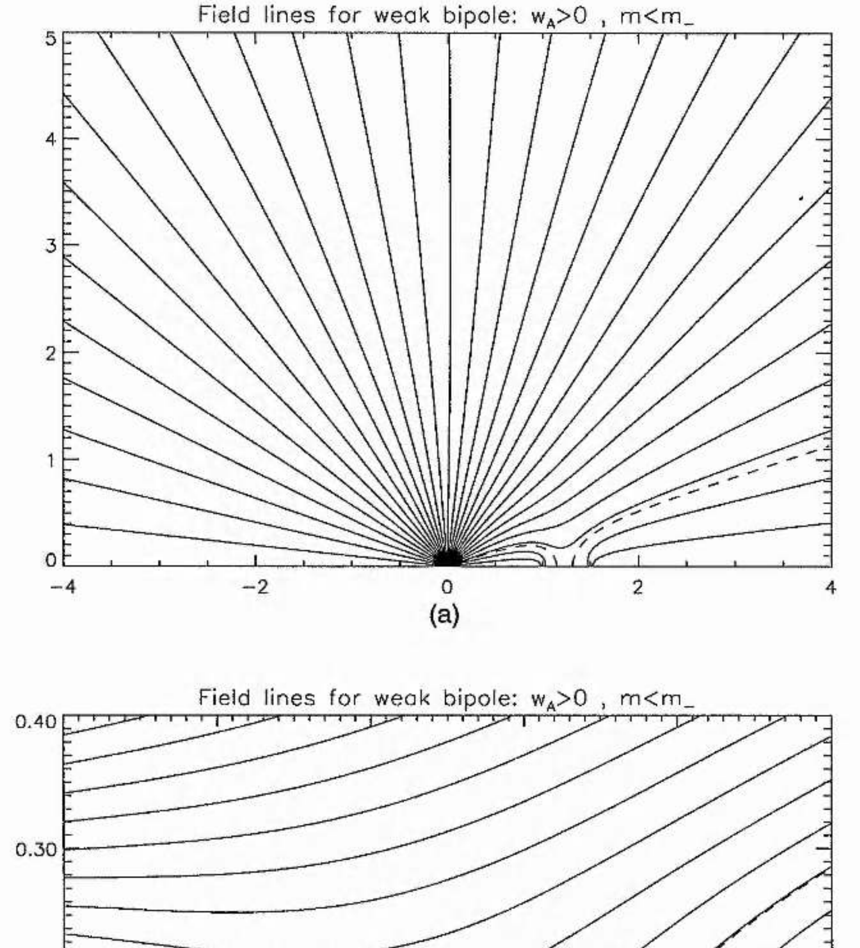

(a)

(b)

Figure 5.3: Field line plots for three charges with the weak bipole case. (c) shows the case of coincident nulls.

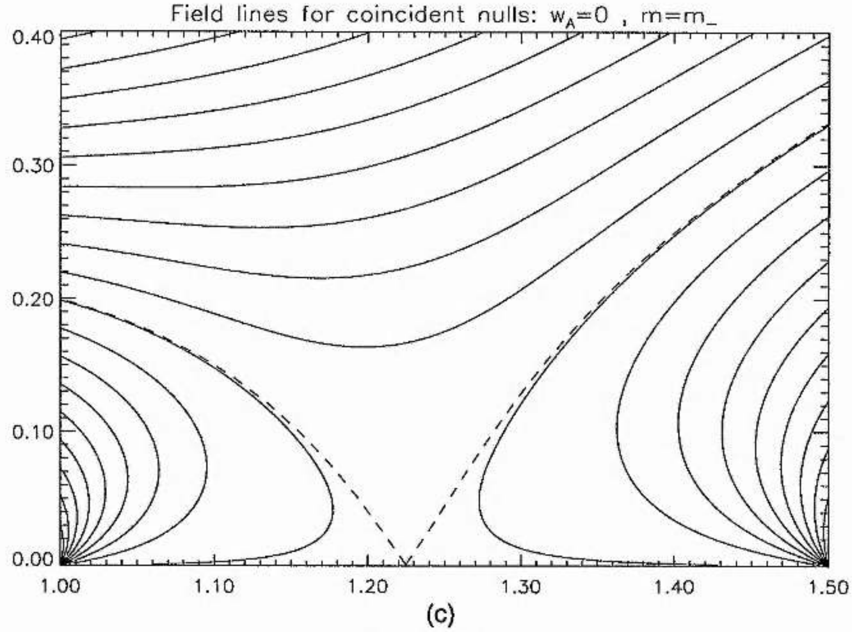

Figure 5.3c

neutral point (x_{N0} , $+y_N$) but as the bipolar strength is increased, θ decreases to a value of $-\pi/2$ as the null rises and rotates to a "+ - type" orientation (see lower dashed curve in Figure 5.2 and Figure 5.4a). Further increase in the bipole strength causes the null to rotate more and rise to a maximum height of $y_N = x_0^{1/2}$ when $m = (x_0+1)/(x_0-1)$ (Figure 5.4b). In addition, it has moved in the horizontal direction and now lies on the y-axis. One can show that $\theta = -\pi$ here and so the local dips are again maximised.

At this point the bipole begins to dominate the polar source, and as it is increased further, the null loses height, moves further to the left, rotates through another minima of dips ($\theta = -3\pi/2$, Figure 5.4c) and eventually reaches the x-axis again when $\theta = -2\pi$ and $m = m_+$ (Figure 5.4d). Finally, case i) is again achieved with $w_A > 0$ and $m > m_+$. At this point, the bipolar field is fully dominant and so the nulls have been 'forced' back onto the x-axis.

It should be stressed here that this sequence is mainly of mathematical and topological interest and cannot be applied to the physical situation because the parameter values are generally far from the observed ones for most cases (the possible solutions are discussed in the following subsection). However, it is a thorough analysis from which we may learn about all the possible topological states and the behaviour of the nulls in order that we may

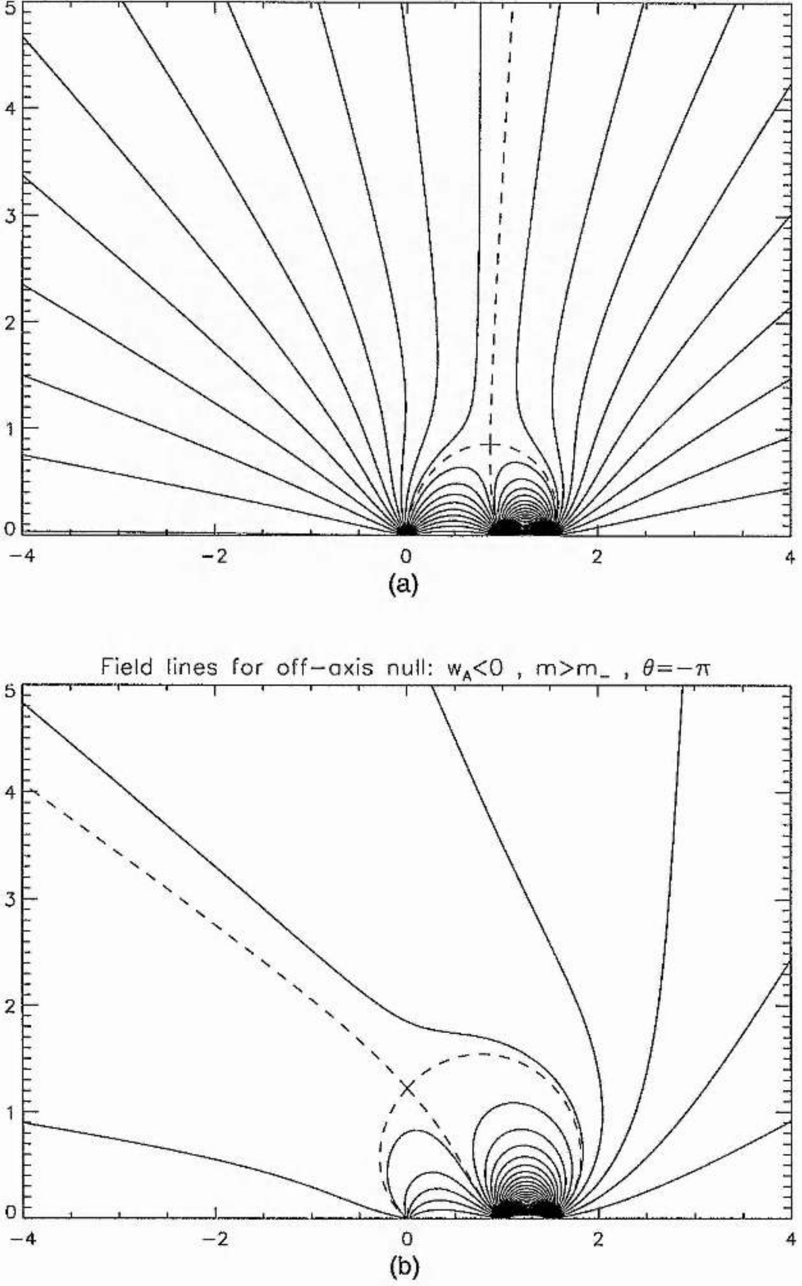

(a)

(b)

Figure 5.4: Field line plots for three charges showing the behaviour of the neutral point (and the associated dips) as the bipolar strength is increased.

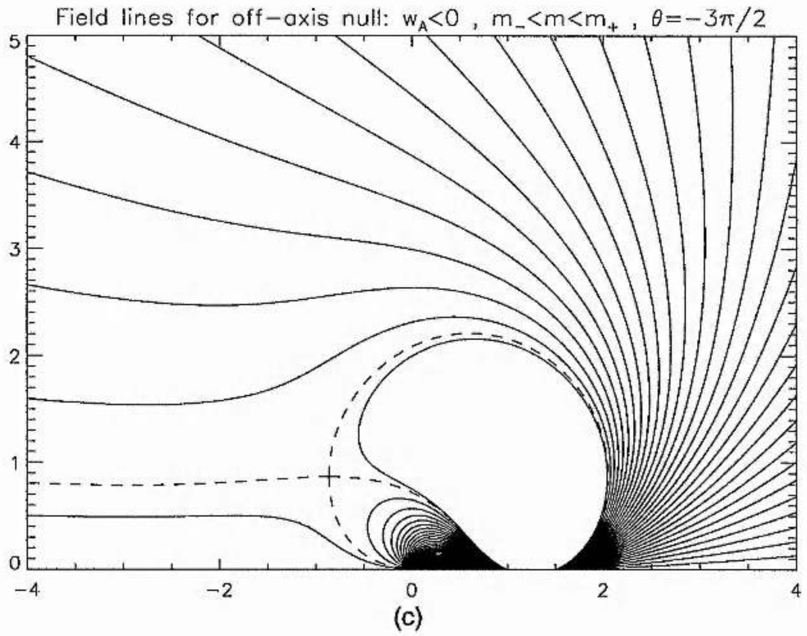

Figure 5.4c

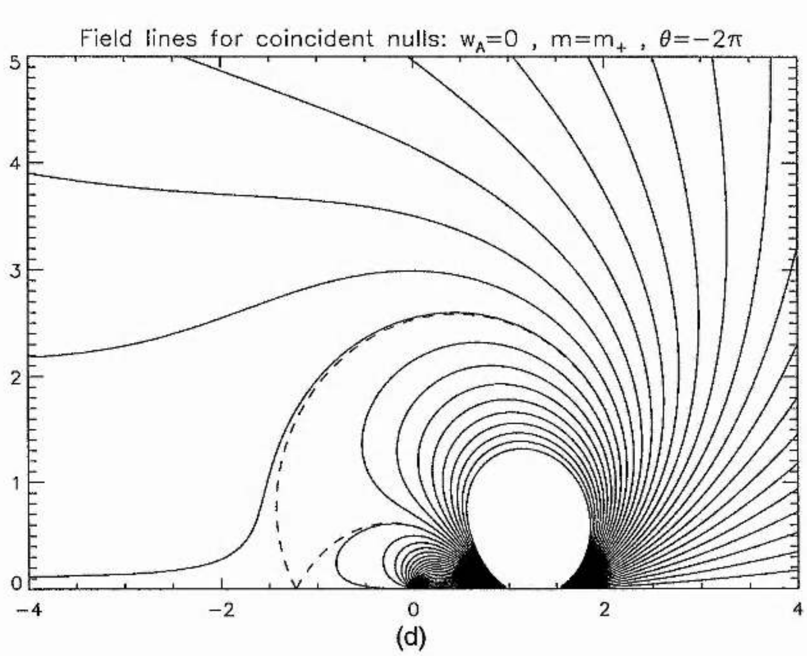

Figure 5.4d

apply this knowledge and experience to the more elaborate model which follows.

5.3.4 Comments on the Three-Source Distribution

The observed values of m and x_0 lie in the ranges

$$2 \leq m \leq 10 \qquad ; \qquad 1.2 \leq x_0 \leq 2 \ ,$$

although it is difficult to place an exact range on x_0 as the observations vary enormously. However, taking $x_0 = 1.5$ fixes the locations of the two polarity inversion lines at $x = 0.5$ and $x = 1.25$, the relative positions of which seem reasonable on examination of a number of magnetograms which show this type of flux distribution. A study of Figure 5.2 then tells us that the weak bipole case ($m \leq m_-$) is not possible. These solutions would be rejected anyway on the grounds that there is no bipolar structure and the polar source is the dominant field. The case $m \geq m_+$ is possible for these parameters but the polar field has been completely swamped by the strength of the bipole and a glance at Figure 5.4d surely eliminates this as a realistic configuration! The remaining possibility for good dips then are solutions close to the $\theta = -\pi$ curve, but again, on examination of Figure 5.4b we note that the polar field is far from vertical and still very distorted.

In order to achieve a good field structure at the pole with a vertical polar field line, it is better to consider a symmetric distribution of sources. This is the aim of the model in the next section.

5.4 Five-Source Distribution (Symmetric Case)

In this section, we again search for the parameters producing field line dips and present some relevant field line plots. For the required symmetry, we add to the previous field a pair of image sources located at $x = -1$ and $x = -x_0$, thus obtaining the expression

$$B(w) = \frac{i}{w} - \frac{i\,m}{w-1} + \frac{i\,m}{w-x_0} - \frac{i\,m}{w+1} + \frac{i\,m}{w+x_0} \ . \tag{5.6}$$

The positions of the nulls are found from the quartic equation

$$w_N^4 + \left[2m(x_0^2-1) - (x_0^2+1)\right] w_N^2 + x_0^2 = 0 \ . \tag{5.7}$$

The coefficients of this equation are real and so the solutions occur in complex conjugate

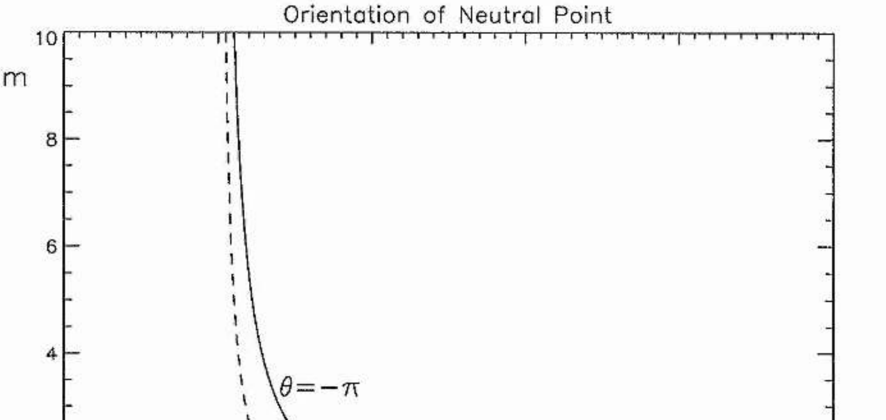

Figure 5.5: Parameter space plot showing the orientation of the neutral point for the symmetric case.

pairs. Also, there are no odd powers of w_N (due to the symmetry of the problem) and so the positions of all four nulls may be determined if we know just one solution, simply by reflections in the axes. Once determined, the behaviour of the nulls may again be considered.

5.4.1 Behaviour of the Neutral Points

Let us consider the null in the first quadrant. The solution curves for its orientation are shown in Figure 5.5. For small values of m, the behaviour of the null is similar to the case with three sources. As m is increased above m_-, where

$$m_- = \frac{x_0 - 1}{2(x_0 + 1)} \, ,$$

the null leaves the x-axis, rises and rotates through a "+ - type" orientation ($\theta = -\pi/2$). As m tends to m_+, given by

$$m_+ = \frac{x_0 + 1}{2(x_0 - 1)} \, ,$$

the null approaches the y-axis where it has a height of $y_N = \sqrt{2x_0}$ and an orientation of

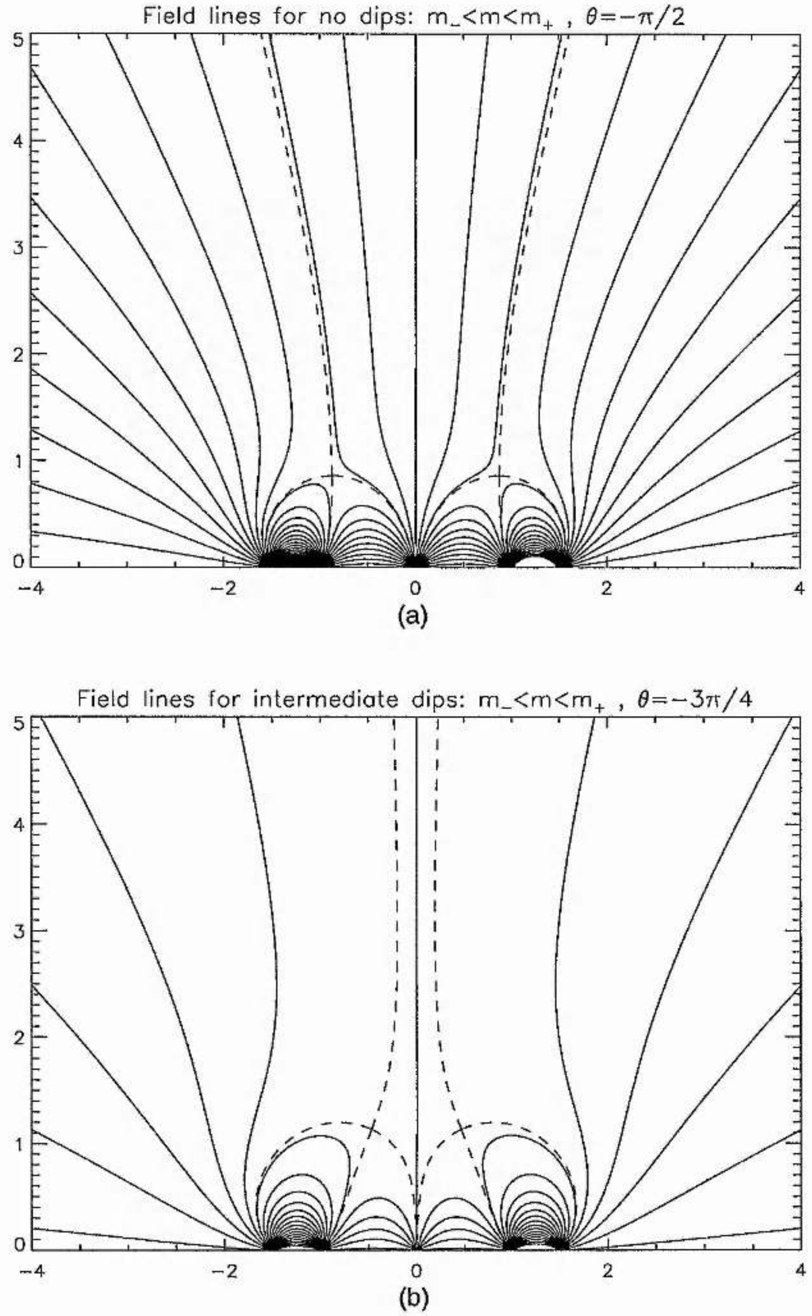

Figure 5.6: Field line plots for the symmetric case with five charges showing the various topologies as the bipolar strength is increased.

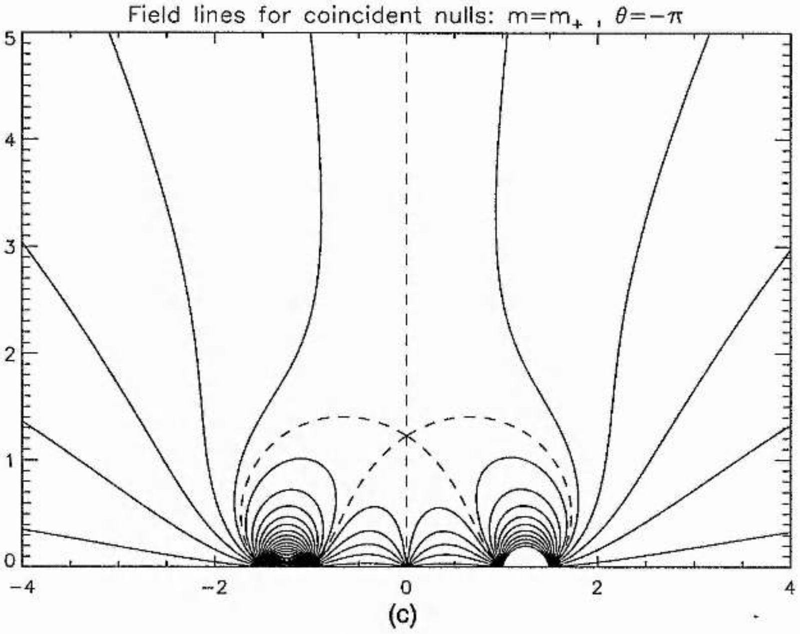

Figure 5.6c

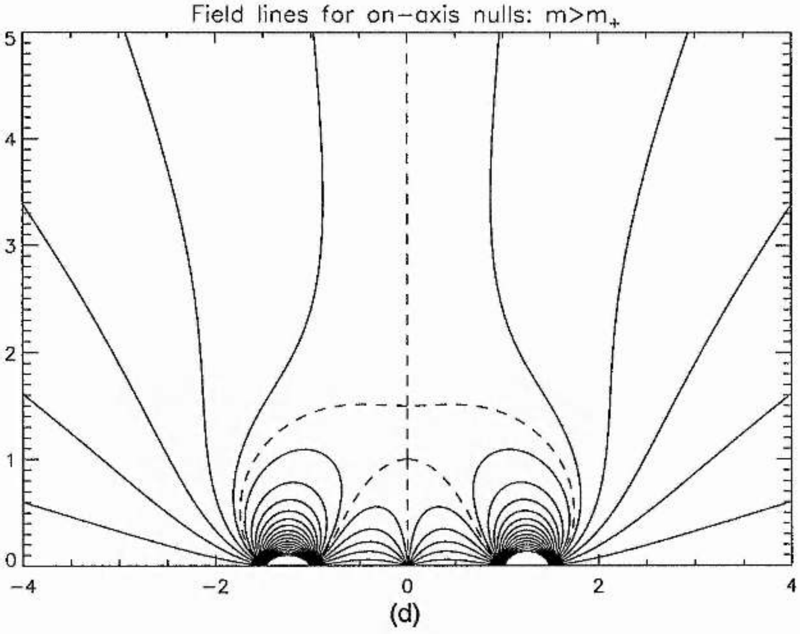

Figure 5.6d

$\theta = -\pi$. Here the behaviour is different to the three-source case, because at this point the two nulls in the upper-half plane have coalesced (coincident nulls). As m is increased further ($m > m_+$), the nulls again separate and move along the y-axis where they possess the "+ - type" orientation.

Figure 5.6 shows various stages in this evolution for $x_0 = 1.5$ and $y > 0$ including (a) $\theta = -\pi/2$ (no dips), (b) $\theta = -3\pi/4$ (intermediate dips), (c) $\theta = -\pi$ (maximum dips; coincident nulls) and finally (d) $m > m_+$, the case of on-axis nulls.

5.4.2 Comments on the Five-Source Distribution

For the case of five charges, it is clearly seen from the field line plots that the behaviour of the polar field is more realistic, with a vertical polar field line as required. Figure 5.5 indicates, for the observed ranges of the parameters, that the best chance of attaining good dips is for θ to lie in the range $-\pi \leq \theta \ll -\pi/2$. Maximum dips occur for $m = m_+$ (Figure 5.6c) but this would imply a prominence forming at the pole which is not observed. Thus, the most likely possibility is a plot similar to Figure 5.6b. The dips are still sufficient to allow some prominence material to collect, and we could assume that this dip will deepen as the material continues to condense. There are problems though, concerning both the structure of the polar field and the technical construction of current sheet prominence solutions from this configuration. The former point arises due to the orientation of the separatrices above the nulls. This causes the polar field to be squeezed inwards, contrary to the usual observation that the polar field expands with height. This may be a consequence of our Cartesian geometry but more likely it is a physical effect that needs to be included in the model. Such an effect is incorporated in the next section. The technical problem occurs in the second quadrant. For the formation of prominence sheets an asymmetry is introduced at the stage where we impose a horizontal field component at infinity. This will cause the current sheet in the second quadrant to have a bad orientation so that when the counter horizontal field is applied, this sheet will either be subject to a downward Lorentz force or will have a very flat orientation, which is equally undesirable. Also, when the counter field is applied, the polar field will become non-vertical, thus discounting the possibility of forming a full solution by reflection of the first quadrant in the y-axis. Possibly, a more sophisticated method, e.g. a conformal mapping, would yield the desired solution - a possibility certainly worth consideration.

The next section develops the ideas further by using finite sources of photospheric flux. It is an asymmetric distribution, but the effect of the solar wind is included which has the advantage of allowing a vertical polar field plus a more realistic field structure.

5.5 Finite Sources and Effect of Solar Wind

In this section we use finite regions of photospheric flux to give a better representation of the surface field distribution. Figure 5.7 illustrates the considered distribution and shows the notation and parameters we adopt. The polar flux is confined to the domain $[-x_1, x_1]$ and has unit strength while the bipolar flux is given by two unequal regions $[x_2, x_3]$ and $[x_3, x_4]$ of strength $\mp B_b$, respectively. Thus, the bipolar field strength has been normalised to the polar value given by $B_p \approx 10\ G$. Notice that this gives rise to two polarity inversion lines located at x_{N1} , where $x_1 < x_{N1} < x_2$, and another at $x_{N2} = x_3$. All lengths have been normalised to the radius of the Sun ($R_\odot \approx 700\ Mm$) and so the equator is located at $x = \pi/2$.

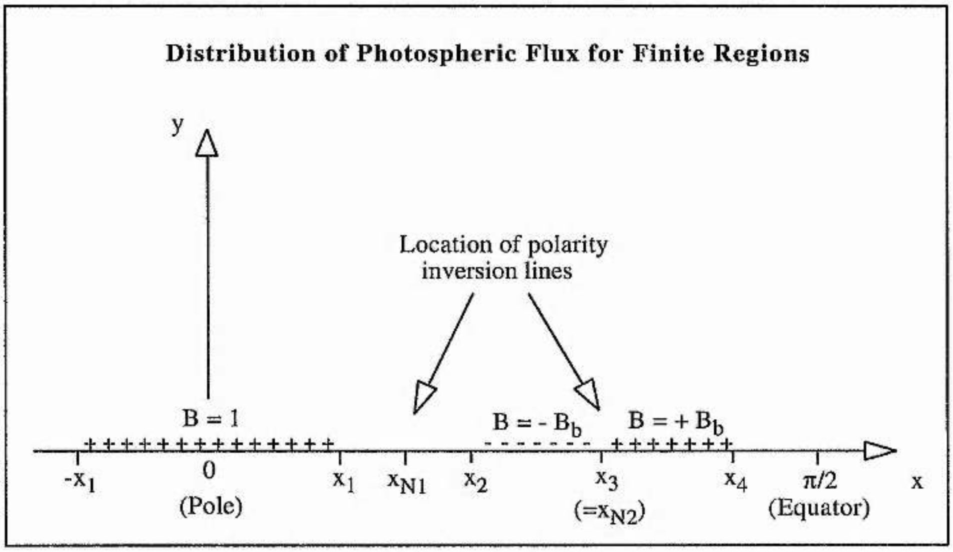

Figure 5.7: The distribution of flux for finite regions showing the notation used.

The purely potential field may be expressed as

$$B(w) = \frac{i}{\pi} \ln\left[\frac{w + x_1}{w - x_1}\right] + B_b \frac{i}{\pi} \ln\left[\frac{(w - x_3)^2}{(w - x_2)(w - x_4)}\right] \ . \tag{5.8}$$

As $w \to \infty$, the behaviour of this field is given by

$$B \sim \frac{2i\ x_1}{\pi w} + \frac{i\ B_b}{\pi w}\ (x_2 - 2x_3 + x_4)\ , \tag{5.9}$$

which is equivalent to the field generated by a point source of strength $2x_1 + B_b(x_2 - 2x_3 + x_4)$ located at the origin. Thus, the field lines become radial at large distances.

5.5.1 Observed Parameter Ranges

Observational data fixes or constrains some of the parameter values as follows. As stated in Section 5.3.4, the flux ratio is given by

$$2x_1 \leq (x_3 - x_2)\ B_b \leq 10x_1\ .$$

The value of x_1 , which approximately defines the boundary of the polar coronal hole, is taken to be 0.3 . Also, the two polarity inversion lines are generally located within the ranges

$$0.6 < x_{N1} < 0.9 \quad \text{and} \quad 1.0 < x_{N2} = x_3 < 1.2\ .$$

At this stage, it is useful to write the parameters in terms of normalised fluxes, i.e.

$$F_1^* = \frac{(x_3 - x_2)\ B_b}{x_1} \quad ; \quad F_2^* = \frac{(x_4 - x_3)\ B_b}{x_1}\ , \tag{5.10}$$

so there are four free parameters: x_2 ; x_3 ; F_1^* and F_2^* , subject to the conditions

$$2 \leq F_1^* \leq 10 \tag{5.11}$$

$$x_{N1} < x_2 < x_3 \tag{5.12}$$

$$x_3 < x_4 = x_3 + \frac{F_2^*}{F_1^*}(x_3 - x_2) < \frac{\pi}{2}\ (\text{equator})\ . \tag{5.13}$$

5.5.2 Influence of the Solar Wind

The purely potential field (5.8) is a good approximation to the observed field for small values of w, but as $w \to \infty$ the field lines become radial. Observations, however, (for example, eclipse photographs) show that the actual field becomes stretched out at a height comparable to the solar radius above the surface . Although our model does not include a circular photospheric boundary (a possibility for future modification), we can incorporate the effect of this stretching by requiring that the field is vertical at a given height (i.e. radial in spherical geometry). The modified field

$$\begin{aligned} B(w) &= \frac{i}{\pi}\ln\left(\frac{\tanh\frac{\pi}{4}(w+x_1)}{\tanh\frac{\pi}{4}(w-x_1)}\right) \\ &+ B_b\frac{i}{\pi}\ln\left(\frac{\tanh^2\frac{\pi}{4}(w-x_3)}{\tanh\frac{\pi}{4}(w-x_2)\,\tanh\frac{\pi}{4}(w-x_4)}\right) \quad y<1\ , \end{aligned} \tag{5.14}$$

possesses such behaviour, since the horizontal component tends to zero as $y \to 1$. For this field the neutral point (in $y > 0$) needs to be computed numerically and the height of the null must lie in the range

$$0.05 \leq y_N \leq 0.15\ ,$$

for prominence applications.

5.5.3 Possible Pre-Prominence Solutions

Despite the restrictions (5.11-5.13) on some of the values, we still have four free parameters to consider. Keeping x_3 free allows us to examine solutions for various positions of the second polarity inversion line (at $x = x_{N2}$). Let us also keep F_2^* free and consider the behaviour of the field for $x_2 = 1.0$ and $F_1^* = 2.0$.

Solutions for $F_1^* = 2.0$ and $x_2 = 1.0$

Relevant pre-prominence solutions may be selected when the null is

(i) at a height of $y_N = 0.1$, say,
(ii) located approximately above a polarity inversion line, and
(iii) well orientated, such that field line dips are present.

Figure 5.8a shows the parameter values for which (i) is satisfied. Solutions for $x_3 < 1.06$ are neglected as this results in the value of B_b exceeding 10 which is too large. Any given

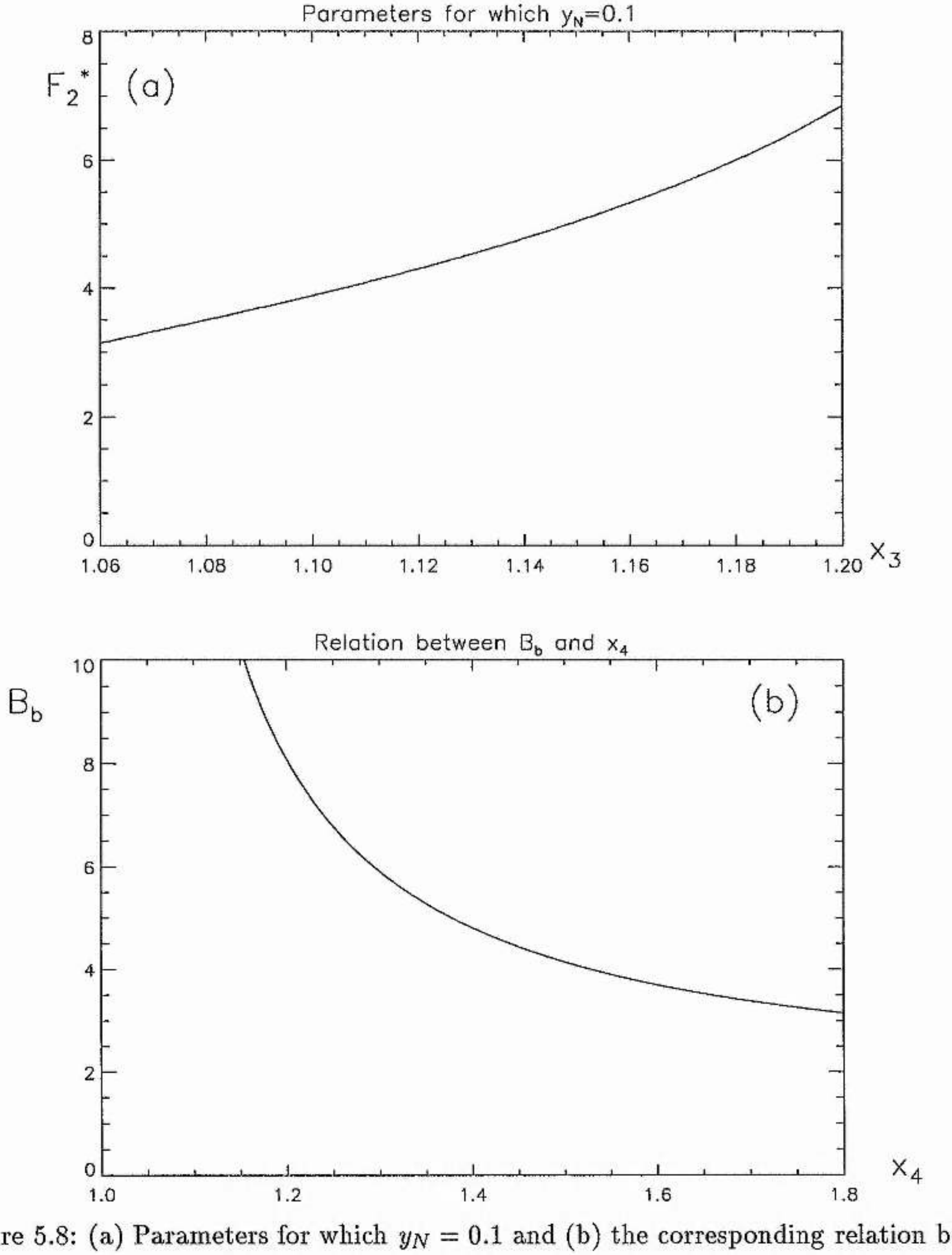

Figure 5.8: (a) Parameters for which $y_N = 0.1$ and (b) the corresponding relation between B_b and x_4.

point along this curve determines both B_b and x_4 , from (5.10), and so the relation between B_b and x_4 for which $y_N = 0.1$ is shown in Figure 5.8b. As x_3 increases, B_b drops (to ensure $F_1^* = 2$) and F_2^* increases (to prevent the null from rising). These effects all imply that x_4

must increase so that the total size of the bipolar region is enlarged.

Figure 5.9 (a, b, c) shows various configurations as x_3 is increased. The values of B_b are respectively 8, 6 and 4 in these plots. It can be seen that there is good polar field structure in all three plots - the field is almost vertical at the pole and the width of the coronal hole increases with height as observed. There is slightly more distortion to the

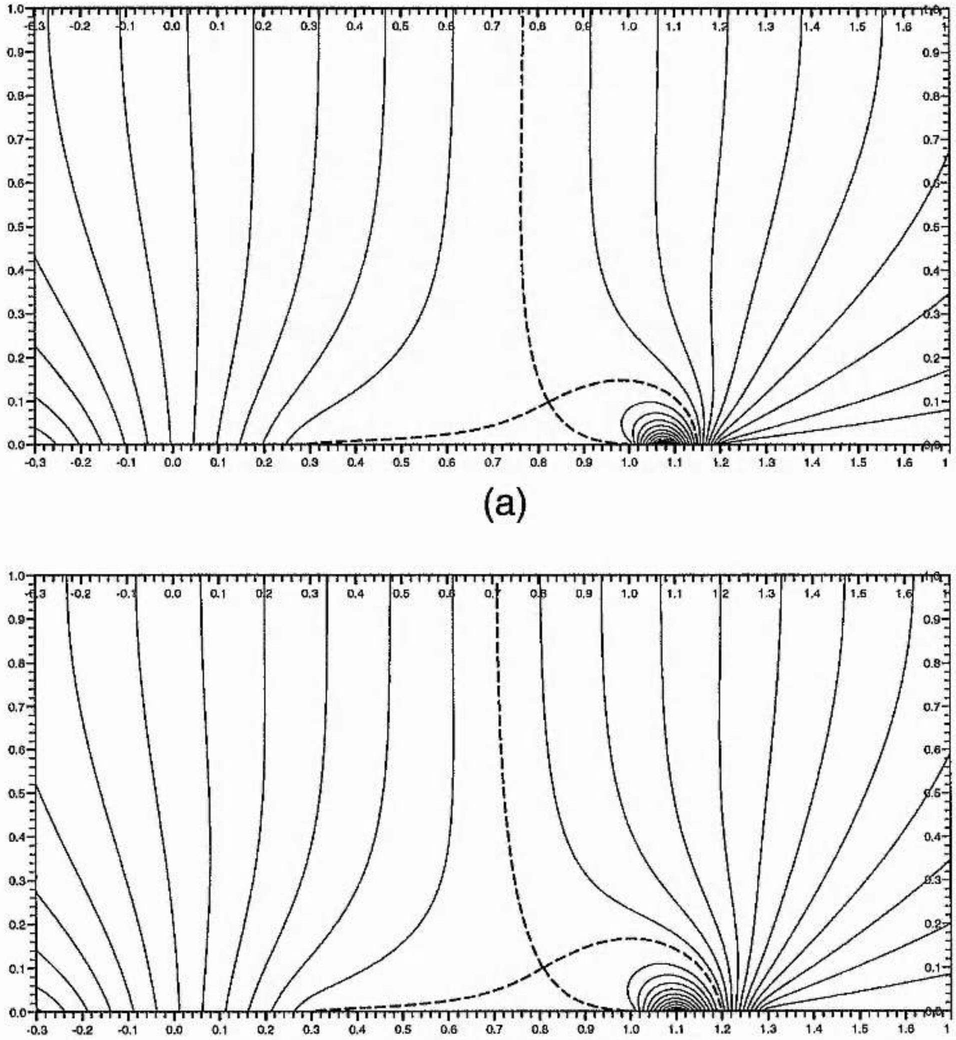

Figure 5.9: Field lines for finite sources. (a)-(c) demonstrates the effect of increasing x_3 in accordance with the requirements of Section 5.5.3. (d) shows the purely potential field (without the wind effect) for comparison.

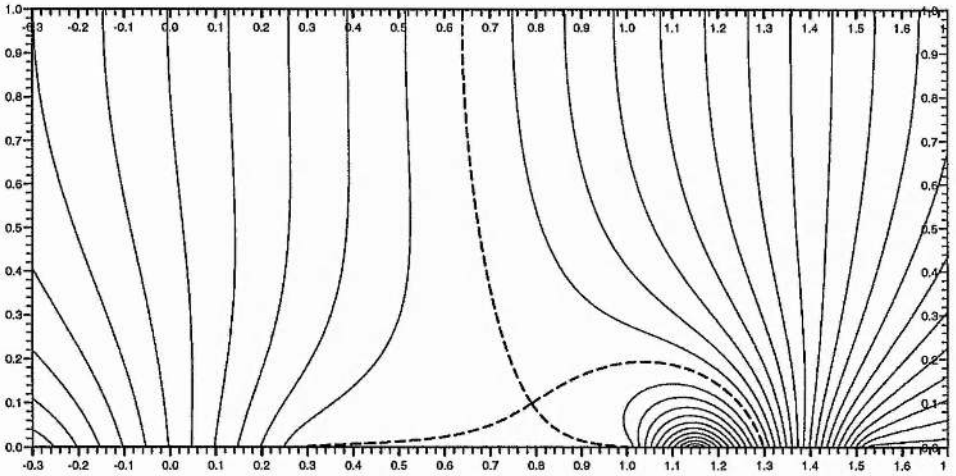

(c)

Figure 5.9c

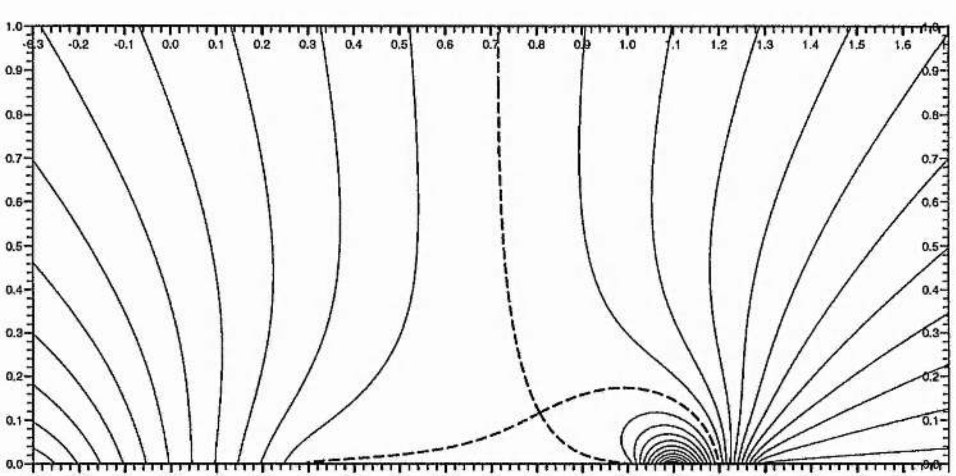

(d)

Figure 5.9d

polar field as x_3 is increased, e.g. Figure 5.9c, but even here the field structure seems reasonable. Good dips are apparent in all three cases. This is due to the low value of y_N (maximum dips occur as the null hits the photosphere). Also, the null overlies the polarity inversion line at $x = x_{N1}$ and so this is certainly a possible location for a prominence to develop. For comparison, Figure 5.9d shows the field for the purely potential case without the effect of the solar wind. The parameters are the same as for Figure 5.9b but it can be seen that, although locally the two configurations are similar, there is poor behaviour at large distances where the field becomes radial. A consequence of this is that the polar field is particularly distorted and so we must conclude that the effect of the solar wind is certainly important in retaining the basic overall structure of the field there.

5.5.4 Evolution of the Field

Finally, it is interesting to consider a possible development of the field prior to the pre-prominence configuration, as the bipolar region moves towards and pushes against the open polar field. Figure 5.10 shows a sequence of plots for different locations of the bipolar region. Throughout the evolution the width and strength of this region is kept fixed, although, in reality, these parameters will probably vary slightly.

Initially (Figure 5.10a), there is a case of on-axis nulls which converge as the bipolar field approaches the pole. After some time, they coalesce (Figure 5.10b) and further evolution causes the null to rise (due to reconnection of the field lines) into the correct pre-prominence location (Figure 5.10c). As this reconnection takes place, the rising field lines may transport dense photospheric/chromospheric material up into the corona giving rise to a slow flow associated with the field as it progresses through a series of quasi-static equilibria. Such a mechanism has been proposed by Titov et al. (1993) and Priest and VanBallegooijen (1995). This provides an alternative mechanism for the formation of the prominence.

Of course, this is only one possible evolution scenario. The final field may be a consequence of several effects, such as variations in the strengths or the sizes of the sources (we have taken the bipolar region to be of uniform strength), newly emerging flux, submerging flux, or possibly a combination of various effects.

5.5.5 Comments on the Finite-Region Distribution

Although we have not made an exhaustive study of this problem, we have shown for certain parameter values that it is possible to achieve a polar-crown configuration that fits reasonably well with the observations. The solutions we obtain are scaled to the correct dimensions and include a neutral point with dips at a height of $y_N = 0.1$, which corresponds to an actual height of $70Mm$. The field is stretched out by the solar wind so that it is

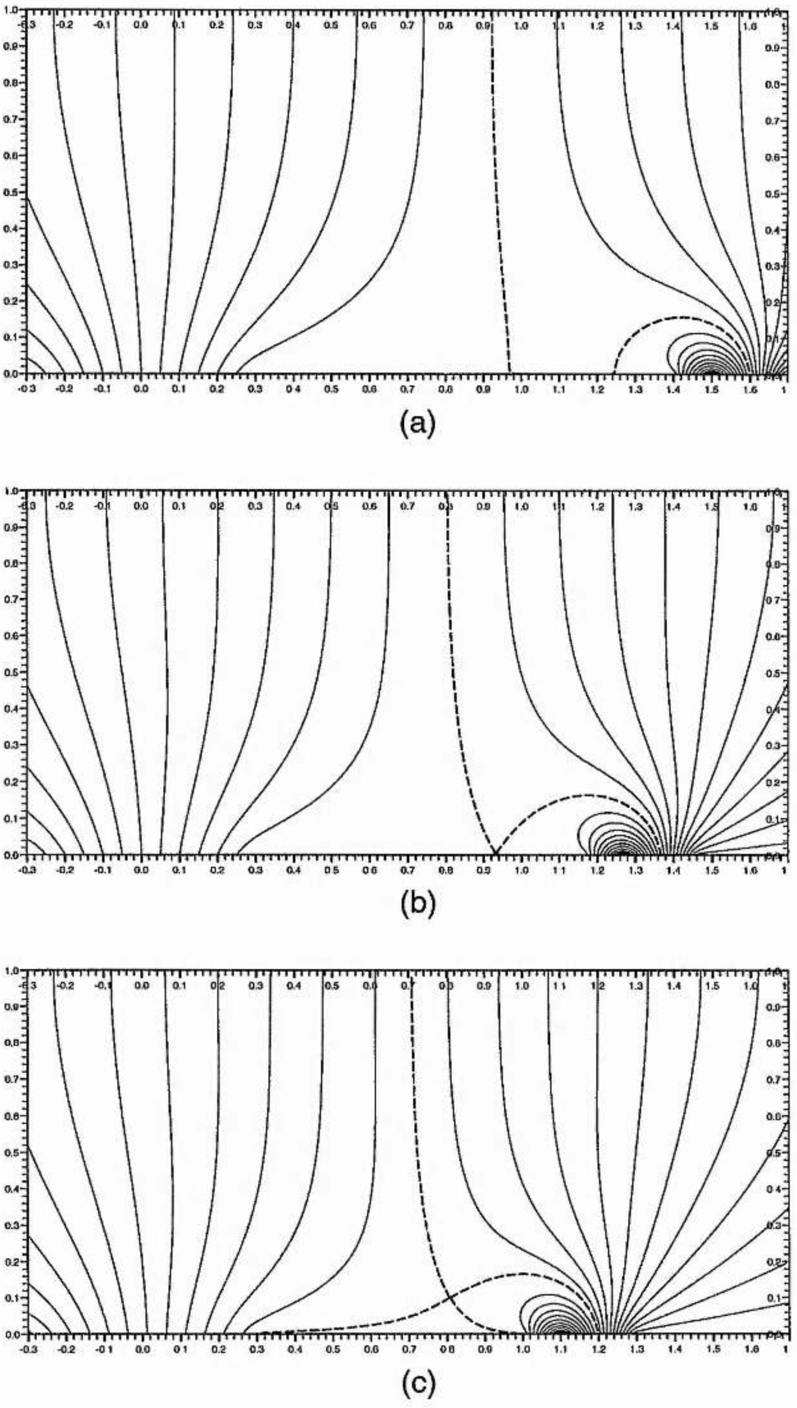

Figure 5.10: A possible evolution sequence of the field to the final pre-prominence configuration

vertical at a height of one solar radius, and this has the effect of maintaining a well developed field structure with a near-vertical polar field line. The dips are naturally located above a polarity inversion line, a necessary condition for prominence formation.

5.6 Discussion

In this chapter, we have made an extensive study using various distributions of flux to generate potential polar-crown field configurations which possess suitable sites for prominence formation. Anzer (1994) has briefly addressed this problem but in his analysis, which was less thorough, he was unable to find acceptable solutions with a location of dipped magnetic field.

The models presented here use distinct regions or sources of photospheric flux and so are more realistic than the original model of Chapter 4 in which an infinite domain of flux was used. It is found that a simple distribution of three charges (necessary to generate an inverse-polarity prominence topology at the pole) is not sufficient to obtain the requisite features. For observed values of flux, field line dips are possible but the polar field is completely disrupted by the relatively high strength of the bipolar field. Using a symmetric distribution of five charges avoids this problem and allows a vertical field line at the pole (for the pre-prominence field, at least), but for good dips the nulls are too close to the pole, resulting in a compression of the polar field with height. A distribution of finite-flux regions presents similar problems: the asymmetric case causes a non-vertical polar field, but this may be resolved when the effect of the solar wind is incorporated so that the field becomes stretched in the vertical direction.

In order to construct final prominence equilibria from these configurations we may use the general method of Titov (1992) which requires the photospheric flux distribution to be known. For the cases where charges are used, fully analytical current sheet solutions are possible. However, for the five-charge distribution, the formation of two current sheets will result, and as the horizontal field component is applied, the symmetry is lost and one of the sheets will either be very flat or subject to a downward Lorentz force. The distribution of finite sources results in a numerical solution, but in theory a well-behaved final prominence sheet equilibrium is possible, with the effect of the solar wind included.

There are still some weaknesses in the model, however. In reality, large variations in three dimensions are present, and observations indicate a high degree of shear at the prominence location (e.g. Tandberg-Hanssen and Anzer (1970); Leroy et al. (1983); Kim (1990); Martin (1990)) so the potential field assumption used here may not be so realistic, although uniform shear may still be artificially superimposed. In this model, there are two polarity inversion lines present, yet it is not possible to obtain neutral points with dips above both from these calculations. Observations, though, indicate that prominence formation can occur at both of these locations. In addition, a spherical geometry should be used as the effect of the curvature of the Sun's surface is certainly important over these length scales.

In spite of these points, the analysis presented here does at least give an approximate indication of possible large-scale flux distributions which are required for prominence formation to occur within the polar-crown magnetic field. In particular, the distributions of Section 5.5 give a reasonable approximation, rectifying Anzer's model to some extent, and hence providing the basis to construct a modified polar-crown prominence equilibrium.

Chapter 6

The Internal Structure of a Curved Prominence Sheet

6.1 Chapter Summary

In the previous two chapters, magnetic configurations associated with a curved prominence sheet have been considered. In such a solution, the prominence is represented by a discrete sheet of mass and current, and so no information about the internal structure is available.

In this chapter, a one-dimensional internal analysis of Kippenhahn-Schlüter type is applied to a sheet of prominence material inclined at an angle θ to the horizontal. It is found that the magnetic pressure across the prominence no longer has a symmetric profile, but is stronger on the lower side of the sheet. The excess in magnetic pressure there is necessary to balance the component of prominence weight in that direction. A matching function is derived and allows for variations along the length of the sheet, enabling the internal prominence solution to be linked onto a given background potential field. In this way a curved prominence sheet in a potential field may be resolved. A smooth profile for the magnetic field and a continuous variation of plasma pressure across the prominence region is then possible. This analysis is applied to the polar-crown prominence model of Chapter 4 to obtain a matched internal and external solution in which the basic properties of the prominence are determined.

6.2 Introduction

Solutions to the magnetohydrostatic equation have been investigated by many authors (see Chapter 2 for a short review) to gain information about the internal prominence properties such as pressure, density and temperature. One of the classic approaches is that of Kippenhahn and Schlüter (1957) in which a simple isothermal solution for a vertically oriented prominence sheet was found by assuming that the horizontal components (both normal and axial) of the field are constant and that the vertical component and the plasma pressure vary only in the normal direction. Appropriate boundary conditions lead to solutions in which the magnetic field has a dipped structure, providing support, and a distribution of pressure, and hence density, that rises from zero outside the prominence to a maximum at the prominence centre. Hood and Anzer (1990) extended this theory by finding a class of two-dimensional, cool internal solutions that match smoothly onto a hot background coronal arcade.

All of these models, however, have all been applied to straight, vertical prominence sheets, but it is one of the objectives of this chapter to demonstrate how a similar analysis may be applied to slanted material, with a view to generalising further to the equilibrium of a curved prominence.

This chapter is set out as follows. In Section 6.3, the basic equations are introduced for the interior region of a prominence sheet inclined at an angle θ to the horizontal. The retrieval of the original Kippenhahn-Schlüter (K-S) solutions for a vertical sheet is demonstrated, and a comparison of the two sets of results given. In Section 6.4, the model for a polar crown prominence proposed in Chapter 4 is considered. By using a matching function technique, the theory of Section 6.3 is applied so that the interior structure of the prominence may be included in the model. It is worth clarifying here that, although a K-S analysis is applied locally in the prominence region, the global magnetic field of the prominence retains its inverse (Kuperus-Raadu) type polarity. Results of this analysis are presented and a discussion is given in the final section.

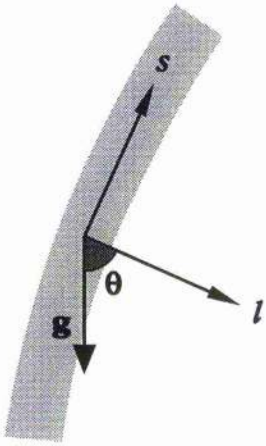

Figure 6.1: The local coordinate system for a sheet of material inclined at an angle θ to the horizontal.

6.3 Equilibrium of a Slanted Prominence Sheet

6.3.1 Basic Equations

We here consider an isothermal plasma at rest in the presence of a magnetic field and under the influence of a constant gravitational field, $\mathbf{g}$, so the magnetohydrostatic equations may be applied:

$$-\nabla p + \mathbf{j} \times \mathbf{B} + \rho \mathbf{g} = \mathbf{0} \ , \tag{6.1}$$

$$\nabla \cdot \mathbf{B} = 0 \ , \tag{6.2}$$

and for a fully ionised hydrogen gas,

$$p = \frac{\rho R T}{\tilde{\mu}} = \rho g H \ , \tag{6.3}$$

where H is the gravitational scale height.

A local system of coordinates is used in which we consider a sheet of plasma at an angle θ to the horizontal as shown in Figure 6.1. Variations in the $\hat{\mathbf{z}}$-direction are ignored.

If the normal and axial components of the magnetic field, B_n and B_z, respectively, are constant and the transverse gradients of the other values in the sheet are much greater than the longitudinal ones, i.e. $\partial/\partial l \gg \partial/\partial s$, then these values depend on l as a parameter and (6.1) may be written as follows:

$$\frac{d}{dl}\left(p+\frac{B_\tau^2}{2\mu_0}\right)=\frac{p}{H}\cos\theta \tag{6.4}$$

$$\frac{B_n}{\mu_0}\frac{dB_\tau}{dl}=\frac{p}{H}\sin\theta \tag{6.5}$$

where $B_\tau(l)$ and $p(l)$ are the local values of the tangential magnetic field component and the plasma pressure, respectively.

Also, the magnetic field,

$$\mathbf{B}=(B_n, B_\tau(l), B_z)$$

satisfies equation (6.2).

6.3.2 Analytical Solution

Dividing (6.4) by (6.5) we obtain

$$\frac{d}{dB_\tau}\left(p+\frac{B_\tau^2}{2\mu_0}\right)=\frac{B_n}{\mu_0}\cot\theta \tag{6.6}$$

from which it follows that

$$p=-\frac{B_\tau^2-B_{\tau L}^2}{2\mu_0}+\frac{B_n}{\mu_0}\cot\theta\,(B_\tau-B_{\tau L})\ . \tag{6.7}$$

Here we have taken into account that, if $l\to-\infty$, $p\to 0$ and $B_\tau\to B_{\tau L}$. Also, if we require that as $l\to+\infty$, $p\to 0$ and $B_\tau\to B_{\tau R}$ we obtain from (6.7)

$$2B_n\cot\theta=B_{\tau L}+B_{\tau R}\ . \tag{6.8}$$

It is useful when solving (6.5) and substituting for p to rewrite (6.7) as

$$p=\frac{1}{2\mu_0}\left[\frac{1}{4}(B_{\tau R}-B_{\tau L})^2-\left(B_\tau-\frac{B_{\tau R}+B_{\tau L}}{2}\right)^2\right]\ ,$$

so that we obtain

$$B_\tau = \frac{B_{\tau R} + B_{\tau L}}{2} + \frac{B_{\tau R} - B_{\tau L}}{2} \tanh\left[\frac{(B_{\tau R} - B_{\tau L})\cos\theta}{2(B_{\tau R} + B_{\tau L})H} l\right] . \tag{6.9}$$

Consider the prominence field to be the superposition of two fields: (a) the field due to a neutral current sheet that contains no mass but finite current in the axial direction; this field tends to a constant value of $\mp B_{\rm sh}\ \hat{\mathbf{s}}$ as $l \to \pm\infty$ and $p \to 0$; and (b) a uniform horizontal field, $-B_{x0}\ \hat{\mathbf{x}}$, which is the component of the field that contributes to the upwards Lorentz force on the sheet, thus providing the support of dense material. Then we have

$$B_{\tau L} = B_{\rm sh} - B_{x0}\ \cos\theta\ ,$$

$$B_{\tau R} = -B_{\rm sh} - B_{x0}\ \cos\theta\ ,$$

and

$$B_n = -B_{x0}\ \sin\theta\ .$$

Substituting these expressions into (6.9), we obtain

$$B_\tau = -B_{x0}\ \cos\theta - B_{\rm sh}\ \tanh\left(\frac{B_{\rm sh}\ l}{2B_{x0}\ H}\right) . \tag{6.10}$$

Also, from (6.7)

$$p = \frac{B_{\rm sh}^2}{2\mu_0}\ \cosh^{-2}\left(\frac{B_{\rm sh}\ l}{2B_{x0}\ H}\right) . \tag{6.11}$$

Note that we are considering here a straight slanted element of sheet so that $B_{\rm sh}$ is a constant, but we shall show in Section 6.4 how this may be adapted to allow for a more general curved sheet.

6.3.3 Retrieval of the Kippenhahn-Schlüter Solution

The original K-S solution corresponding to a vertical sheet may be obtained from equations (6.10) and (6.11) by setting

$$\theta = 90^\circ\ ,\ B_{\rm sh} = B_{y0}\ ,\ l = x\ ,\ B_\tau = B_y\ ,$$

and so we have

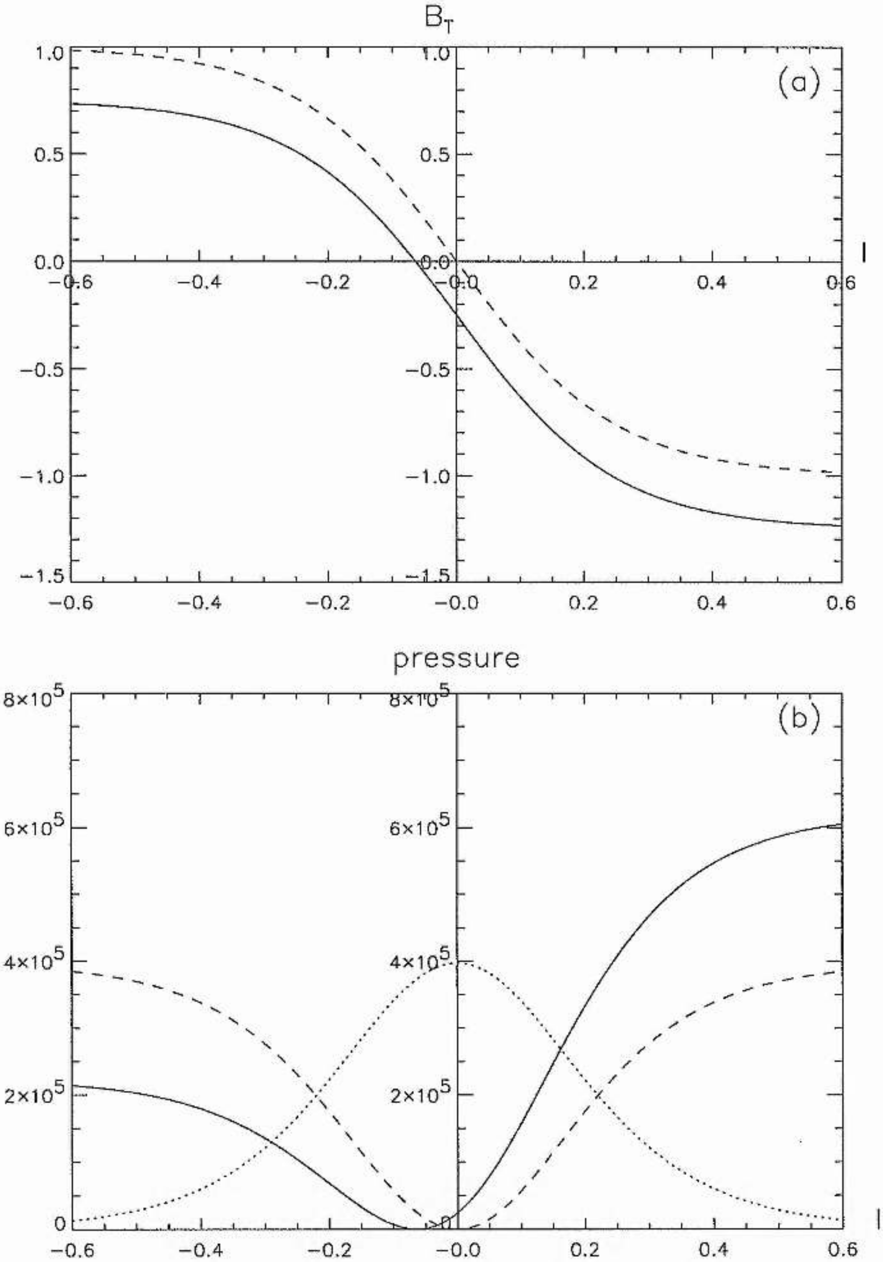

Figure 6.2: (a) The variation of B_τ across the sheet for a vertical (K-S) sheet (dashed) and a sheet inclined at an angle 60° to the horizontal (solid). (b) The variation of plasma pressure (dotted), and magnetic pressure for vertical (dashed) and slanted (solid) cases. Parameter values used are $B_{\rm sh} = 1.0$, $B_{x0} = 0.5$, $H = 0.25$.

$$B_y = -B_{y0} \tanh\left(\frac{B_{y0}\, x}{2B_{x0}\, H}\right) ,$$

with

$$p = \frac{B_{y0}^2}{2\mu_0} \cosh^{-2}\left(\frac{B_{y0}\, x}{2B_{x0}\, H}\right) .$$

6.3.4 Comparison of Results

It is useful, at this stage to make a comparison of the results of the vertical and slanted cases. Figure 6.2a shows the variation of B_τ in the normal direction and it can be seen that, for the slanted case (solid curve), this is no longer a symmetric profile. Figure 6.2b neatly illustrates the balance of forces between the magnetic and plasma pressure gradients. For the vertical case, the magnetic pressure exerts a force towards the centre of the sheet equally from both sides. The role of this force is simply to confine the plasma by balancing the outwardly directed plasma pressure gradient. The magnetic pressure at the edge of the sheet ($p = 0$) thus takes the same value as the plasma pressure at the centre of the sheet, i.e. $B_{\rm sh}^2/2\mu_0$. For the slanted case, however, there is an excess in magnetic pressure on the lower ($l > 0$) side of the sheet. This is necessary as there is now a component of weight in this direction, and so the excess is required for supporting the additional weight of the plasma.

These points are illustrated in the governing equations. If we rewrite equation (6.4) as follows

$$p + \frac{B_\tau^2}{2\mu_0} = g\cos\theta \int_{-\infty}^{l} \rho(l)\, dl + \text{const} ,$$

and integrate using the boundary condition as $l \to -\infty$, we obtain

$$p + \frac{B_\tau^2 - B_{\tau L}^2}{2\mu_0} = m(l)\, g\cos\theta . \tag{6.12}$$

Similarly, (6.5) gives

$$\frac{B_n[B_\tau]}{\mu_0} = m(l)\, g\sin\theta . \tag{6.13}$$

where $m(-\infty) = 0$ and $m(+\infty) = M$, the mass per unit area of the sheet. $[B_\tau]$ is the jump in B_τ across the region of integration, i.e.

$$[B_\tau] = B_\tau - B_{\tau L} \ .$$

Equation (6.12) gives the force balance in the normal ($\hat{\mathbf{l}}$) direction and highlights the relation between these forces. The magnetic pressure force acts inwards towards the point l_c given by

$$l_c = -\frac{2B_{x0}\ H}{B_{\rm sh}} \ \mathrm{arctanh}\left(\frac{B_{x0}}{B_{\rm sh}}\cos\theta\right) \ ,$$

and is the position at which the forces due to plasma pressure and gravity cancel. For $l < l_c$, the plasma pressure gradient dominates the weight and so the magnetic pressure force must act in the positive $\hat{\mathbf{l}}$-direction. For $l > l_c$, the reverse is true. This effect is illustrated in Figure 6.2b. In the tangential direction, the effects of force balance, given by equation (6.13), are basically the same as in the vertical case, in which the tension in the field lines is required to balance the component of weight in this direction. Of course, for the vertical case, it is the resultant prominence weight which acts in this direction.

Plots of the magnetic field lines are shown in Figure 6.3. The enhanced magnetic pressure on the lower side of the sheet can be clearly seen for the slanted cases. Figures 6.3a and 6.3b show the field lines through the prominence region for the vertical and slanted cases, respectively, and a value of $H = 0.25$. The prominence half-width may be defined by the value of l at which the plasma pressure has fallen to a fraction α of the central value. Using this definition with $\alpha = 0.5$ we have shaded the prominence region in these figures. Figures 6.3c and 6.3d illustrate the effect as H tends to zero for which the current sheet case is retrieved.

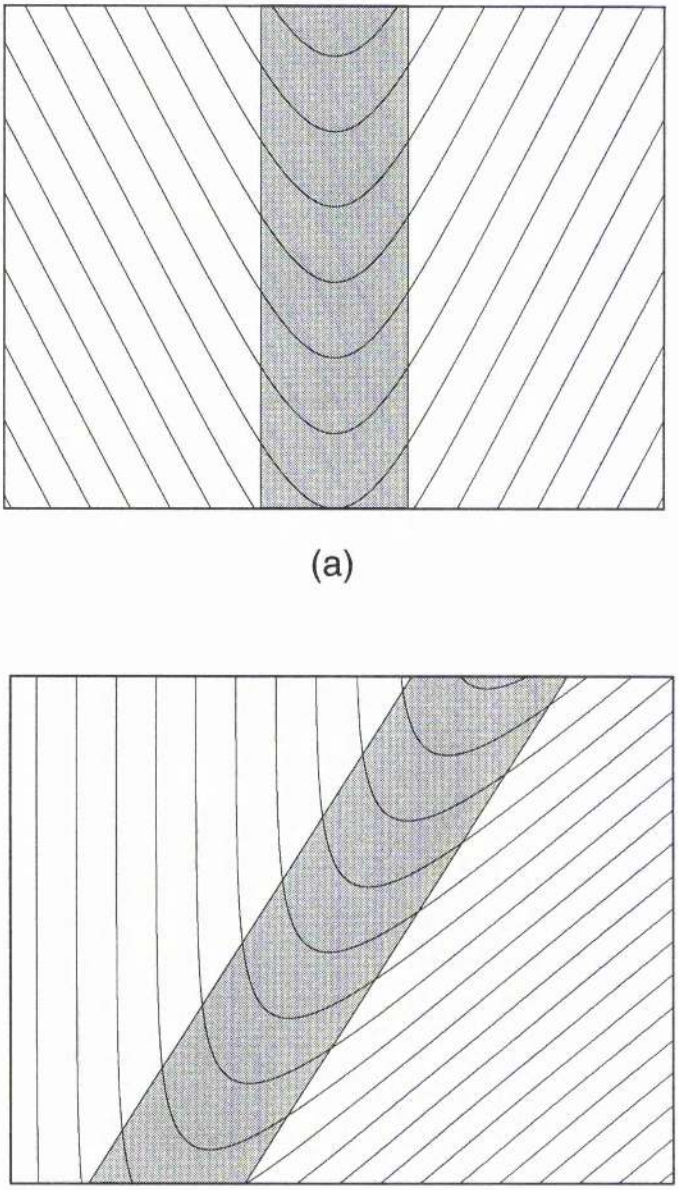

(a)

(b)

Figure 6.3: Field lines through the prominence region for both vertical and slanted cases. (a) and (b) are plotted for $H = 0.5$ and (c) and (d) show the current sheet case, i.e. $H \to 0$.

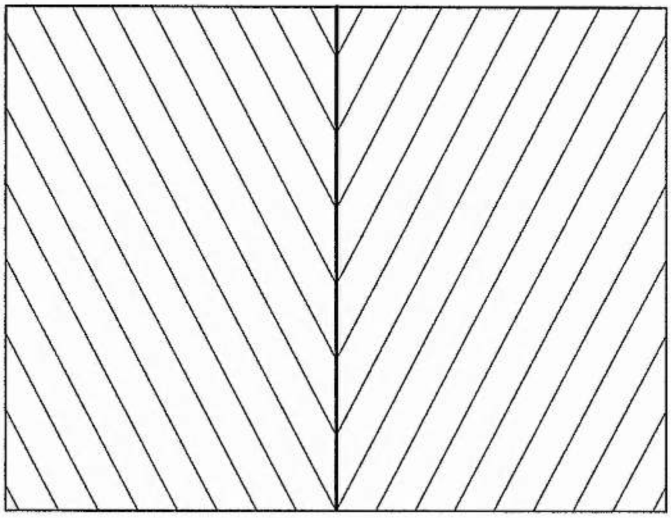

(c)

Figure 6.3c

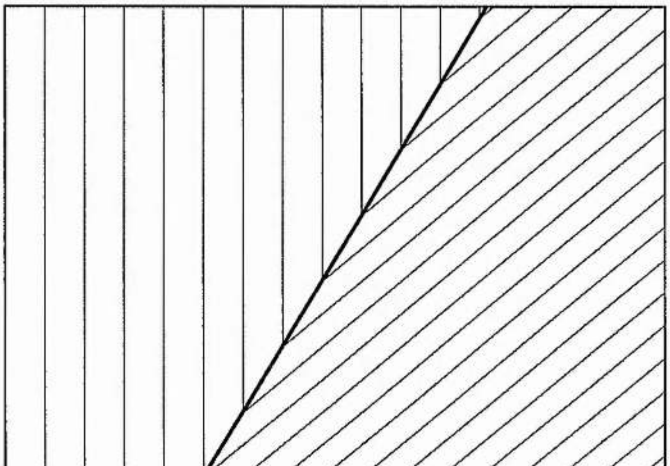

(d)

Figure 6.3d

6.4 Curved Prominence Sheets: Matching the Internal and External Solutions

6.4.1 Applied Example

We now demonstrate how the above internal analysis may be developed to enable this type of prominence solution to be included in a more general magnetic configuration. We consider the model for the polar-crown prominence given in Chapter 4 in which a curved, weighted current sheet is supported in equilibrium in a background potential field.

The resultant field, shown in Figure 4.4a may be decomposed into the sum of two components: the field with a neutral current sheet (no mass), $B_Q(w)$, and a constant horizontal field, $-iB_{x0}$. $B_Q(w)$ is computed using the general method given by Titov (1992) and is shown in Figure 4.3a. The ambient field, $-iB_{x0}$, is superimposed on $B_Q(w)$ and serves two purposes: firstly, to provide weight for the current sheet (thus simulating the dense prominence) by exerting upon it an upwardly directed Lorentz force which must be balanced by gravitational forces; and secondly to achieve a vertical field at large distances, thus representing the open field at the poles of the Sun.

The separation of the two components, $B_Q(w)$ and $-iB_{x0}$, is the key to constructing an appropriate matching function. This allows the internal solution to be linked smoothly onto the external potential configuration.

6.4.2 The Matching Function

The relations (6.10) and (6.11) describe the local behaviour of the magnetic field and pressure inside the prominence sheet. Let us now consider how to construct the relations matching this local behaviour with the global behaviour given by

$$B(w) = B_y + iB_x = B_Q(w) - iB_{x0} \quad ; \quad p = 0 \ . \tag{6.14}$$

For this purpose we need to introduce two new values $l_{\text{sh}}(w)$ and $B_{\text{sh}}(w)$. These values are obtained from the field $B_Q(w)$ by projecting the given point w onto the sheet along the curve which passes perpendicularly through each magnetic field line as shown in Figure 6.4. This projection curve is determined by the following ordinary differential equation:

$$\frac{dw}{dl} = \frac{\bar{B}_Q}{|B_Q|} , \tag{6.15}$$

where $\bar{B}_Q$ is the conjugate of B_Q . We denote the length of this curve by $l_{\rm sh}$. If, for some w, this curve does not intercept the sheet we simply set $l_{\rm sh}(w) \to +\infty$. $B_{\rm sh}(w)$ is defined as the value of the magnetic field at the end of this curve, i.e. at the position of the sheet.

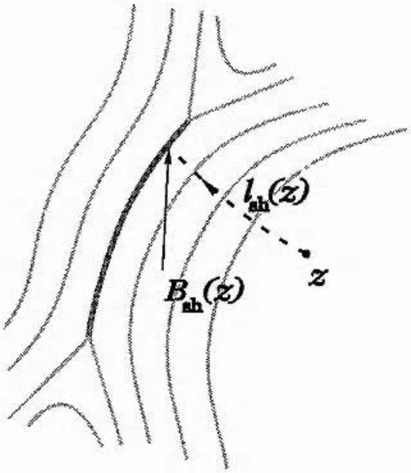

Figure 6.4: The projection of the point w onto the current sheet along the curve defined by orthogonal field lines. $l_{\rm sh}(w)$ is the length of this curve and $B_{\rm sh}(w)$ is the magnetic field at the end of the "projection curve".

Using the concepts of $l_{\rm sh}(w)$ and $B_{\rm sh}(w)$ one can construct the matching function for the magnetic field as

$$\tilde{B}(w) = B_Q(w) \tanh\left(\left|\frac{B_{\rm sh}(w)}{B_{x0}}\right| \frac{l_{\rm sh}(w)}{2H}\right) - iB_{x0} , \tag{6.16}$$

which, for sufficiently small values of H provides a good approximation for both the internal and external magnetic fields in the prominence model.

In a similar way, one can write the matching function for the distribution of pressure in the prominence:

$$p(w) = \frac{|B_{\rm sh}(w)|^2}{2\mu_0} \cosh^{-2}\left(\left|\frac{B_{\rm sh}(w)}{B_{x0}}\right| \frac{l_{\rm sh}(w)}{2H}\right) . \tag{6.17}$$

These functions are both dependent on the positions of the end-points of the sheet. The internal solutions are only significant for $l_{\text{sh}} = \mathrm{O}(H)$ and for $l_{\text{sh}} \gg H$ the potential solution with a current sheet holds.

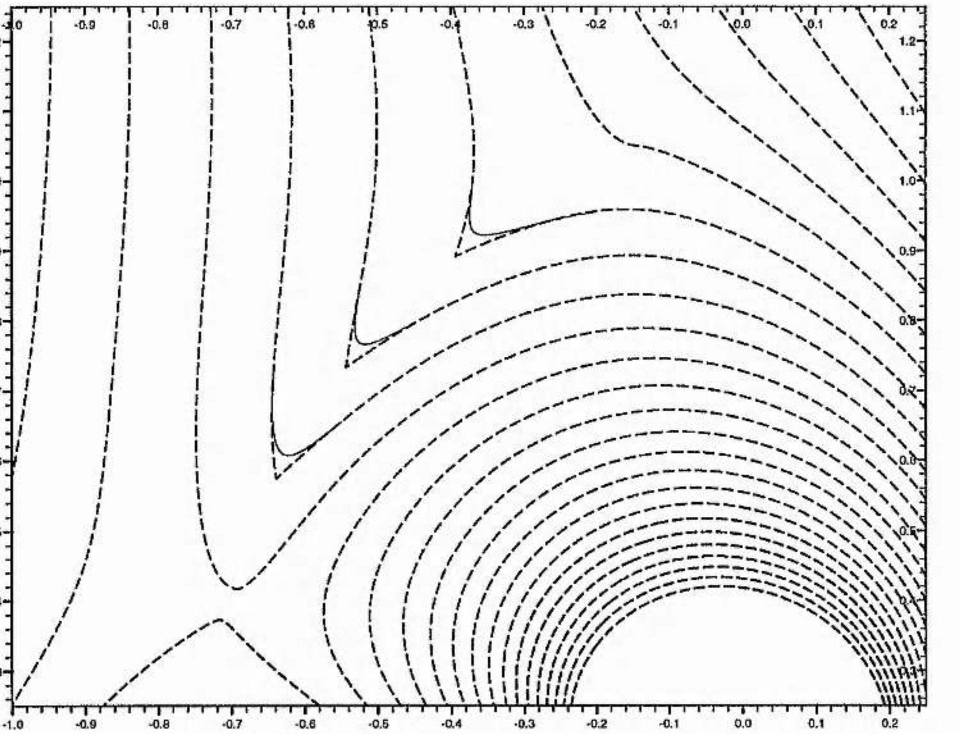

Figure 6.5: The matched field lines through the prominence region.

6.4.3 Main Results

Figure 6.5 depicts the field lines through the interior of the prominence (solid lines) for $H = 0.05$ and shows how these match onto the original potential field (dashed) lines. The discontinuity in the dashed field lines has clearly been replaced by a smooth and continuous profile, as has the pressure distribution which is shown in Figure 6.6a for a cut across the middle part of the sheet. Figure 6.6b shows contours of pressure for a central section of the sheet.

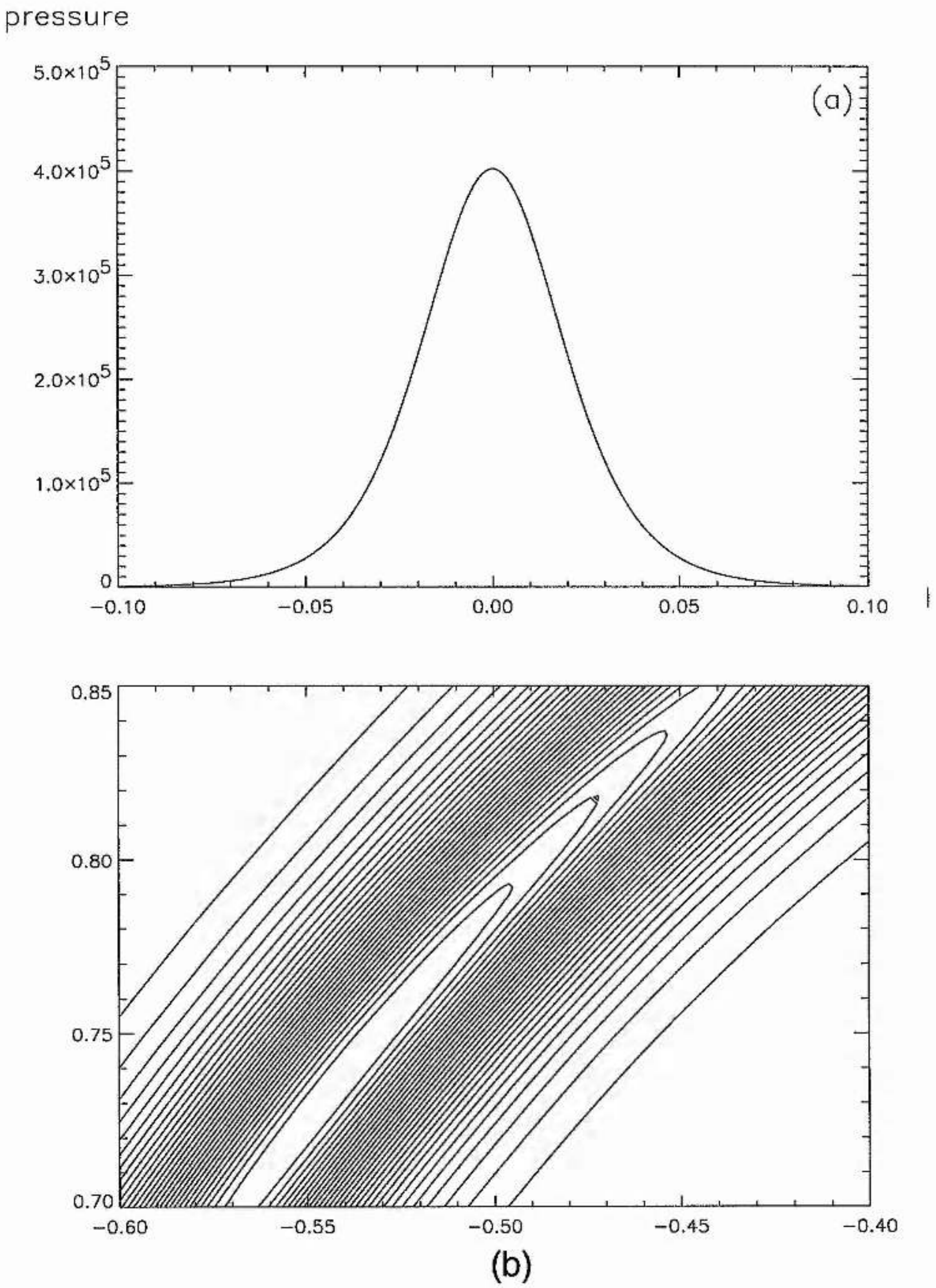

Figure 6.6: The pressure through the interior of the prominence showing (a) the variation along a cut through the middle of the sheet and (b) the contours in the central section of the prominence region.

For the case $H = 0$, the current and mass densities are given by the expressions

$$j_\Sigma(s) = \frac{[B_{\text{sh}}](s)}{\mu_0} \quad \text{and} \quad m_A(s) = \frac{[B_{\text{sh}}](s)B_{x0}}{\mu_0 g} \ ,$$

respectively. Here, $[B_{\text{sh}}] = (B_{\text{sh}})_R - (B_{\text{sh}})_L = 2B_{\text{sh}}$, represents the jump in the value of B_{sh} across the sheet. The variation of $[B_{\text{sh}}]$ is shown in Figure 6.7a, from which we can see that the quantities of mass and current reach a maximum at $s = s_m$. This corresponds to the lower section of the contour map of Figure 6.6b where the pressure, and hence density, reaches a maximum value. If the outer boundary of the prominence is defined by a particular contour of pressure then it can be seen from Figure 6.6b that the prominence cross-section will assume an elongated, curved oval-like shape. At the end-points of the sheet, $B_{\text{sh}} = 0$, and so the pressure and hence the width of the prominence are zero. The variation of the prominence width, defined by the contour

$$p_w = \alpha \frac{B_m^2}{2\mu_0} \quad \text{where} \quad B_m = B_{\text{sh}}\Big|_{l=0, s=s_m} \ ,$$

and $0 < \alpha < 1$ is shown in Figure 6.7b for $\alpha = 0.5$. This has been computed from the expression

$$w(s) = \frac{2B_{x0}H}{|B_{\text{sh}}(s)|} \text{arccosh}\left(\frac{|B_{\text{sh}}(s)|}{\sqrt{2\mu_0 p_w}}\right) \ ,$$

which is a good approximation for sufficiently small values of H . Using this definition we see that $w = 0$ for $B_{\text{sh}} = \alpha^{\frac{1}{2}} B_m$ and so the prominence exists in the region given by $\alpha^{\frac{1}{2}} B_m < B_{\text{sh}} < B_m$. Of course, this actually excludes the end-points of the current sheet from the prominence region, but it is a reasonable representation of the prominence boundary and allows some insight into this property.

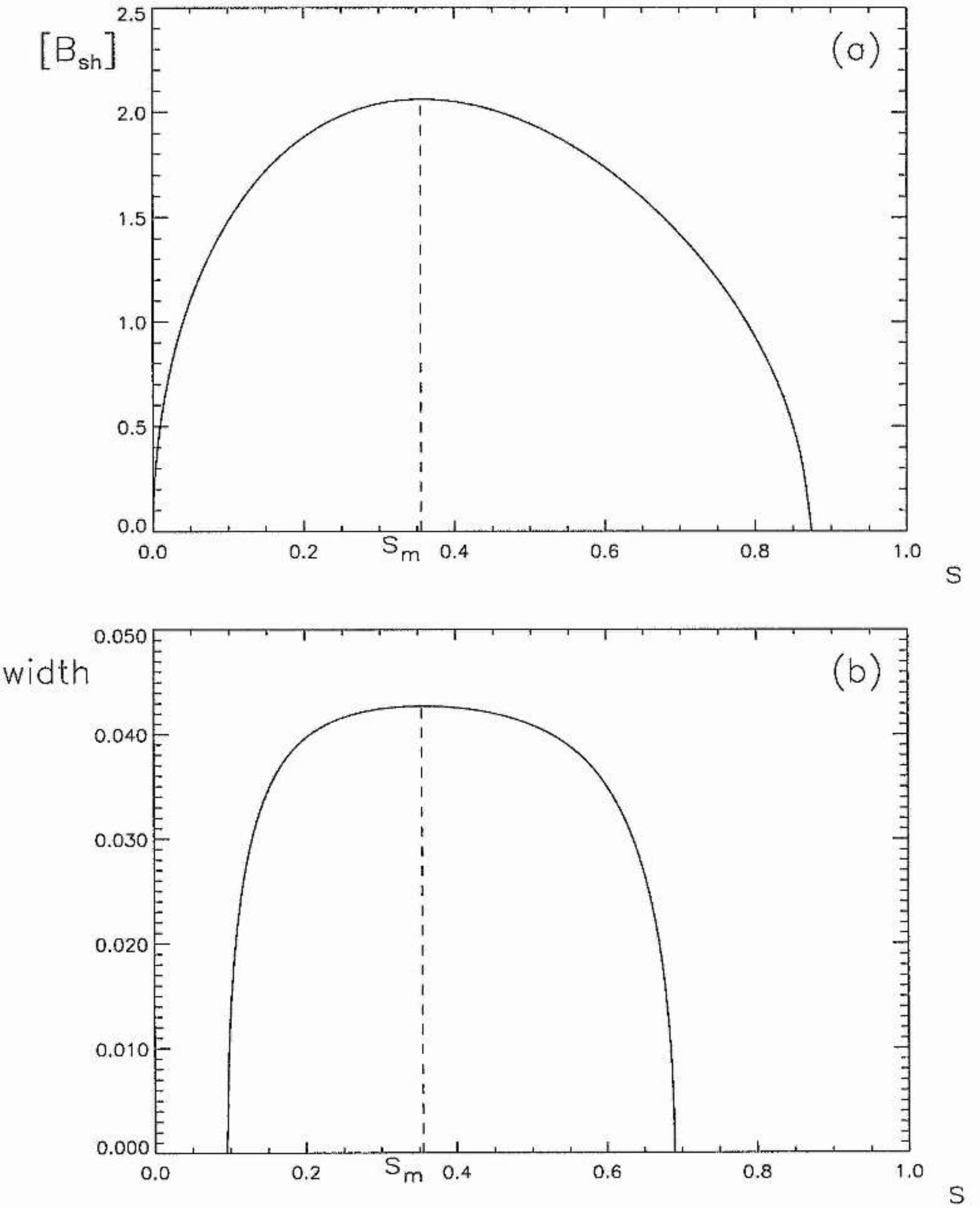

Figure 6.7: (a) The variation of the mass density along the sheet for the case $H = 0$. (b) The variation of the prominence width along the sheet.

6.5 Discussion

In this chapter, we have generalised the one-dimensional analysis of Kippenhahn and Schlüter to include prominence sheets which are inclined away from the vertical. The equilibrium of such a prominence is made possible by means of an enhanced magnetic field strength at the lower side of the sheet. This results in an asymmetric pressure balance across the sheet in which the surplus magnetic pressure force on the lower side is required to balance the component of weight in that direction. For the K-S case, no weight acts in that direction and so the magnetic pressure assumes a symmetric profile, its associated force required solely to confine the dense material by balancing the outwardly directed plasma pressure gradient.

In Section 6.4, a matching function technique has been applied enabling this type of internal solution to be incorporated in a more general model. We considered a specific example in which a curved prominence sheet of inverse magnetic polarity is embedded in a background configuration representing the polar-crown field, but this method may easily be applied to other similar models with non-vertical current sheets such as those of Wu and Low (1987).

The field around the current sheet can be separated into two fundamental components, namely the field due to a neutral current sheet and that of an ambient horizontal field. This allows a cut across the sheet to be considered by taking a curve which passes orthogonally to the field lines of the neutral sheet. Along this curve, the magnetic field given by the internal solution tends to a constant value as we move away from the centre of the sheet, this being the value of the magnetic field in the potential model just at the edge of the current sheet. In this way the two solutions are matched together providing us with a more detailed model in which both the global field structure and the interior of the prominence are given. It is possible to determine the width of the prominence in this model by defining the boundary of the prominence to lie along a contour of constant pressure, thus enabling the cross-section of the prominence to be examined. In our example this assumes the form of an elongated oval which is widest in the central section of the prominence. Such variations in prominence width and curvature are often found in observations.

Chapter 7

An Alternative Approach to Matching the Solutions

7.1 Chapter Summary

In the previous chapter we demonstrated how an internal magnetohydrostatic prominence solution can be asymptotically matched to an external potential solution for the case of a non-vertical, curved sheet of prominence material. This method, however, has the shortcoming that it generates only an approximate solution and so, in general, the magnetic field will only be divergence-free in an asymptotic sense (as the internal scale height tends to zero). That discrepancy is resolved in this chapter by using a slightly different approach which is applied to a basic example with a vertical current sheet. In the analysis the composite solution switches smoothly between the internal and external solutions through a region of overlap, or transition region, and it is possible to show that the field is divergence-free in each of these regions. The pressure, density and temperature are determined to check that the solutions are physically realistic.

7.2 Basic Example

Consider an inverse-polarity prominence solution obtained by the superposition of a potential field $B_Q(w)$, which has a vertically oriented neutral sheet, and a constant, horizontal background field, B_{x0} . A simple example is given by the field

$$B_P(w) = B_{Py} + i\ B_{Px} = B_Q(w) + i\ B_{x0}\ ,$$

in which

$$B_Q(w) = w^{\frac{1}{2}}(w-i)^{\frac{1}{2}} \quad \text{and} \quad w = x + i\ y\ . \tag{7.1}$$

The field lines for the neutral sheet component are shown in Figure 7.1a where we note that the sheet extends along the y-axis from the origin to $y = 1$. Figure 7.1b shows the resultant prominence field, $B_P(w)$, in which a weighted sheet, with surface mass density, $m_A(y)$, is supported by upwards tension forces that arise from the kinked field lines at the sheet. An X-type neutral point is located at

$$w_N = \left(0\ ,\ \frac{1}{2} - \frac{\sqrt{1+4B_{x0}^2}}{2}\right)\ .$$

We now set $B_{x0} = 1/2$ here (and for the remainder of this chapter) and so w_N is given by

$$w_N = \left(0\ ,\ \frac{1}{2} - \frac{1}{\sqrt{2}}\right)\ .$$

The surface mass and current densities at the sheet are given by the expressions

$$m_A(y) = \frac{[B_y](y)B_{x0}}{\mu_0 g} \quad ; \quad j_\Sigma(y) = \frac{[B_y](y)}{\mu_0}\ ,$$

where $[B_y](y) = 2y^{\frac{1}{2}}(1-y)^{\frac{1}{2}}$ is the jump in the vertical field component across the sheet.

From the analysis of the previous chapter, we can show that the matched field through the prominence region for a given internal scale height, ϵ, may be written as

$$B_P(w) = B_Q(w)\tanh\left(f(y)\frac{x}{\epsilon}\right) + \frac{1}{2}\ i\ , \tag{7.2}$$

where $f(y)$ is the value of the external potential field, $B_Q(w)$, at the edge of the sheet, i.e.

$$f(y) = B_Q(iy) = y^{\frac{1}{2}}(1-y)^{\frac{1}{2}} \quad , \quad 0 \le y \le 1\ .$$

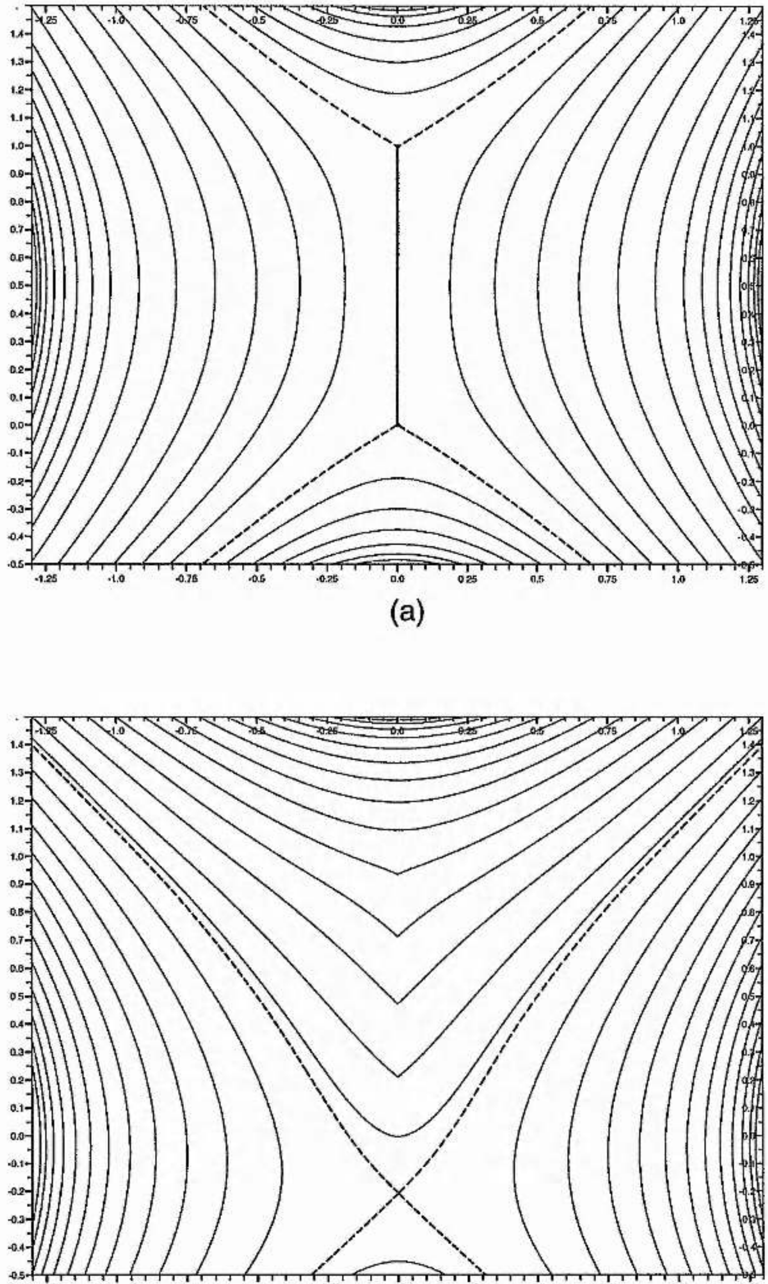

Figure 7.1: Field lines for (a) the neutral sheet and (b) the inverse-polarity prominence sheet.

Note that in this case, where a vertical sheet is used, our coordinate system has been altered slightly by setting $l_{\rm sh}(z) = x$ and $B_{\rm sh}(z) = f(y)$. This means that a slightly different cut across the current sheet has been taken; we do not need to consider a path across orthogonal neutral field lines here, although generally this is not possible for the case of a curved sheet.

The associated plasma pressure is given by

$$p(w) = \frac{f^2(y)}{2\mu_0}\mathrm{sech}^2\left(f(y)\frac{x}{\epsilon}\right) \ . \tag{7.3}$$

We now demonstrate how the matched magnetic field solution, $B_P(w)$, may be re-written so as to be explicitly expressed in terms of its constituent internal and external components. This allows us to examine the behaviour of the solutions through the two regions and shows how the composite solution switches between them across a region of overlap.

7.3 Internal and External Solutions

In this analysis we consider only the region $0 \leq y \leq 1$ corresponding to the vertical extent of the prominence sheet.

The external potential solution is given by the expression

$$B^{\rm ext}(w) = B_Q(w) + \frac{1}{2}\, i$$

with field components

$$B_x^{\rm ext} = \mathrm{Im}\left[B_Q(w)\right] + 1/2 \quad ; \quad B_y^{\rm ext} = \mathrm{Re}\left[B_Q(w)\right] \ . \tag{7.4}$$

Making an expansion of $B_Q(w)$ at a small distance $x = \delta$ from the sheet, we obtain the following:

$$\begin{aligned} B_Q(w) &= (\delta + i\,y)^{\frac{1}{2}}\,(\delta + i\,(y-1))^{\frac{1}{2}}\,, \qquad\qquad 0 \leq y \leq 1 \\ &= f(y)\left[\left(1 - \frac{i\,\delta}{y}\right)^{\frac{1}{2}}\left(1 + \frac{i\,\delta}{1-y}\right)^{\frac{1}{2}}\right] \end{aligned}$$

$$= \quad f(y)\left[1+\frac{i\,\delta\,(2y-1)}{2y(1-y)}+\mathrm{O}(\delta^2)\right] \qquad .$$

$$= \quad f(y) - i\,\delta f'(y) + \mathrm{O}(\delta^2)\ .$$

Therefore, the field components close to the edge of the sheet are approximately given by

$$B_y^o = f(y) \quad ; \qquad B_x^o = 1/2 - x f'(y)\ , \tag{7.5}$$

as long as the conditions

$$\delta \ll y \quad \text{and} \quad \delta \ll 1-y\ ,$$

are satisfied. This means that the solution is valid only in the region

$$x \ll y \ll 1-x\ .$$

Thus, an internal solution, written as

$$B_x^{\mathrm{int}} = \frac{1}{2} - x f'(y)\tanh\left(f(y)\frac{x}{\epsilon}\right) \quad ; \quad B_y^{\mathrm{int}} = f(y)\tanh\left(f(y)\frac{x}{\epsilon}\right)\ , \tag{7.6}$$

tends to the correct values, given by (7.5), as the inner variable, $X = x/\epsilon$, tends to infinity ($\epsilon \to 0$). Similarly, the external solution (7.4) tends to the same values as the outer variable, x, tends to zero.

Thus, our complete composite solution is given by

$$B_{Px} = B_x^{\mathrm{int}} + B_x^{\mathrm{ext}} - B_x^o \quad ; \quad B_{Py} = B_y^{\mathrm{int}} + B_y^{\mathrm{ext}} - B_y^o\ , \tag{7.7}$$

where B^o represents the overlap of the two solutions.

Figures 7.2 (a and b) show the internal, external and matched solutions for a value of $\epsilon = 0.1$ and $y = 0.7$. Here we see how the composite solution (solid curve) switches smoothly between the internal and external solutions. As ϵ is decreased, the composite solution converges to the external solution as the internal solution tends to, and hence cancels with, the overlap term. This effect can be seen in Figure 7.2 (c and d) in which a value of $\epsilon = 0.01$ is used.

Note that the composite solution is identical to the original matched solution (7.2) for this case, although this is actually a consequence of our chosen function $B_Q(w)$ and will

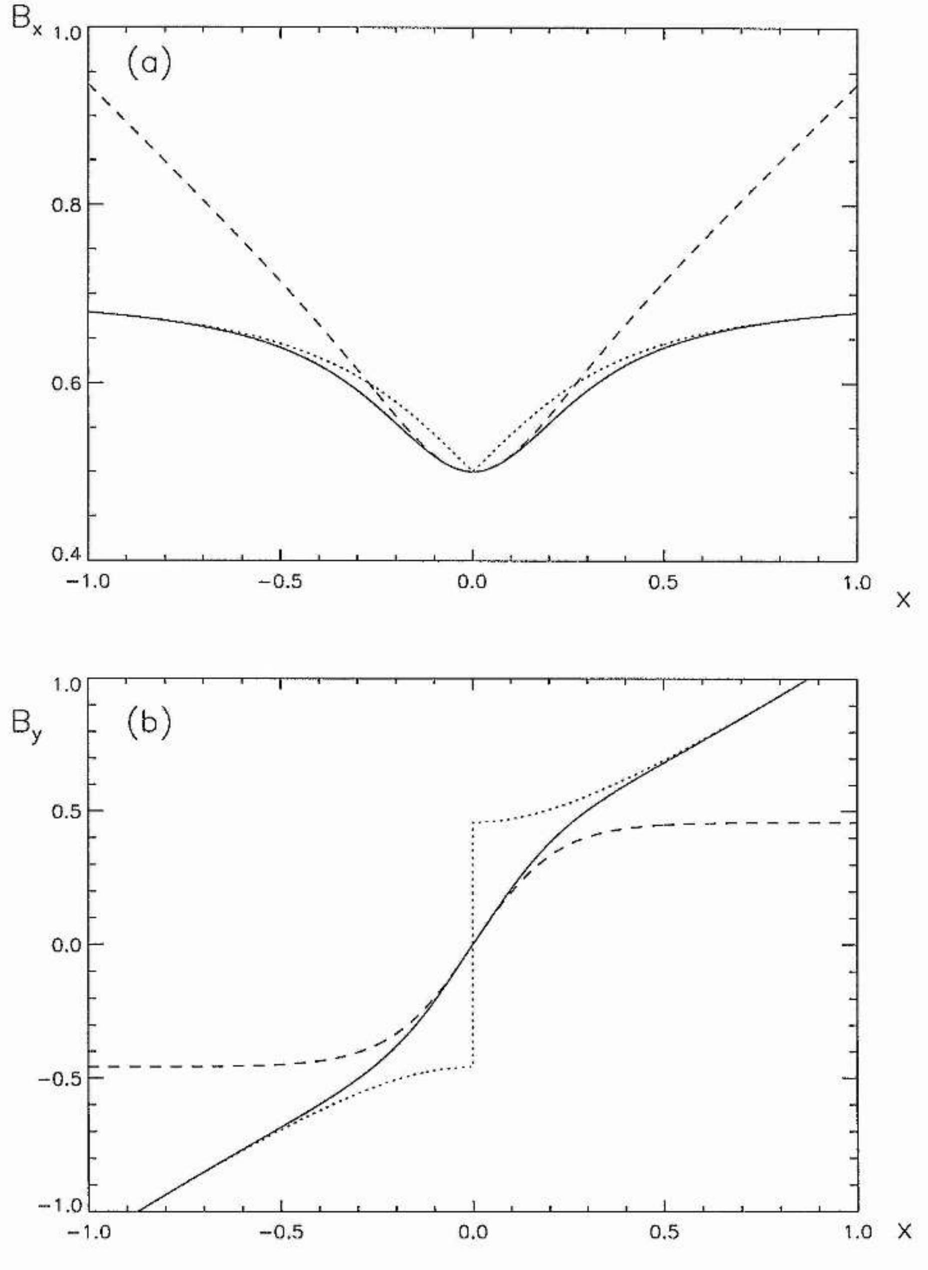

Figure 7.2: The field components of the internal (dashed line), external (dotted) and composite (solid) solutions for $\epsilon = 0.1$ (a,b) and $\epsilon = 0.01$ (c,d).

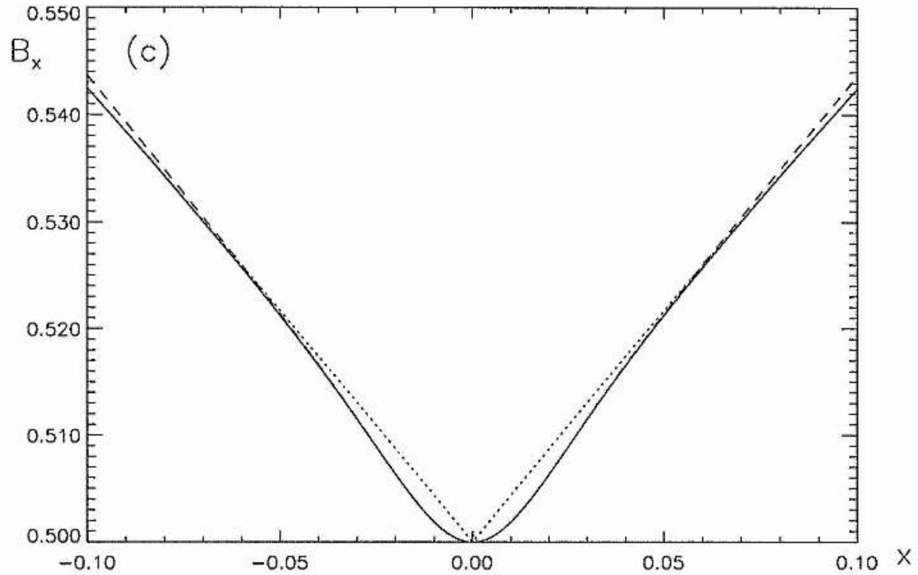

Figure 7.2c

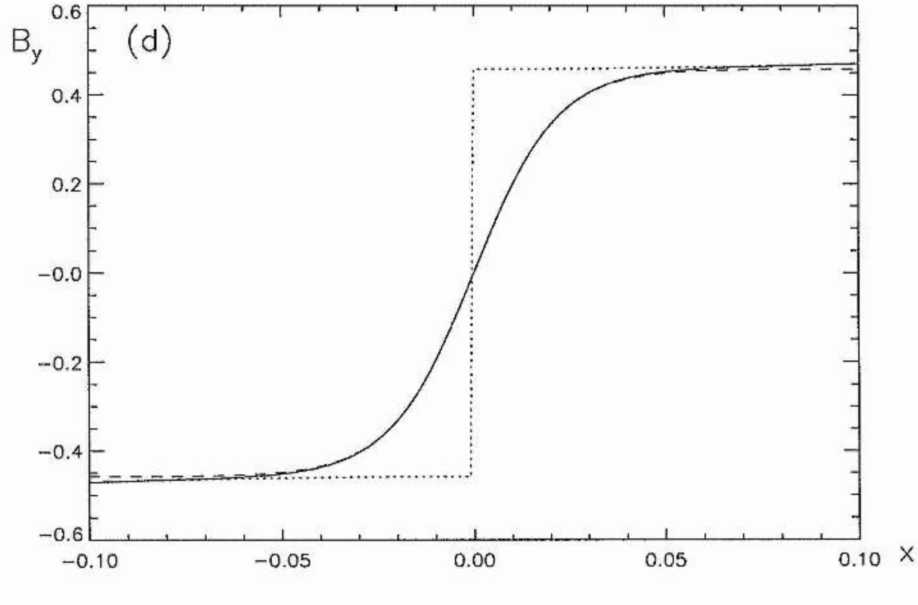

Figure 7.2d

not, in general, be true. Also, the solutions are sensitive to the nature of the cut across the sheet and so slight differences in the solutions may arise depending on how this cut is taken. Here, though, the cut is the same for both cases.

The matched field lines are shown in Figure 7.3 (dashed), where they have been superimposed onto the external, potential field lines (solid) for comparison. It can be seen that they smoothly match onto the external field, thus removing the discontinuities at $x = 0$ and resolving the prominence sheet into a distinct internal region of finite width. The field lines near the top and bottom of the sheet have not been plotted as this is the region in which the expansion breaks down. A modified analysis would be needed to cope with this region.

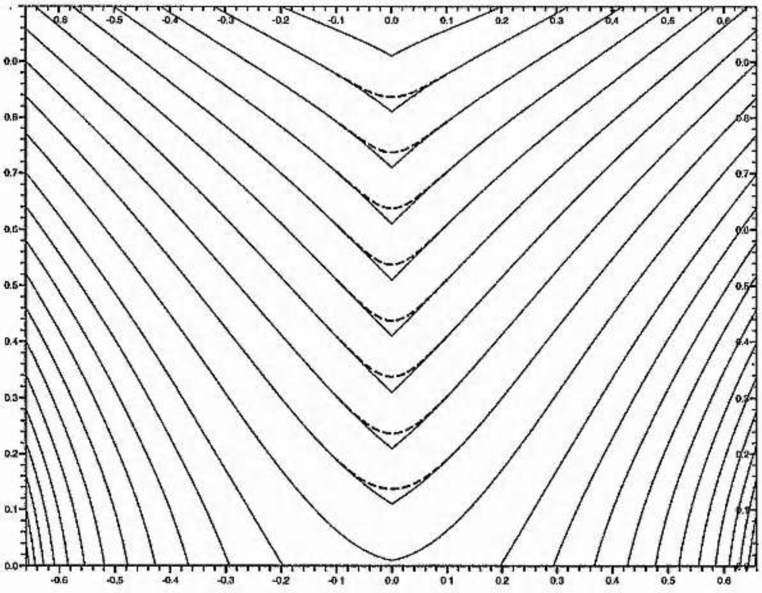

Figure 7.3: Plot of the external field lines showing also the matched solution (dashed lines) through the internal region.

Divergence of B

We now check that the composite solution (7.7) is divergence-free!

It is easy to show that $\nabla \cdot \mathbf{B}^{\mathrm{int}} = 0$. In fact we may find a vector potential, A^{int}, for the internal solution :

$$A^{\text{int}} = -\epsilon \ln\left(\cosh\left(f(y)\frac{x}{\epsilon}\right)\right) + y/2 \; . \tag{7.8}$$

This satisfies

$$\mathbf{B}^{\text{int}} = \frac{\partial A^{\text{int}}}{\partial y}\, \hat{\mathbf{x}} - \frac{\partial A^{\text{int}}}{\partial x}\, \hat{\mathbf{y}} \; ,$$

and so $\nabla \cdot \mathbf{B}^{\text{int}} = 0$ is automatically guaranteed.

The external solution, $B^{\text{ext}}(w) = B_y^{\text{ext}} + i\; B_x^{\text{ext}}$, is an analytic function of the complex variable w and so the Cauchy-Riemann equations are satisfied, ensuring

$$\frac{\partial B_y^{\text{ext}}}{\partial y} = -\frac{\partial B_x^{\text{ext}}}{\partial x} \; ,$$

and hence $\nabla \cdot \mathbf{B}^{\text{ext}} = 0$.

Finally, it is easily shown that $\nabla \cdot \mathbf{B}^o = 0$, with a corresponding vector potential, $A^o = -x f(y)$, thus completing the proof of

$$\nabla \cdot \mathbf{B}_P = 0 \; .$$

7.4 Other Properties

Once the full magnetic field solution, given by equations (7.4)-(7.7), has been obtained, it is important to investigate the other main properties, such as the current, pressure and density to check that they are physically realistic. Firstly, we need to evaluate the current density, j_z .

7.4.1 Current Density

The volume current density, j_z^{ext}, in the external region is zero, as this part of the solution is potential and hence current-free (by definition). It also follows that the overlap current, j_z^o, is zero and so the only contribution comes from the internal region. This is determined by the curl of the magnetic field, i.e.

$$\mu_0 \; j_z = \frac{\partial B_y^{int}}{\partial x} - \frac{\partial B_x^{\text{int}}}{\partial y} \; .$$

In terms of an inner variable, $X = x/\epsilon$, this can be written in powers of ϵ as

$$\mu_0 \; j_z = \left[\frac{f^2}{\epsilon} + \epsilon X^2 \left(f'^2 + \frac{1}{8f^2}\right) + \mathrm{O}(\epsilon^3)\right] \mathrm{sech}^2(fX) \; , \tag{7.9}$$

where f represents the function $f(y)$ and f', it's derivative.

Note that the leading term is of order $1/\epsilon$ and so the current profile spikes at $x = 0$ as $\epsilon \to 0$. The volumetric current density is infinite at this point, as B_y is discontinuous, but the surface current density is finite with a value of

$$\frac{2\,f}{\mu_0} = \frac{[B_y](y)}{\mu_0} \; ,$$

as stated earlier. This can easily be shown by integrating the leading order term of (7.9) across the sheet between the limits $x = -\infty$ and $x = +\infty$.

7.4.2 Pressure and Density

Once the current has been obtained, the plasma pressure can be evaluated from the horizontal force balance equation, i.e.

$$\frac{1}{\epsilon}\frac{\partial p}{\partial X} = -j_z \; B_y \; .$$

It is given by

$$p = \frac{f^2}{2\mu_0}\mathrm{sech}^2(fX) + \mathrm{O}(\epsilon^2) + F(y) \; , \tag{7.10}$$

where $F(y)$ is a constant of integration. This represents the background hydrostatic pressure, $F(y) = p_0 \; e^{-y/H_0}$, where p_0 is the pressure at the height of the lower end of the prominence ($y = 0$) and H_0 is the coronal scale height.

Force balance in the vertical direction allows us to solve for the density,

$$\frac{\partial p}{\partial y} = j_z \; B_x - \rho \; g \; ,$$

from which we find

$$\rho \; g = \frac{1}{\mu_0}\left[\frac{f^2}{2\;\epsilon} - f f' + \mathrm{O}(\epsilon)\right] \mathrm{sech}^2(fX) + \frac{p_0}{H_0}\; e^{-y/H_0} \; . \tag{7.11}$$

Note that the O(1) term from $j_z \; B_x$ has cancelled with the contribution

$$\frac{f^2}{2\mu_0}\frac{\partial}{\partial y}[\mathrm{sech}^2(fX)] \ ,$$

from the vertical pressure gradient.

Normalisation

We now fully non-dimensionalise these equations as follows.

In the function f, y has effectively already been normalised to the vertical extent, h_{pr} , of the prominence, i.e

$$y = h_{\mathrm{pr}}\ y^* \quad , \quad 0 \leq y^* \leq 1 \ ,$$

and so, if we write $f = B_{y0}\ f^* = B_{y0}\ {y^*}^{\frac{1}{2}}(1-y^*)^{\frac{1}{2}}$, with $B_{y0} = 1$, and set $p = p_0\ p^*$, we obtain for the pressure

$$p^* = \frac{{f^*}^2}{\beta_0}\mathrm{sech}^2(f^*X) + e^{-y^*h^*} + \mathrm{O}({\epsilon^*}^2) \ , \tag{7.12}$$

where $\beta_0 = (2\mu_0\ p_0)/B_{y0}^2$ is the coronal plasma beta, $\epsilon^* = \epsilon/H_0$ is the ratio of scale heights in the internal and external regions, and $h^* = h_{\mathrm{pr}}/H_0$ is the ratio of the vertical extent of the prominence to the coronal scale height.

For the density we set $\rho = \rho_0\ \rho^* = (p_0/gH_0)\ \rho^*$, and so we have

$$\rho^* = \left[\frac{{f^*}^2}{\beta_0\ \epsilon^*} - \frac{2f^*{f^*}'}{h^*\beta_0} + \mathrm{O}(\epsilon^*)\right]\mathrm{sech}^2(f^*X) + e^{-y^*h^*} \ . \tag{7.13}$$

7.4.3 Temperature

Finally, the temperature may be found from the ideal gas law, i.e.

$$T^* = \frac{p^*}{\rho^*} \ . \tag{7.14}$$

This should be checked, of course, to confirm that it gives a realistic value. We now use the following values to plot solutions for the pressure and density:

$$\beta_0 = 0.05 \quad ; \quad h^* = 0.25 \quad ; \quad \epsilon^* = 0.01 \ .$$

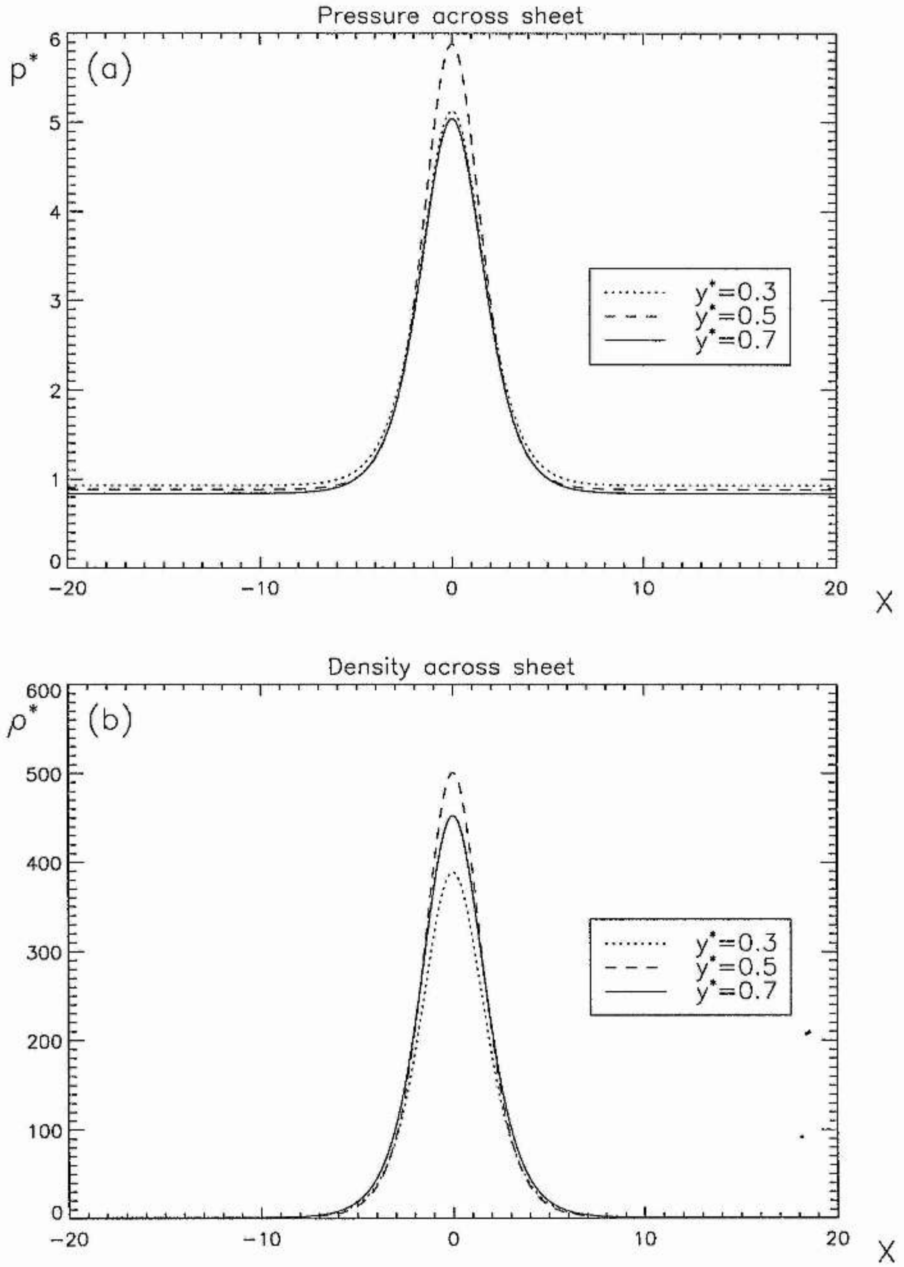

Figure 7.4: Profiles of pressure, density and temperature for various cuts across the sheet.

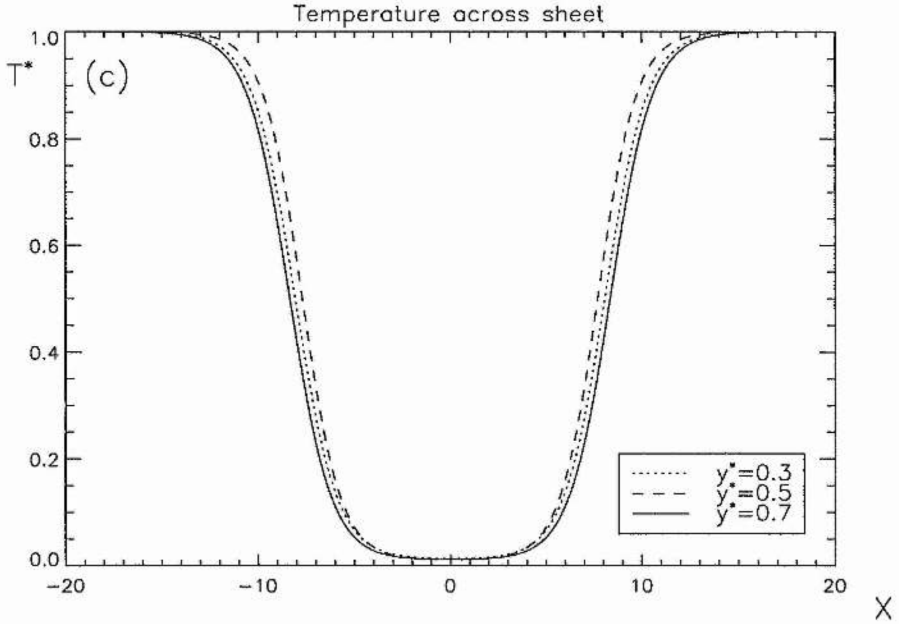

Figure 7.4c

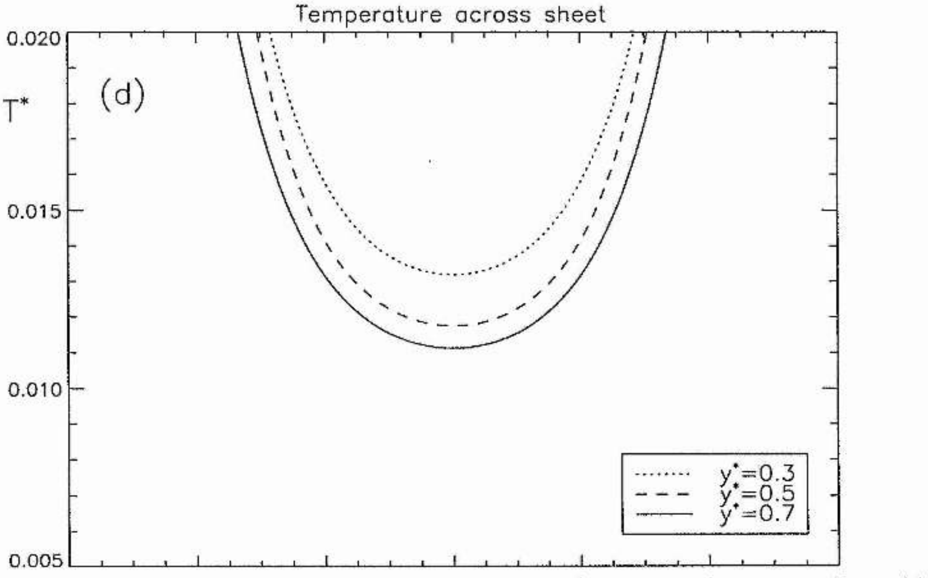

Figure 7.4d

Variations Across the Sheet

Profiles of the pressure, density and temperature for various cuts across the sheet are shown in Figure 7.4. In the external region (corona), $|X| \to \infty$, and so $p^* = \rho^* = e^{-y^* h^*}$ with $T^* = 1$. This is the background hydrostatic atmosphere, i.e.

$$p = p_0 e^{-y^* h^*} \quad ; \quad \rho = \rho_0 e^{-y^* h^*} \quad ; \quad T = T_0 \ .$$

As the centre of the sheet is approached, $X \to 0$ and so the pressure and density profiles gain maximum values of

$$p^* \sim \frac{{f^*}^2}{\beta_0} + e^{-y^* h^*} \quad \text{and} \quad \rho^* \sim \frac{{f^*}^2}{\beta_0 \ \epsilon^*} \ .$$

Also, the temperature reaches a minimum value of approximately $T^* \sim \epsilon^*$. For the above parameter values, this gives a central density 500 times higher than the corona and a temperature 100 times lower. Moving away from the sheet centre, the temperature remains close to this value for a few scale heights before rapidly rising to match onto the coronal value.

These solutions across the sheet are basically the original Kippenhahn-Schlüter solutions superimposed on a background hydrostatic atmosphere. However, variations along the sheet have also been considered in our analysis which we will now discuss.

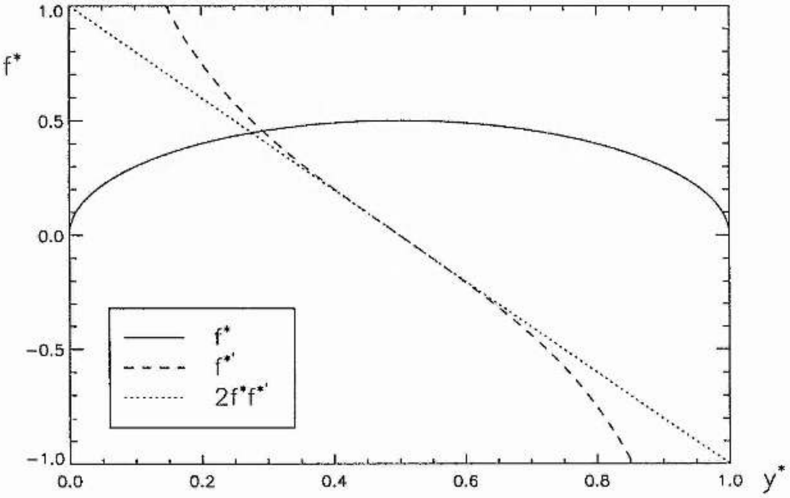

Figure 7.5: The variation of the function f^* and its derivatives.

Variations Along the Sheet

It is important to remember at this stage that the solutions cease to be valid close to the end-points of the sheet where the expansion of B_Q breaks down. Also, the nature of the function f^* implies that its derivative, $f^{*'}$, becomes infinite at these end-points. This can be rectified in the expression for the density, however, since it is the product, $2f^*f^{*'}$ that occurs in the order unity term, and this is equal to $(f^{*^2})' = 1 - 2y^*$ which tends to finite values (± 1) at the end-points. More will be said about this later. The behaviour of these functions is shown in Figure 7.5 for interest.

The pressure along the sheet basically depends on f^* and so has a symmetric profile with a small correction due to the hydrostatic term. This can be clearly seen in Figures 7.6a and 7.6b and also in Figure 7.4a, which shows that the maximum pressure at $y^* = 0.3$ is slightly higher than at $y^* = 0.7$ due to the influence of the background term, $e^{-y^*h^*}$.

The density, however, possesses an asymmetric distribution. The leading order term is the same as that in the pressure but with a factor of $1/\epsilon^*$ which causes an enhancement of two orders of magnitude! This is plotted as a dashed curve in Figure 7.6c. The O(1) term provides the asymmetry, as it gives rise to a negative correction for $y^* < 0.5$ and a positive correction for $y^* > 0.5$. The solid curve is the complete solution (to order unity), highlighting well the effect of this asymmetry. Note that an additional problem occurs near the end-points where the $O(1/\epsilon^*)$ term drops to zero yet the O(1) term remains finite. This results in the density tending to the values

$$e^{-y^*h^*} \mp \frac{1}{h^*\beta_0} ,$$

at the base and the top of the sheet, respectively. These large deviations from the hydrostatic values would cause a problem for the matching in the vertical direction, indeed, the density even becomes negative close to $y = 0$, but this is clearly an area that requires a separate and more elaborate treatment which we do not consider in this analysis. Figure 7.6d shows density contours for $0.1 \leq y^* \leq 0.9$, thus avoiding the problem region.

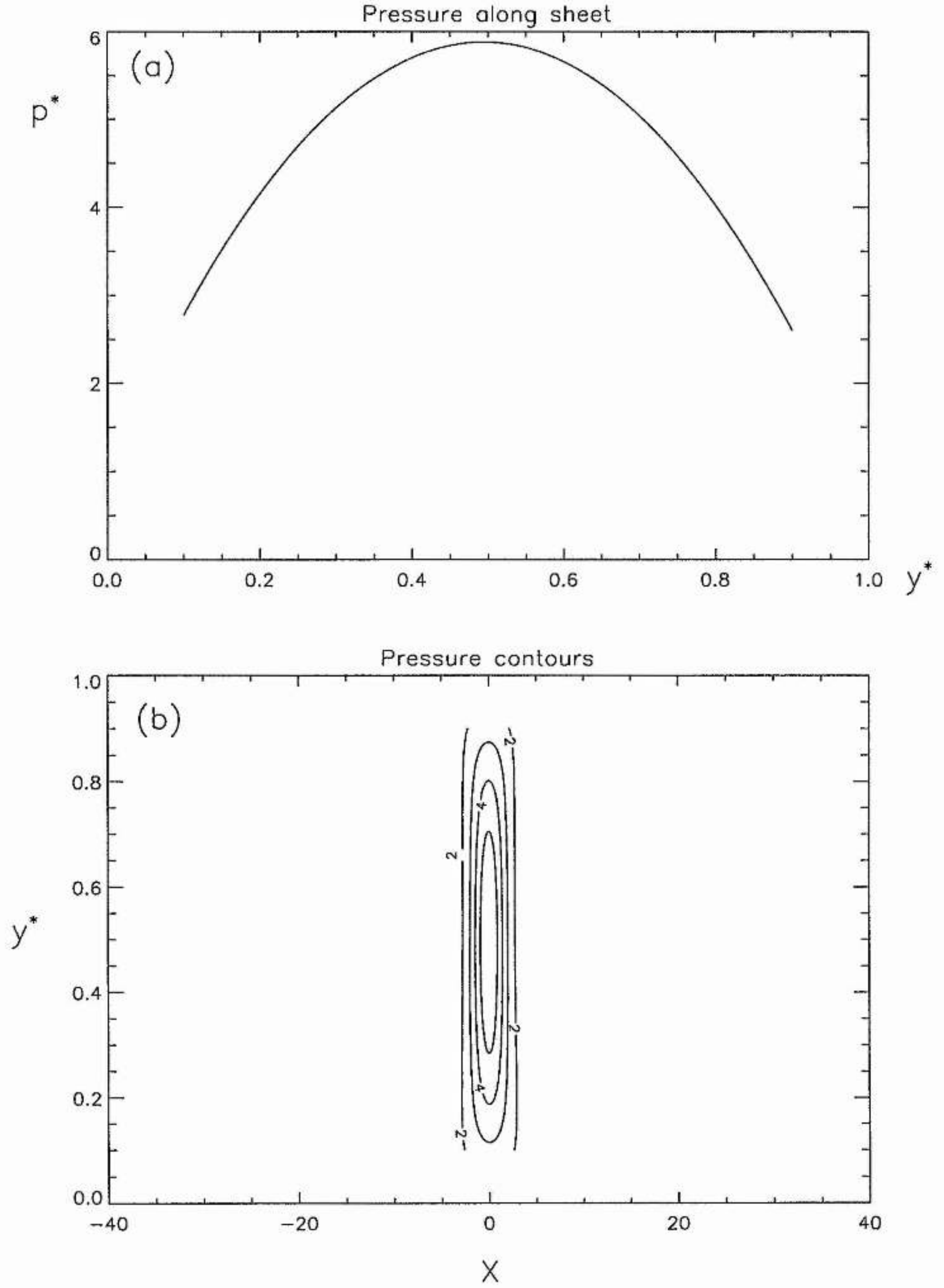

Figure 7.6: (a), (c) and (e) show profiles of the pressure, density and temperature along the sheet. Contours of these properties are shown in (b), (d) and (f). In each plot, the end-points of the sheet are excluded.

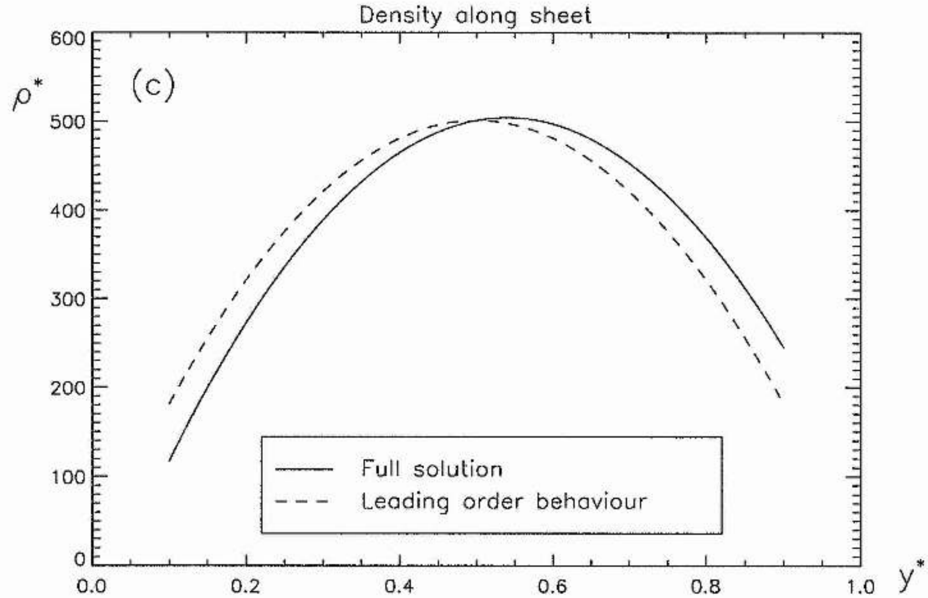

Figure 7.6c

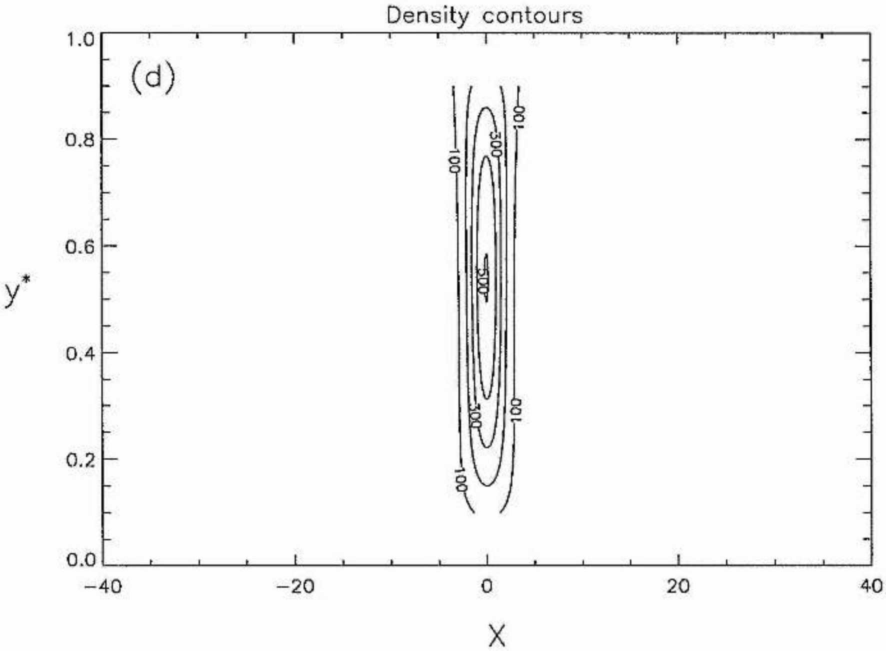

Figure 7.6d

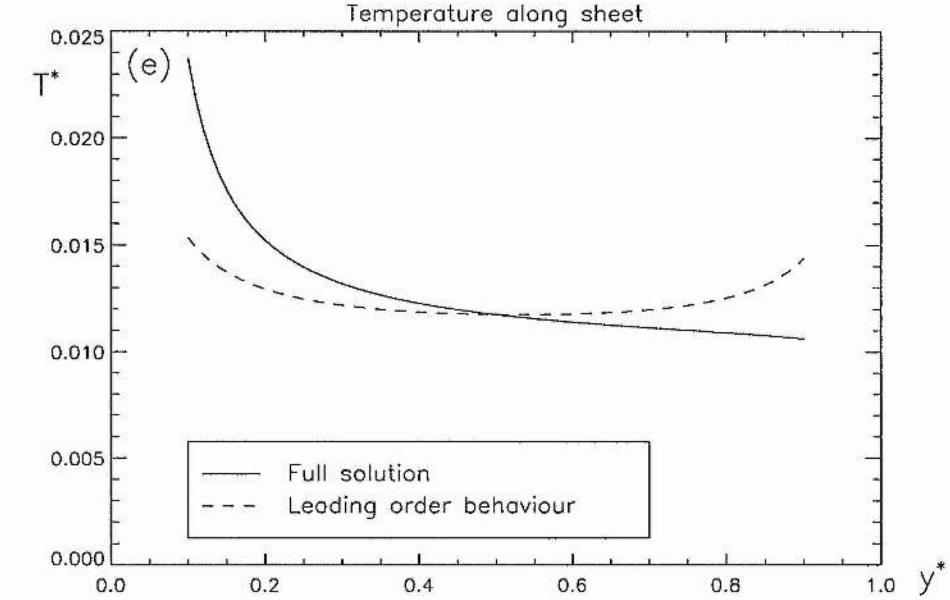

Figure 7.6e

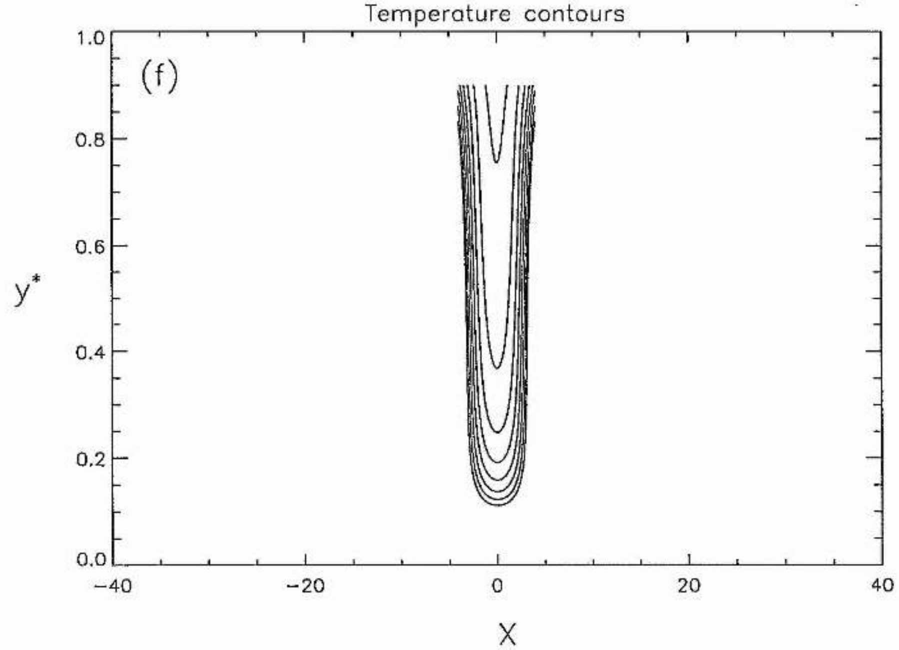

Figure 7.6f

Finally, the temperature distribution along the sheet is shown in Figures 7.6e and 7.6f. Again, the leading order behaviour is plotted as a dashed curve given by the expression

$$T^* \sim \epsilon^* \left(1 + \frac{\beta_0}{f^{*2}} e^{-y^* h^*}\right) ,$$

which is approximately constant along central section of the sheet. The solid curve and the contour plot show the full solution where, again, the poor behaviour at the end-points is noted.

7.5 Discussion

In this chapter we have made a slightly different approach to the matching of internal and external solutions through a prominence sheet by considering explicitly the two regions of concern. This has been done to enable a separate check of the constituent components of the solution to confirm that the solutions are well behaved and satisfy the original equations. In the example used, this approach yields a composite solution which is identical to the original solution (7.2) as long as a simple horizontal cut is taken and not a path orthogonal to the neutral sheet field. This is a consequence of the chosen functional form of the sheet, though, and in general the two solutions will differ slightly, with the original solution satisfying $\nabla \cdot \mathbf{B} = 0$ only in an asymptotic manner.

The other physical properties of this solution are quite interesting. To leading order, the basic Kippenhahn-Schlüter solution is found across the sheet in which the internal variables match smoothly onto the background hydrostatic corona. Along the sheet, however, variations are included in this analysis resulting in an asymmetric density profile and a temperature profile that increases gradually with height along the central section of the sheet. Problems are found, though, since the solutions cease to be valid as the ends of the sheet are approached. This is partly due to the expansion of B_Q breaking down and also because of the fact that the order unity term in the density does not drop to zero there. This causes the density to become too large at the top of the sheet and negative close to the bottom of the sheet which is unsatisfactory. A modified analysis would clearly be needed here to deal with this effect and ensure that the internal and external solutions could be matched in this direction.

Chapter 8

Conclusions

The work we have presented includes various analytical solutions for the equilibrium and structure of quiescent prominences supported in the Sun's magnetic field. The physical mechanisms by which these dense objects are supported against gravity are a key solar issue and must be studied in great depth if we are to develop our overall understanding of the Sun. In our work we have concentrated on magnetic configurations that are capable of providing such support, and by addressing relevant problems we have formulated and developed models to improve or further our ideas on these incredible features.

In Chapter 3 we extended the twisted flux-tube model, originally formulated by Ridgway, Priest and Amari (1991), to allow for the support of a *finite* height prominence sheet. This model is particularly encouraging as it provides good agreement with many of the associated observations. For example, twist is often in evidence in large quiescent prominences, especially whilst erupting; the inverse-polarity field commonly associated with quiescent prominences is a natural consequence of the geometry of the tube; the helical field lines provide a means of shielding the cool prominence material from the hot neighbouring environment and give a possible explanation for the surrounding coronal cavity; and since the solution permits a shearless outer edge, the tube can be matched onto a potential background configuration (Schönfelder and Hood, 1995), for example a large-scale helmet streamer, so that the tube forms the cavity within its base (see Low and Hundhausen (1995)). Also, the magnetic field in the sheet increases with height by a factor of approximately 50% which is in good agreement with the observations of Rust (1967) and Leroy et al. (1983).

By using an expanded scale and fitting a suitable magnetic field through the internal prominence region, we have demonstrated that cool, dense prominence solutions may be smoothly matched onto the external flux tube solution, thus resolving the current sheet and providing a more detailed description of the prominence interior. Realistic temperature and density profiles are achieved and they match onto the external values at both the edges and the ends of the prominence. In addition, Longbottom and Hood (1994) have examined the stability and find realistic stable and unstable loop lengths for observed prominence parameters when the axial magnetic field does not vanish.

In Chapters 4 and 5 we proposed a scenario for the formation of the large-scale polar-crown field and presented solutions for the subsequent equilibrium in which a prominence has formed. Given a typical distribution of photospheric magnetic field, we found that it is possible to obtain a pre-prominence configuration which includes a location of dipped magnetic field. This represents an advance over the preliminary calculations of Anzer (1994) as he was unable to find such dips.

The overall topology is *tripolar* (as the region of bipolar flux interacts with the large-scale source of unipolar field at the pole) which naturally gives rise to inverse-polarity solutions. For a more convincing geometry, the effect of curvature of the solar surface should be included, although this will not significantly alter the model's main qualitative features. Also, the field is restricted to two dimensions but this does, at least, give an indication of the basic configurations possible. We suggest that the effect of the solar wind should be incorporated, as this tends to stretch the field out at large distances and preserves the correct behaviour of the polar field.

The final solution consists of a *curved* prominence sheet supported in the location of dips; the equilibrium requires an enhanced magnetic pressure in the region below the prominence to support the component of weight in the normal direction. The stability of such a solution has yet to be examined, though it is highly likely that the material in the upper part of the sheet, which is largely slanted and not contained in significant dips, will be prone to sliding away, along the field lines to the surface. The field there is anchored in the dense photosphere but the field on the other side of the prominence is open and does not return to the surface. It may still be line-tied, however, the effect of the solar wind possibly providing additional stability.

The model presented here does not reflect the common idea of a prominence within a symmetric, large-scale helmet streamer and so new evidence is clearly required to check if this scenario is a real possibility. Examples of slanted prominences at the limb have been observed but they are not particularly common; it would be a valuable exercise, therefore, to make a detailed search of polar-crown prominence observations to see if they differ in this way from their lower-latitude counterparts.

In Chapter 4, we were able to construct curved prominence sheet solutions by adapting the general method of Titov (1992) and superimposing a suitable horizontal prominence field. In this way, a whole class of prominence solutions with asymmetric boundary conditions may be generated and so this technique clearly provides a very useful application of his method.

The potential model of Chapter 4 gives no information about the internal prominence structure and so we have studied methods, in Chapters 6 and 7, in which an internal magnetohydrostatic solution may be incorporated. Previous internal models have only considered vertical structures and so we have formulated a solution, based on the original model of Kippenhahn and Schlüter (1957), which gives the equilibrium of a sheet of *slanted* material. Once obtained, this solution represents a general cut across a *curved* prominence sheet and so, by allowing for the variations along the sheet, it is possible to match the internal and external solutions together. The drawback with this method is that it is only an approximate solution and so the field is not necessarily divergence-free. A way of avoiding this is to reformulate the matched solution by writing it in terms of its constituent components. In this way the composite solution is written as a linear combination of the internal solution, the external solution and a solution for the region of overlap. It can be shown that all of these components are divergence free thus resolving that particular discrepancy. Another problem arises, though, since the solution breaks down near the end-points of the sheet and so a separate treatment must be applied there. Hood (1995) has suggested a possibility by considering an expansion about the end-points, although this work is yet to be completed and so remains as a possible future extension.

We have demonstrated this alternative matching technique by considering a simple example with a vertical sheet, but it is clear that this may be applied to more general, curved situations. Once formulated, the solution may be used to find expressions for the current, pressure and density and these can be matched onto a background hydrostatic atmosphere as we demonstrated in Chapter 7. Another extension to this would be to drop the internal isothermal assumption and solve for the field with a given temperature variation.

It is worth stating that all of the models we have presented are either two-dimensional or invariant in the axial direction and so they represent a fairly crude, yet nonetheless invaluable, approximation. Little work has been done on modelling prominences in three dimensions, although Wu and Low (1987) and Démoulin, Priest and Anzer (1989) have made encouraging progress; this certainly presents a challenge for future work. In order to advance with the fundamental question of prominence support, it is often necessary to neglect many of the other inherent properties such as fine structure, feet and internal plasma flows. However, these are all important features and we must continue to study them separately with the ultimate aim of constructing a global, integrated model which will provide a better overall understanding. In addition, one also needs to consider the overall development, from the formation stage to the eventual eruption, to help provide explanations for other related events such as flares and CME's. Until such time, the study of quiescent prominences remains an enormous challenge to both the theorist and the observer and we may continue to wonder about the mysteries behind these intriguing entities.

Appendix A

Reduction of Equation 4.9 to the X-point Case and Recovery of the Purely Potential Solution

We investigate the behaviour of the general solution (4.9) as the current sheet solution is reduced to the case containing an X-type neutral point.

As $w_1, w_2 \rightarrow w_N$, $\mathbf{r_e} \rightarrow \mathbf{r_N} = (x_N, y_N, x_N, y_N)$ and so

$$Q(w) \rightarrow (w - w_N)(w - \bar{w}_N) = (w - x_N)^2 + y_N^2 \ .$$

The integral

$$\mathrm{I} \ = \int_{-\infty}^{+\infty} \frac{d\xi}{(\xi - w)Q(\xi)}$$

may be transformed into a contour integral as follows:

$$\lim_{R \rightarrow \infty} \int_{-R}^{+R} \frac{d\xi}{(\xi - w)Q(\xi)} = \lim_{R \rightarrow \infty} \left\{ \oint_C \frac{d\xi}{(\xi - w)Q(\xi)} - \int_\Gamma \frac{d\xi}{(\xi - w)Q(\xi)} \right\}$$

where $\Gamma = \{\xi \in \mathcal{C} \ : \mid \xi \mid = R, \ Im(\xi) \geq 0\}$

and $\quad C = \{\xi \in \mathcal{C} \ : \ (\xi \in \Gamma) \cup (-R \leq Re(\xi) \leq R)\}$.

Using complex variable theory the integral evaluated on the semicircle, Γ , vanishes as the radius, R, of the semicircle tends to infinity. Thus, the evaluation of I is reduced to finding the residues of the contour integral (contained in C), i.e. the residues in the upper-half plane.

There are two simple poles, at $\xi = w$, and $\xi = w_N$. Thus,

$$\int_{-\infty}^{+\infty} \frac{d\xi}{(\xi - w)Q(\xi)} = 2\pi i \sum_{\xi = w, w_N} \text{res} \left[\frac{1}{(\xi - w)Q(\xi)} \right]$$

$$= 2\pi i \left[\frac{1}{Q(w)} + \frac{1}{(w_N - w)(w_N - \bar{w}_N)} \right] ,$$

and so

$$\begin{aligned} B(w) &= -\frac{i}{\pi} Q(w) \left\{ \frac{2\pi i B_{y0}}{Q(w)} + \frac{2\pi i B_{y0}}{2i y_N (w_N - w)} - \frac{m\pi}{w^2 Q(0)} + \frac{m\pi Q'(0)}{w Q^2(0)} \right\} \\ &= B_{y0} \left(1 - i \frac{x_N}{y_N} \right) + \frac{i B_{y0}}{y_N} w + \frac{im}{Q(0)} \frac{Q(w)}{w^2} - \frac{im Q'(0)}{Q^2(0)} \frac{Q(w)}{w} . \end{aligned}$$

Collecting powers of w gives

$$B(w) = \left[\frac{i B_{y0}}{y_N} + \frac{2im x_N}{(x_N^2 + y_N^2)^2} \right] w + \left[B_{y0} \left(1 - i \frac{x_N}{y_N} \right) + \frac{im}{x_N^2 + y_N^2} - \frac{4im x_N^2}{(x_N^2 + y_N^2)^2} \right] + \frac{im}{w^2} .$$

To recover the purely potential solution, i.e.

$$B(w) = B_{y0} + i B_{x0} + \frac{im}{w^2}$$

we require that the O(w) term is zero and that the constant term reduce to $B_{y0} + i B_{x0}$. Hence,

$$\frac{B_{y0}}{y_N} + \frac{2m x_N}{(x_N^2 + y_N^2)^2} = 0 \Longleftrightarrow Re \left\{ B_{y0} + i B_{x0} + \frac{im}{w_N^2} \right\} = 0 . \qquad \text{(A1)}$$

Also,

$$-B_{y0} \frac{x_N}{y_N} + \frac{m}{x_N^2 + y_N^2} - \frac{4m x_N^2}{(x_N^2 + y_N^2)^2} = B_{x0} .$$

Using (A 1), this simplifies to

$$\frac{m}{x_N^2 + y_N^2} - \frac{2m x_N^2}{(x_N^2 + y_N^2)^2} = B_{x0}$$

and it follows from here that

$$Im \left\{ B_{y0} + i B_{x0} + \frac{im}{w_N^2} \right\} = 0 . \qquad \text{(A2)}$$

Hence, from equations (A 1) and (A 2) we deduce that the expression for the field reduces to the purely potential case iff w_N is a neutral point of this configuration.

Appendix B

Derivation of the Equations that Determine the End-points of the Current Sheet

As $w \to \infty$ we may make an expansion of $B(w, \mathbf{r}_\mathrm{e})$ as follows:

$$\begin{aligned} Q(w) &= [(w-w_1)(w-\bar{w}_1)(w-w_2)(w-\bar{w}_2)]^{\frac{1}{2}} \\ &= w^2\left[1-\frac{2x_1}{w}+\frac{x_1^2+y_1^2}{w^2}\right]^{\frac{1}{2}}\left[1-\frac{2x_2}{w}+\frac{x_2^2+y_2^2}{w^2}\right]^{\frac{1}{2}} \\ &= w^2\left[1-\frac{x_1+x_2}{w}+\mathrm{O}(w^{-2})\right] . \end{aligned}$$

Thus,

$$\begin{aligned} B(w) = i\frac{Q(w)}{\pi}&\left\{\int_{-\infty}^{+\infty}\frac{B_{y0}\left(1-\frac{\xi}{w}\right)^{-1}}{Q(\xi)w}d\xi+\frac{m\pi}{Q(0)w^2}-\frac{m\pi Q'(0)}{Q^2(0)w}\right\} \\ =\frac{i}{\pi}\left(w^2-(x_1+x_2)w+\mathrm{O}(1)\right)&\left\{\int_{-\infty}^{+\infty}\frac{B_{y0}}{Q(\xi)}\left(\frac{1}{w}+\frac{\xi}{w^2}+\frac{\xi^2}{w^3}+\mathrm{O}(w^{-4})\right)d\xi\right. \\ &\left.+\frac{m\pi}{Q(0)w^2}-\frac{m\pi Q'(0)}{Q^2(0)w}\right\} \end{aligned}$$

Now we must fix the asymptotic behaviour of this field (as $w \to \infty$) for the following two cases:

$$\text{(a) Neutral sheet :} \quad B(w) \to 0w + 0w^0 + \frac{1}{\pi w}\int_{-\infty}^{+\infty} B_{y0}\ d\xi \ ,$$

$$\text{(b) Prominence sheet :} \quad B(w) \to 0w + iB_{x0}w^0 + \frac{1}{\pi w}\int_{-\infty}^{+\infty} B_{y0}\ d\xi \ .$$

Thus, the first equation for the end-points, determined by the $\mathrm{O}(w)$ term, is the same for both cases, i.e.

$$\int_{-\infty}^{+\infty} \frac{B_{y0}}{Q(\xi)}\ d\xi - \frac{m\pi Q'(0)}{Q^2(0)} = 0 \ . \tag{B1}$$

The second equation is given by the behaviour of the constant term (w^0), i.e.

$$\int_{-\infty}^{+\infty} \frac{B_{y0}}{Q(\xi)}\left[\xi - (x_1 + x_2)\right] d\xi + \frac{m\pi}{Q(0)} + \frac{m\pi Q'(0)}{Q^2(0)}(x_1 + x_2) \ = \ \begin{cases} 0 \\ \pi B_{x0} \end{cases}$$

where the upper and lower conditions correspond to cases (a) and (b), respectively. Using (B 1) this reduces to

$$\int_{-\infty}^{+\infty} \frac{\xi B_{y0}}{Q(\xi)}\ d\xi + \frac{m\pi}{Q(0)} \ = \ \begin{cases} 0 \\ \pi B_{x0} \end{cases} \tag{B2}$$

Finally, the third equation is given by the behaviour of the (w^{-1}) term:

$$\int_{-\infty}^{+\infty} \frac{B_{y0}}{Q(\xi)}\left[\xi^2 - (x_1 + x_2)\xi + \mathrm{O}(1)\right] d\xi - \frac{m\pi}{Q(0)}(x_1 + x_2) - \frac{m\pi Q'(0)}{Q^2(0)}\mathrm{O}(1) = \int_{-\infty}^{+\infty} B_{y0}\ d\xi \ .$$

Using (B 1) the $\mathrm{O}(1)$ terms cancel and if (B 2) is applied there is much simplification so that the third expression is given by

$$\int_{-\infty}^{+\infty} B_{y0}\left(\frac{\xi^2}{Q(\xi)} - 1\right) d\xi \ = \begin{cases} 0 \\ \pi B_{x0}(x_1 + x_2) \end{cases} \tag{B3}$$

Appendix C

Treatment of the Integrals in Equations (B 2) and (B 3)

$$\text{As} \qquad \xi \to \infty, \qquad Q(\xi) \to \xi^2 \left(1 - \frac{x_1 + x_2}{\xi} + \mathrm{O}(\xi^{-2})\right)$$

and so the integral in (B 2), namely

$$\int_{-\infty}^{+\infty} \frac{\xi \, d\xi}{Q(\xi)} \qquad \text{behaves as} \qquad \int_{-\infty}^{+\infty} \frac{d\xi}{\xi} ,$$

which is clearly divergent. Thus one should consider this integral in the sense of the principle value. It may be transformed, however, to a normal integral if we note that

$$\mathcal{P} \int_{-\infty}^{+\infty} \frac{\xi}{\xi^2 + 1} \, d\xi \equiv 0 ,$$

so we can combine it with the integral of (B 2) without altering the total value. Hence,

$$\mathcal{P} \int_{-\infty}^{+\infty} \left(\frac{\xi}{Q(\xi)} - \frac{\xi}{\xi^2 + 1} \right) \, d\xi = \int_{-\infty}^{+\infty} \frac{\xi^3 + \xi - \xi Q(\xi)}{(\xi^2 + 1) Q(\xi)} \, d\xi .$$

Now there is cancellation of the cubic terms in the numerator and the integrand behaves as

$$\frac{\xi^2}{\xi^4} = \frac{1}{\xi^2} ,$$

as $\xi \to \infty$. The integrand remains finite, however, at $\xi = 0$ and so the integral is convergent with a finite sum.

Now, consider the integral in (B 3), i.e.

$$\int_{-\infty}^{+\infty} \frac{\xi^2 - Q(\xi)}{Q(\xi)} \, d\xi \, .$$

This too is divergent and so we must apply a similar treatment. For example,

$$\mathcal{P} \int_{-\infty}^{+\infty} \left(\frac{\xi^2 - Q(\xi)}{Q(\xi)} - (x_1 + x_2) \frac{\xi}{\xi^2 + 1} \right) \, d\xi = \int_{-\infty}^{+\infty} \frac{\xi^2 - Q(\xi)}{Q(\xi)} \, d\xi \, .$$

As $\xi \to \infty$, the integrand may be written:

$$\frac{(\xi^2 + 1) \left[\xi^2 - \xi^2 \left(1 - \frac{x_1 + x_2}{\xi} + \mathrm{O}(\xi^{-2}) \right) \right] - \xi (x_1 + x_2) \left[\xi^2 \left(1 - \frac{x_1 + x_2}{\xi} + \mathrm{O}(\xi^{-2}) \right) \right]}{(\xi^2 + 1) Q(\xi)} \, .$$

The denominator is of degree four but the numerator simplifies to

$$(\xi^2 + 1) \left[\xi (x_1 + x_2) + \mathrm{O}(1) \right] - (x_1 + x_2) \left[\xi^3 - \xi^2 (x_1 + x_2) + \mathrm{O}(\xi) \right] \, ,$$

and so the third-order terms cancel as well.

Thus, this integral now behaves as

$$\int_{-\infty}^{+\infty} \frac{\xi^2}{\xi^4} \, d\xi = \int_{-\infty}^{+\infty} \frac{d\xi}{\xi^2} \, ,$$

as required.

Appendix D

Neutral Point Equations

Consider the expressions given by equation (4.19), i.e.

$$B_{x0} = \frac{x_N^2 - y_N^2}{2x_N y_N} = \frac{x_N}{2y_N} - \frac{y_N}{2x_N} \ ,$$

and

$$1 = -\frac{(x_N^2 + y_N^2)^2}{2x_N y_N} = -(x_N^2 + y_N^2)\left(\frac{x_N}{2y_N} + \frac{y_N}{2x_N}\right) \ .$$

Now if we make the following change of variables:

$$x_N^2 + y_N^2 = r_N^2 \quad \text{and} \quad \frac{x_N}{y_N} = s < 0 \ , \tag{D1}$$

then the expression for B_{x0} is given by

$$B_{x0} = \frac{s}{2} - \frac{1}{2s} \ ,$$

and so

$$s = B_{x0} - \sqrt{B_{x0}^2 + 1} \ . \tag{D2}$$

Similarly, r_N^2 may be written

$$r_N^2 = \frac{2(\sqrt{B_{x0}^2 + 1} - B_{x0})}{1 + (\sqrt{B_{x0}^2 + 1} - B_{x0})^2} \ . \tag{D3}$$

Rewriting (D 1) and using (D 2) and (D 3) it follows that

$$x_N = -\frac{\sqrt{2(\sqrt{B_{x0}^2 + 1} - B_{x0})^3}}{1 + (\sqrt{B_{x0}^2 + 1} - B_{x0})^2} \quad , \quad y_N = \frac{\sqrt{2(\sqrt{B_{x0}^2 + 1} - B_{x0})}}{1 + (\sqrt{B_{x0}^2 + 1} - B_{x0})^2} \ . \tag{D 4}$$

Bibliography

Aly, J. J. and Amari, T. (1988). *Astron. Astrophys.* **207**: 154.

Aly, J. J. and Amari, T. (1989). *Astron. Astrophys.* **221**: 287.

Amari, T. (1988). PhD thesis, University of Paris VI.

Amari, T. and Aly, J. J. (1989). *Astron. Astrophys.* **208**: 261.

Amari, T. and Aly, J. J. (1990). *Astron. Astrophys.* **231**: 213.

Amari, T. and Aly, J. J. (1992). *Astron. Astrophys.* **265**: 791.

Antiochos, S. K. and Klimchuk, J. A. (1991). *Astrophys. J.* **378**: 372.

Anzer, U. (1972). *Solar Phys.* **24**: 324.

Anzer, U. (1984). *in* M. J. Hagyard (ed.), *Measurements of Solar Vector Magnetic Fields*, NASA CP-2374, p. 101.

Anzer, U. (1989). *in* E. R. Priest (ed.), *Dynamics and Structure of Quiescent Solar Prominences*, Kluwer Academic Publishers, Dordrecht, Holland.

Anzer, U. (1993). *Comments Astrophys.* **16**: 305.

Anzer, U. (1994). *in* V. Rusin, P. Heinzel and J.-C. Vial (eds), *Solar Coronal Structures, Proc. IAU Colloq. 144*, pp. 309–314.

Anzer, U. and Priest, E. R. (1985). *Solar Phys.* **95**: 263.

Athay, G., Querfeld, C. W., Smartt, R. N., LandiDegl'Innocenti, E. and Bommier, V. (1983). *Solar Phys.* **89**: 3.

Babcock, H. and Babcock, H. (1955). *Astrophys. J.* **121**: 349.

Ballester, J. L. and Priest, E. R. (1987). *Solar Phys.* **109**: 335.

Brown, A. (1958). *Astrophys. J.* **128**: 646.

Démoulin, P. and Priest, E. R. (1988). *Astron. Astrophys.* **206**: 336.

Démoulin, P. and Priest, E. R. (1993). *Solar Phys.* **144**: 283.

Démoulin, P., Malherbe, J. M. and Priest, E. R. (1989). *Astron. Astrophys.* **211**: 482.

Démoulin, P., Priest, E. R. and Anzer, U. (1989). *Astron. Astrophys.* **221**: 326.

Démoulin, P., Raadu, M. A., Malherbe, J. M. and Schmieder, B. (1987). *Astron. Astrophys.* **183**: 142.

Engvold, O. (1989). *in* E. R. Priest (ed.), *Dynamics and Structure of Quiescent Solar Prominences*, Kluwer Academic Publishers, Dordrecht, Holland.

Fiedler, R. A. S. and Hood, A. W. (1992). *Solar Phys.* **141**: 75.

Fiedler, R. A. S. and Hood, A. W. (1993). *Solar Phys.* **146**: 297.

Grad, H. and Rubin, H. (1958). *Proc. Second United Nations International Conf. in the Peaceful Uses of Atomic Energy, Geneva*, Vol. 31, pp. 190–7.

Hood, A. W. (1995). Private communication.

Hood, A. W. and Anzer, U. (1990). *Solar Phys.* **126**: 117.

Hood, A. W. and Priest, E. R. (1979a). *Astron. Astrophys.* **77**: 233.

Huggins, W. (1869). *Proc. Roy. Soc. (London)* **17**: 302.

Hundhausen, A. J., Sawyer, C. R., House, L., Illing, R. M. E. and Wagner, W. J. (1984). *J. Geophys. Res.* **89**: 2639.

Inhester, B., Birn, J. and Hesse, M. (1992). *Solar Phys.* **138**: 257.

Kim, I. S. (1990). *in* V. Ruzdjak and E. Tandberg-Hansen (eds), *Dynamics of Quiescent Prominences, Proc. IAU Conf.*, Vol. 117, p. 49.

Kippenhahn, R. and Schlüter, A. (1957). *Z. Astrophys.* **43**: 36.

Kuperus, M. and Raadu, M. (1974). *Astron. Astrophys* **31**: 189.

Kuperus, M. and Van Tend, W. (1981). *Solar Phys.* **71**: 125.

Leroy, J. L., Bommier, V. and Sahal-Bréchot, S. (1983). *Solar Phys.* **83**: 135.

Longbottom, A. W. and Hood, A. W. (1994). *Solar Phys.* **154**: 51.

Low, B. C. (1975). *Astrophys. J.* **198**: 211.

Low, B. C. (1991). *Astrophys. J.* **370**: 427.

Low, B. C. (1993). *Astrophys. J.* **409**: 798.

Low, B. C. and Hundhausen, J. R. (1995). *Astrophys. J.* **443**: 818.

Lust, R. and Schlüter, A. (1957). *Z. Naturforschung* **12a**: 850.

Malherbe, J. M. and Priest, E. R. (1983). *Astron. Astrophys.* **123**: 80.

Malherbe, J. M., Schmieder, B., Ribes, E. and Mein, P. (1983). *Astron. Astrophys.* **119**: 197.

Martin, S. F. (1986). *in* A. I. Poland (ed.), *Coronal and Prominence Plasmas*, NASA CP 2442, p. 73.

Martin, S. F. (1990). *in* V. Ruzdjak and E. Tandberg-Hanssen (eds), *Dynamics of Quiescent Prominences, Proc. IAU Conf.*, Vol. 117, p. 1.

McIntosh, P. S. (1980). *in* M. Dryer and E. Tandberg-Hanssen (eds), *Solar and Interplanetary Dynamics, IAU Symp.*, Vol. 91, p. 25.

Menzel, D. (1951). *Proc. Conf. on Dynamics of Ionised Media*, University College, London.

Milne, A., Priest, E. R. and Roberts, B. (1979). *Astrophys. J.* **232**: 304.

Mok, Y., Drake, J. F., Schnack, D. D. and VanHoven, G. (1990). *Astrophys. J.* **359**: 228.

Oran, E. S., Mariska, J. T. and Boris, J. P. (1982). *Astrophys. J.* **254**: 349.

Ploceniak, S. and Rompolt, B. (1973). *Solar Phys.* **29**: 399.

Pneuman, G. W. (1983). *Solar Phys.* **88**: 219.

Poland, A. I. (1986). *Coronal and Prominence Plasmas*, NASA CP 2442.

Poland, A. I. and Anzer, U. (1971). *Solar Phys.* **19**: 401.

Poland, A. I. and Mariska, J. T. (1986). *Solar Phys.* **104**: 303.

Priest, E. R. (1982). *Solar Magnetohydrodynamics*, D. Reidel, Dordrecht.

Priest, E. R. (1989). *Dynamics and Structure of Quiescent Solar Prominences*, Kluwer, Holland.

Priest, E. R. and Smith, E. A. (1979). *Solar Phys.* **64**: 267.

Priest, E. R. and VanBallegooijen, A. (1995). in press.

Priest, E. R., Hood, A. W. and Anzer, U. (1989). *Astrophys. J.* **344**: 1010.

Ridgway, C., Amari, T. and Priest, E. R. (1991). *Astrophys. J.* **378**: 773.

Ridgway, C., Amari, T. and Priest, E. R. (1992). *Astrophys. J.* **385**: 718.

Ridgway, C., Priest, E. R. and Amari, T. (1991). *Astrophys. J.* **367**: 321.

Rust, D. M. (1967). *Astrophys. J.* **150**: 313.

Ruzdjak, V. and Tandberg-Hanssen, E. (eds) (1989). *Dynamics of Quiescent Prominences*, Springer, New York.

Schmieder, B. (1989). *in* E. R. Priest (ed.), *Dynamics and Structure of Quiescent Solar Prominences*, Kluwer Academic Publishers, Dordrecht, Holland.

Schönfelder, A. and Hood, A. W. (1995). *Solar Phys.* **157**: 223.

Secchi, A. (1875). *Le Soleil*, Gauthier-Villars, Paris.

Shafranov, V. D. (1958). *Sov. Phys. JETP* **6**: 545.

Tandberg-Hanssen, E. (1974). *Solar Prominences*, D. Reidel, Dordrecht.

Tandberg-Hanssen, E. and Anzer, U. (1970). *Solar Phys.* **15**: 158.

Tang, F. (1987). *Solar Phys.* **107**: 233.

Titov, V. S. (1992). *Solar Phys.* **139**: 401.

Titov, V. S., Priest, E. R. and Démoulin, P. (1993). *Astron. Astrophys.* **276**: 564.

Ulloa, A. (1779). *Phil. Trans. Roy. Soc. (London)* **69**: 105.

Van Ballegooijen, A. A. and Martens, P. C. H. (1989). *Astrophys. J.* **343**: 971.

Van Hoven, G., Mok, Y. and Drake, J. F. (1992). *Solar Phys.* **140**: 269.

Van Tend, W. and Kuperus, M. (1978). *Solar Phys.* **59**: 115.

Vassenius, B. (1733). *Phil. Trans. Roy. Soc. (London)* **38**: 134.

Waldmeier, M. (1957). *Z. Astrophys.* **43**: 34.

Waldmeier, M. (1973). *Solar Phys.* **28**: 389.

Wu, F. and Low, B. C. (1987). *Astrophys J.* **312**: 431.

Zirin, H. (1988). *Astrophysics of the Sun*, Cambridge University Press.